

May 2015

Computational and Experimental Study on Innovative Horizontal-Axis Wind Turbine Blade Designs

Abdulrahman A. Alsultan
University of Wisconsin-Milwaukee

Follow this and additional works at: <https://dc.uwm.edu/etd>

 Part of the [Aerospace Engineering Commons](#), and the [Oil, Gas, and Energy Commons](#)

Recommended Citation

Alsultan, Abdulrahman A., "Computational and Experimental Study on Innovative Horizontal-Axis Wind Turbine Blade Designs" (2015). *Theses and Dissertations*. 791.
<https://dc.uwm.edu/etd/791>

This Thesis is brought to you for free and open access by UWM Digital Commons. It has been accepted for inclusion in Theses and Dissertations by an authorized administrator of UWM Digital Commons. For more information, please contact open-access@uwm.edu.

COMPUTATIONAL AND EXPERIMENTAL STUDY ON INNOVATIVE
HORIZONTAL-AXIS WIND TURBINE BLADE DESIGNS

by

Alsultan, Abdulrahman

A Thesis Submitted in

Partial Fulfillment of the

Requirements for the Degree of

Master of Science

in Engineering

at

The University Of Wisconsin-Milwaukee

May 2015

ABSTRACT

COMPUTATIONAL AND EXPERIMENTAL STUDY ON INNOVATIVE HORIZONTAL-AXIS WIND TURBINE BLADE DESIGNS

by

Alsultan, Abdulrahman

The University Of Wisconsin Milwaukee, 2015

Under the Supervision of Professor Ryoichi Amano

This study was made to explore three novel blade geometries with intent to increase power production of a horizontal axes, three blade arrangement wind turbine. This was done by designing the blades using computer aided design (CAD) modeling software, followed by a rigorous testing phase, utilizing a computational fluid dynamics software (CFD). The blades then went into a cycle of iterative design to achieve the best parameters that will positively impact the overall power generation efficiency. These steps were followed by printing the blades utilizing 3D Printing technology, testing them for the power generation, and finally, tabulating these findings to validate the numerical results gathered using CFD software. The blade designs under investigation here are the slotted blade (blade with slot shaped cavity on leading edge extending to lower surface), A blade resembling the tubercles (local inflations or bulges on surface) found on a humpback whale and the winglet blade, which was compared to the baseline traditional straight blade. The slotted, tubercle and straight blade were experimentally investigated, while the winglet blade underwent a CFD study only and compared to the other designs. It was found experimentally that the slotted blade generates 26.1% more power on average than the straight blade, and was found very ideal for low wind vacancies, while the tubercle was found of less effectiveness than the straight, though it possesses superior characteristics in suppressing the resultant noise, which is a common wind turbine problem. The winglet

showed very similar in results to the straight blade, where its addition would come very fruitful at higher wind velocities, due to the fact that the inertial forces needed to start the operation is a higher order of magnitude than the straight blade.

©Copyright by Abdulrahman Alsultan, 2015
All Rights Reserved

TABLE OF CONTENTS

ABSTRACT.....	ii
Table of Contents.....	v
List of figures.....	vii
List of Tables.....	ix
LIST OF NOMENCLATURE.....	x
ACKNOWLEDGMENTS.....	xi
Chapter I. Introduction.....	1
History of Wind turbines advancements.....	1
Chapter II. Wind Turbine Blade Design Considerations.....	7
Straight Blade Design (Control).....	8
Wind turbine Orientation.....	9
Mechanism of propulsion.....	9
Number of blades effect.....	10
Airfoil selection.....	10
Slotted Blade Design.....	12
Tubercle Blade Design.....	15
Upstream curved Winglet Blade Design.....	18
Chapter III. Experimental Facility.....	21
Wind tunnel Facility.....	21
Blades and Hub.....	22
FEA, 3D Printing and materials.....	22
Hot Wire, Data Acquisition Devices and Wind tunnel Flow field.....	27
Chapter IV. Experimental Procedures.....	31
Power Extraction.....	31
Experimental power calculation.....	35
Flow Mapping.....	36
Chapter V. Computational Fluid Dynamics (CFD).....	39
Computational Domain Construction.....	39
Mesh Generation.....	40
Turbulence model selection.....	42

Grid independence Test.....	43
Chapter VI. Results.....	45
Experimental results.....	45
Straight blade (Control).....	46
Slotted Blade.....	53
Tubercle Blade.....	59
CFD results.....	65
Straight blade.....	65
Slotted Blade.....	66
Tubercle Blade.....	68
Winglet Blade.....	70
Chapter VII. Discussion of Results.....	73
Experimental results.....	73
CFD Results.....	76
CFD Validation with Experiment and error discussion.....	77
Conclusions.....	79
References.....	80
Author's Research Publications on Thesis Topic.....	83
Appendix.....	84
A. Experimental findings.....	84
A.1-Straight blade findings.....	84
A.2-Slotted Blade findings.....	86
A.3-Tubercle Blade findings.....	88
B. CFD Findings (Pressure and Velocity).....	90
B.1-Velocity Vectors @ 5.3 m/s And 80 Rad/s.....	90
B.2-Velocity Vectors @ 6.2 m/s And 105 Rad/s.....	91
B.3-Velocity Vectors @ 7.7 m/s And 150 Rad/s.....	92
B.4- Pressure Contours @ 5.3 m/s And 80 Rad/s.....	93
B.5- Pressure Contours @ 6.2 m/s And 105 Rad/s.....	94
B.6- Pressure Contours @ 7.7 m/s And 150 Rad/s.....	95

LIST OF FIGURES

Figure 1: Ancient Egyptian sailboats.....	1
Figure 2: Mill Stone grinder for grains used by Persians (500-900 B.C.).....	1
Figure 3: Wind turbine developed in (1000 A.D.) and used to pump water.....	2
Figure 4: First Electrical Generating Wind turbine, made by James Blyth at Marykirk, Scotland July 1887.....	3
Figure 5: First automatically operated wind turbine, built by Charles F. Brush at Cleveland, Ohio late 1887.....	3
Figure 6: evolution in wind turbine technology (Source: NREL)	5
Figure 7: Lift and drag vectors on Aero foil.....	7
Figure 8: Straight Blade Design.....	8
Figure 9: airfoil variables and characteristics.	11
Figure 10: Circa 1938, NACA Langley wind tunnel testing for Leading edge slots.....	12
Figure 11: Slotted blade inlet and exit slots.....	13
Figure 12: Explanation of slotted blade Vs. Straight blade	14
Figure 13: Dimensions of slots as a percentage of chord	15
Figure 14: Humpback Whale flippers.....	15
Figure 15: tubercle blade design.....	16
Figure 16: visualizing the tubercle blade coordinates.....	17
Figure 17: implementation of tabulated coordinates on straight blade to make the tubercle blade.....	18
Figure 18: Reduction in the wingtip vortex size with the blended winglet.	19
Figure 19: Key design parameters of a winglet	19
Figure 20: Different views of the winglet blade	20
Figure 21: Wind tunnel facility and research lab at UW-Milwaukee.....	21
Figure 22: Different views of the Hub design	22
Figure 23: 3D Printed Blades using Renshape material.	26
Figure 24: Hot wire anemometer used for flow field mapping and three axes robotic traverse system.....	27
Figure 25: Sample calibration curve for the hot wire sensors U and V components.....	28
Figure 26: Robotic traverse system resolution demonstration.....	28
Figure 27: Wind tunnel boundary with the wind turbine installed.....	29
Figure 28: flow field mapping of velocity behind the wind turbine.	30
Figure 29: testing apparatus and wind turbine blades connected to the measurement column.....	31
Figure 30: National instrument NI 9215 Analog Data acquisition device.....	32
Figure 31: Monarch tachometer used to monitor the angular velocity at the hub.	32
Figure 32: National instrument NI 9402 Digital Data acquisition device	33
Figure 33: Labview program designed for voltage, RPM and time logging	33
Figure 35: Dedicated hot wire calibrator.	36

Figure 36: Hot wire and travers controlling program	37
Figure 37: hot wire acquisition system	38
Figure 38: computational domain	39
Figure 39: Straight blade computational domain mesh	41
Figure 40: Mesh deployed for all blade designs	42
Figure 41: Slotted blade grid independency test.....	43
Figure 42: Straight blade grid independency test	44
Figure 43: Power Extracted Vs. Resistive loading at 6.2 m/s.....	46
Figure 44: Power Extracted from Straight blade using different velocities.....	47
Figure 45: Straight blade Angular velocity Vs. U velocity	47
Figure 46: Straight Blade Torque Generation.....	48
Figure 47: Straight Blade Tip Speed Ratio.....	49
Figure 48: Slotted blade Power, Depicted as percentage of Straight Blade	53
Figure 49: Slotted blade Angular velocity Vs. U velocity.....	54
Figure 50: Slotted blade calculated torque.....	55
Figure 51: Slotted blade TSR values	55
Figure 53: Tubercle blade power as compared to the straight blade	59
Figure 54: Tubercle blade Angular velocity Vs. U velocity.....	60
Figure 55: Tubercle Blade Torque vs. U Velocity.....	61
Figure 56: Tubercle Tip Speed Ratio.....	61
Figure 58: Straight Blade CFD results for torque.....	65
Figure 59: Straight blade CFD Result For torque.....	66
Figure 60: Slotted Blade CFD Results for Torque.....	66
Figure 61: Slotted Blade CFD Results for Power Compared to straight blade	67
Figure 62: Slotted Blade Velocity Line integral Convolution.....	67
Figure 63: Tubercle Blade CFD results for torque	68
<i>Figure 64: Tubercle Blade CFD Results for Power Compared to straight blade.....</i>	<i>69</i>
Figure 65: Stream line plot colored by Turbulence Kinetic Energy for tubercle and straight blade.....	69
Figure 66: Winglet Blade CFD results for torque.....	70
Figure 67: Winglet Blade CFD Results for Power Compared to straight blade.....	70
Figure 68: Tip vortex for straight and winglet blade	71
Figure 69: Coefficient of performance Vs. TSR for slotted, tubercle and straight blade.	74
Figure 70: Typical Wind turbine Cp Values.....	74
Figure 71: CFD and experimental power findings for slotted and tubercle blade compared to the straight blade.....	77

LIST OF TABLES

Table 1: Wind Turbine Orientation Advantages.....	9
Table 2: Lift powered Vs. drag powered wind turbine.....	10
Table 3: Number of blades (N) impact on power production efficiency	10
Table 4: NACA 4412 characteristics	11
Table 5: Tubercle blade design parameters	17
Table 6: 3D printing candidate materials for FEA study	23
Table 7: FEA study showing Von mises stress and displacement result for straight, tubercle and slotted blade.....	24
Table 8: Mesh statistics for different blade designs.....	42
Table 9: Flow Field Mapping for Straight blade at different velocities, taken at inlet section of wind tunnel and 12in behind wind turbine.....	50
Table 10: Straight Blade Cp Values.....	51
Table 11: Straight blade Turbulence intensity	52
Table 12: Flow Field Mapping for Slotted blade at different velocities, taken at inlet section of wind tunnel and 12in behind wind turbine.....	56
Table 13: Slotted Blade Cp Values.....	57
Table 14: Slotted Blade Turbulence intensity.....	58
Table 15: Flow Field Mapping for Tubercle blade at different velocities, taken at inlet section of wind tunnel and 12in behind wind turbine.....	62
Table 16: Tubercle Blade Cp Values	63
Table 17: Tubercle Blade Turbulence intensity.....	64
Table 18: flow parameters used in CFD study.....	65
Table 19: summary of experimental findings for slotted, tubercle and straight blade.	73
Table 20: Torque CFD findings for the blades under investigation	76
Table 21: Power CFD findings for the blades under investigation.....	76
Table 22: Efficiency of experiment compared to the CFD findings.....	78
Table 23: Summary of experimental power collected from straight blade.....	84
Table 24: Summary of experimental Torque collected from straight blade	84
Table 25: Summary of experimental Angular velocity collected from straight blade.....	85
Table 26: Summary of experimental Tip speed ratio collected from straight blade.....	85
Table 27: Summary of experimental power collected from slotted blade	86
Table 28: Summary of experimental Angular velocity collected from slotted blade	86
Table 29: Summary of experimental torque collected from slotted blade.....	87
Table 30: Summary of experimental tip speed ratio collected from slotted blade	87
Table 31: Summary of experimental power collected from tubercle blade.....	88
Table 32: Summary of experimental torque collected from tubercle blade.....	88
Table 34: Summary of experimental angular velocity collected from tubercle blade	89
Table 35: Summary of experimental tip speed ratio collected from tubercle blade	89

LIST OF NOMENCLATURE

<i>A</i>	<i>Blade swept area (m²)</i>	Symbols	
<i>E</i>	<i>Energy (Joule)</i>	<i>C_p</i>	<i>Coefficient of performance</i>
<i>l</i>	<i>Chord length (m)</i>	<i>U(U_{cal})</i>	<i>relative standard uncertainty of the calibrator, %</i>
<i>L</i>	<i>Force due to lift (N)</i>	<i>U(U_{temp})</i>	<i>relative standard uncertainty factor due to temperature</i>
<i>m</i>	<i>Mass (Kg)</i>	<i>ρ</i>	<i>Density of air (in kg/m³)</i>
<i>ṁ</i>	<i>Mass flow rate (Kg/s)</i>	<i>τ</i>	<i>Torque (N.m)</i>
<i>N</i>	<i>Number of blades</i>	<i>TSR</i>	<i>Tip Speed Ratio</i>
<i>P</i>	<i>Calculated power, in Watts</i>	<i>TKE</i>	<i>Turbulence Kinetic Energy</i>
<i>T</i>	<i>Temperature, in Kelvin</i>	<i>RMS</i>	<i>Root Mean Square</i>
<i>R</i>	<i>Electric resistance, in Ohm</i>	<i>ω</i>	<i>Rotation speed of the fluid volume (in rad/s)</i>
<i>r</i>	<i>Rotor radius (m)</i>	<i>v</i>	<i>Velocity (m/s)</i>
<i>U</i>	<i>Wind tunnel velocity, in m/sec</i>	<i>ν</i>	<i>Kinematic viscosity of air (in m²/s)</i>
<i>V</i>	<i>Measured potential difference, in Volts</i>		
<i>Ṃ</i>	<i>Volumetric flow rate (M³/s)</i>		

ACKNOWLEDGMENTS

I would like to dedicate this work to my loving and caring mother, Nourah Almainan for all her support and positive enforcement and her encouragement throughout my life and studies. Moreover, I would like to acknowledge my program advisor, Dr. Ryoichi Amano for his guidance, leading the path for my research, aiding me in my engineering and publishing career. Additionally, I would like to thank all my family and friends, who helped me throughout my studies, their insights made me who I am today and they are my motivation to achieve more.

Chapter I. Introduction

This chapter is aimed to explore the historical advancements of wind turbines, economic importance and overview of the research study in hand

History of Wind turbines advancements

Energy is in the air, this statement is totally true, and was known since the beginning of ages. Going back to the ancient Egyptian empire, 5000 B.C., researchers of office of energy efficiency and renewable energy claim that wind was harvested and employed for propelling sail boats that can be seen in figure 1.



Figure 1: Ancient Egyptian sailboats

Those sailboats were used to move the huge rocks to build the pyramids along the shores of the Nile River. The US department of energy further elaborate that the development of wind harvesting devices did not stop there, where it was found that during the era of 500-900 B.C. Persians employed the wind energy into a more complex system, where they directed the wind to drive millstones to grind grains as seen in Figure 2.

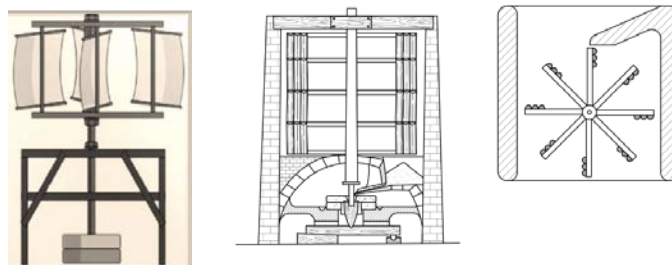


Figure 2: Mill Stone grinder for grains used by Persians (500-900 B.C.)

Lynn White Jr., a specialist in medieval European technology reports that during the 1000 A.D. at the start of the medieval era, new advancements were made in the functionality of wind turbines. European countries known now a days as Greece and Netherlands started using the wind energy as pumping devices, where it was used to drain lakes and small ponds off the Rhine river delta. This device is similar to the 20th century wind turbine, as seen in figure 3.



Figure 3: Wind turbine developed in (1000 A.D.) and used to pump water.

Since the development of water pumping wind turbines, the popularity of wind turbines increased. This was due to the increase in its functionality, where one could use a wind turbine for both grain grinding and pumping purposes. The progress was followed by centuries of enhancements and developments in shape, size and use. This development extended to the early 20th century, where the first electrical energy generation device was invented and erected during late 1800's -early 1900's. In July, 1887 A Scottish academic Professor, James Blyth was the first to generate power using a wind turbine. The purpose of his project was to light his home during the holiday season. What he did was, he erected a vertical axis wind turbine that can be seen in figure 4.

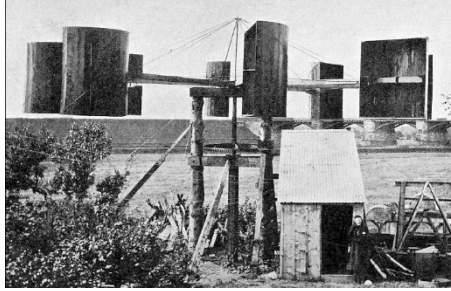


Figure 4: First Electrical Generating Wind turbine, made by James Blyth at Marykirk, Scotland July 1887.

James Blyth remarkable advancement in wind turbine technology was followed by the implementation of the first automated wind turbine. This automatically operated wind turbine, shown in figure 5, was built by Charles F. Brush, in Cleveland, Ohio, the same year James Blyth erected his, but some months later.

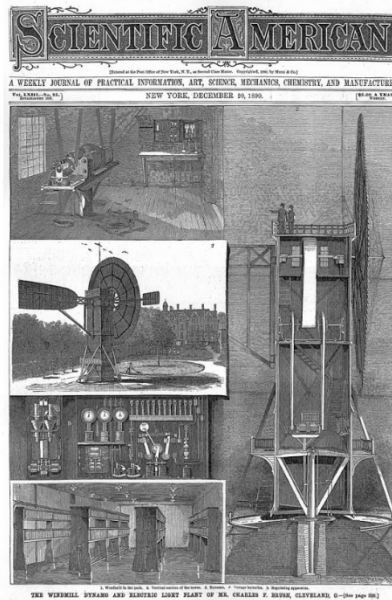


Figure 5: First automatically operated wind turbine, built by Charles F. Brush at Cleveland, Ohio late 1887.

This turbine was 18 m tall, weighed about 4 tons and generated about 12 kW of power, which was astonishing for such era. Following these advancements was a rapid increase in demand for wind turbines, especially in European countries such as Denmark, who, by the 1900, had about 2500 windmills that was used for milling and pumping reasons. Those wind turbines were repurposed to suite a new task which is electrical generation. At that

time, wind turbines offered a great deal of importance in rural communities, and areas of decentralized population topology. As well as a great potential to areas where the population is widely scattered. at that time, wind turbines offered a wiser economic solution than extending the power grid to farms and remote areas.

Since the time of egyptian sailboats, people tried to find a good reasoning of why the wind turbines managed to produce the force of lift, hence, producing power. A number of scientists tried to find what physical explanation to such a phenomena, which seemed to offer great potential. The journey to find reasoning behind wind energy brings us to the three people who uplifted the technology as we know it today, and widely known for being the three founders of wind energy.




Sir Isaac Newton

He presented his ideas about the three laws of motion the year 1686, And stated, **“Lift is the reaction force on a body caused by deflecting a flow of gas.”**



Daniel Bernoulli

He presented his work on conservation of energy to fluid dynamics the year 1738, and stated, **“Lift is generated by a pressure difference across the wing.”**



His Work Took Place Between 1922-1925 and he stated, **“By applying elementary physical laws, The Mechanical Energy extractable from an air stream passing through a given cross-sectional area is restricted to a certain fixed proportion of the energy or power contained in the air stream.”**

Albert Betz

Beginning in the 1980’s, the wind turbine industry showed an enormous growth in both size and power generation, as seen in figure 6.

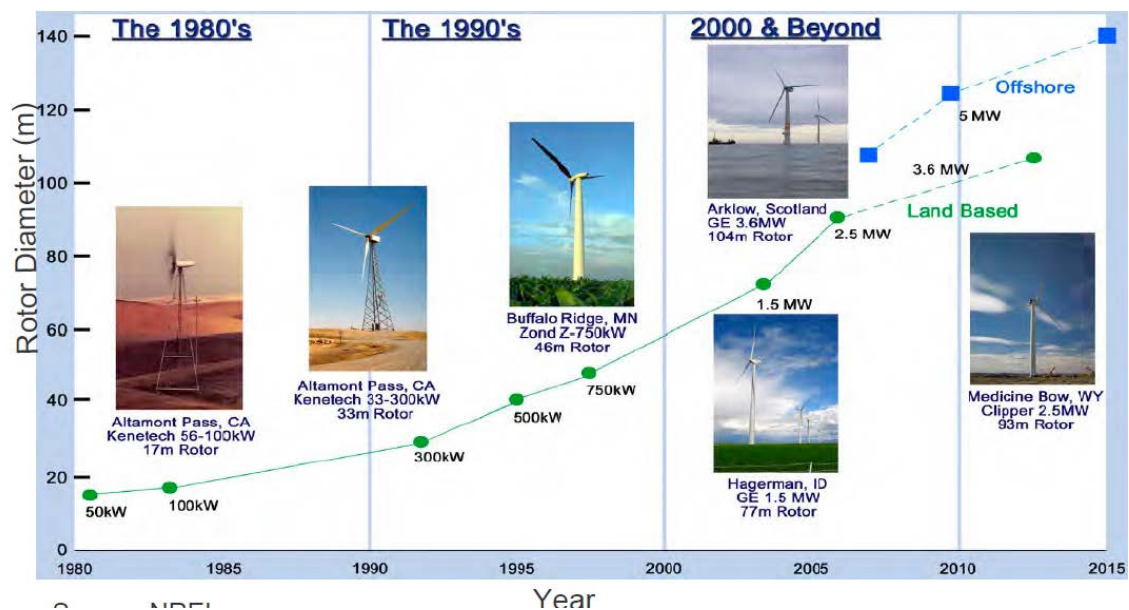


Figure 6: evolution in wind turbine technology (Source: NREL)

A lot of new techniques have been devised in order to increase the energy capacity, reliability as well as the efficiency of wind turbines. The implementation of active and passive controls as well as the implementation of new large rotors, allowed for an increase

in the energy generation, longer and lighter blades as well as to relieve the stress concentrations build on the tower. Here we work to further extend the reach of scientific advances in wind turbine, presenting new and innovative designs that are able to increase the efficiency of wind turbines.

Chapter II. Wind Turbine Blade Design Considerations

The wind turbine blade is analogous to the airplane wing, since they both work on the same principles, generating lift force due to the geometric shape. The airfoil shape dictates a highly curved leading edge, which separates the flow into two regions, (i.e. pressure side and suction side). The conservation of energy and momentum, then plays a big role, trying to equalize the pressure in the two abovementioned regions. The pressure side of the airfoil is governed by high pressure and low velocity, and the suction side is to possess low pressure with air particles moving at high velocity. The stream tries to bring the two sides to be equal in pressure, which would be translated to forces exerted on the area witnessing high-pressure, moving it towards the low-pressure region. This causes the well-known aerodynamic force; lift. While propagating through a medium, (i.e. liquid or gas), the same phenomena takes place, but this case, in an axial manner, requiring the airfoil to exert more energy to hold position. The force behind this hardship is referred to as the drag force. Figure 7 shows the vectors of the lift and drag as they act on an airfoil.

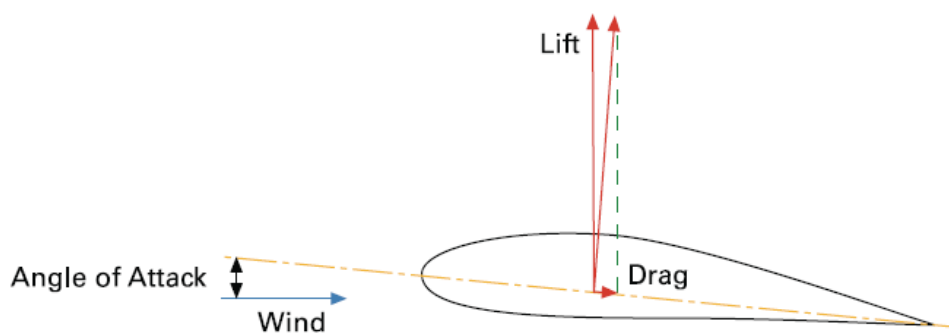


Figure 7: Lift and drag vectors on Aero foil

The design process for the three innovative wind turbine blades - slotted, winglet and tubercle - investigated in this research is discussed in this section. It is to be noted that the airfoil used in all these designs is the NACA4412 - which is known for its high lift to drag ratio approximately 100. Moreover, it is the most widely used airfoil profile for the wind turbine applications. The rotor diameter is kept the same at 0.3 m for all the different blade designs throughout the study.

Straight Blade Design (Control)

The straight blade resembles the conventional wind turbine blade used commercially and depicts a blade with a minimal twist, which is clear of alterations. This blade seen in figure 8, was used as a design baseline for all the three blades, which means, the straight blade was taken and modified to produce the slotted, winglet and tubercle blade.

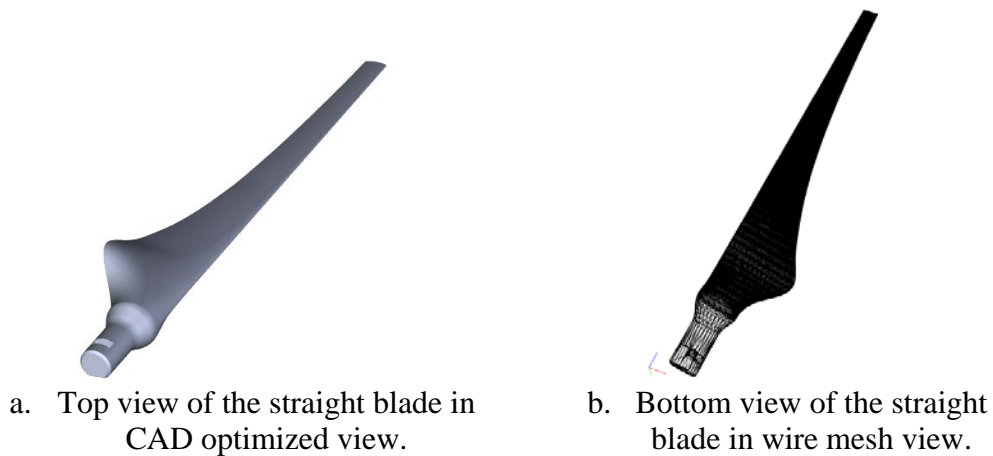


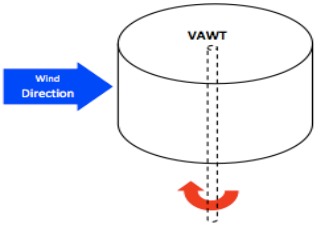
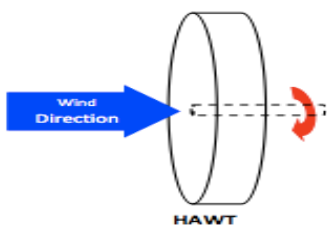
Figure 8: Straight Blade Design.

To make the straight blade, some design decisions had to be done, and presented here are the discussion of the benefits each design decision had to offer. These decisions were the motivation behind the straight blade design.

Wind turbine Orientation

The wind turbine orientation has important implications on the power production, the difficulty level of controlling the wind turbine, and to some extent, it dictates the tower shape and resultant loadings. Table. 1 highlights the advantages each design has to offer.

Table 1: Wind Turbine Orientation Advantages

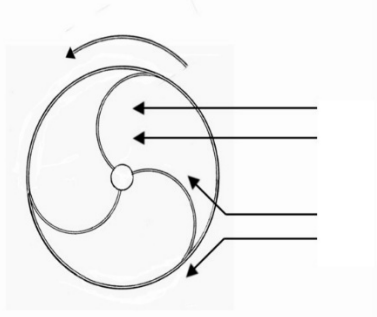
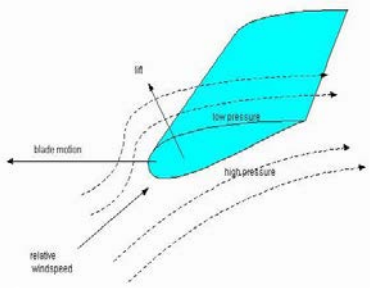
VAWT: Vertical Axes Wind Turbine	HAWT: Horizontal Axes Wind Turbine
<ul style="list-style-type: none"> • Low tip speed ratio. • Difficult to control rotor speed. • Incapable of self-starting. • Requires no additional mechanism to face the wind. • Heavy generators can be mounted. • Less tower loads. 	<ul style="list-style-type: none"> • More Rotor control through yaw and pitch. • Power generation by the Megawatt scale.
	

Mechanism of propulsion

There are two distinct Wind turbine mechanism of propulsion, as depicted in Table

2. The drag induced propulsion and lift-induced propulsion.

Table 2: Lift powered Vs. drag powered wind turbine

	Drag	Lift
Relative Wind Velocity	$= \text{WindVelocity} - \text{BladeVelocity}$	$= \sqrt{\frac{2}{3} \text{WindVelocity}^2 + \text{BladeVelocity}}$
Max. Theoretical Efficiency	16%	50%
Diagram		

The lift-induced propulsion offers a very high maximum cap of efficiency, compared to the drag type.

Number of blades effect

The number of blades (N), has influence on the power generation efficiency of the wind turbine and as seen in Table 3. The best arrangement that offers the highest efficiency is the three blade setting that was chosen for this investigation.

Table 3: Number of blades (N) impact on power production efficiency

Number Of Blades	Efficiency Impact
1	43%
2	47%
3	50%

Airfoil selection

The airfoil selection is one of the controlling factors that dictates the power production. Lift (L) is proportional to the torque generation, which directly translated to

power production. It is important to select the proper airfoil that will generate the highest lift while minimizing the drag, which negatively influences the efficiency.

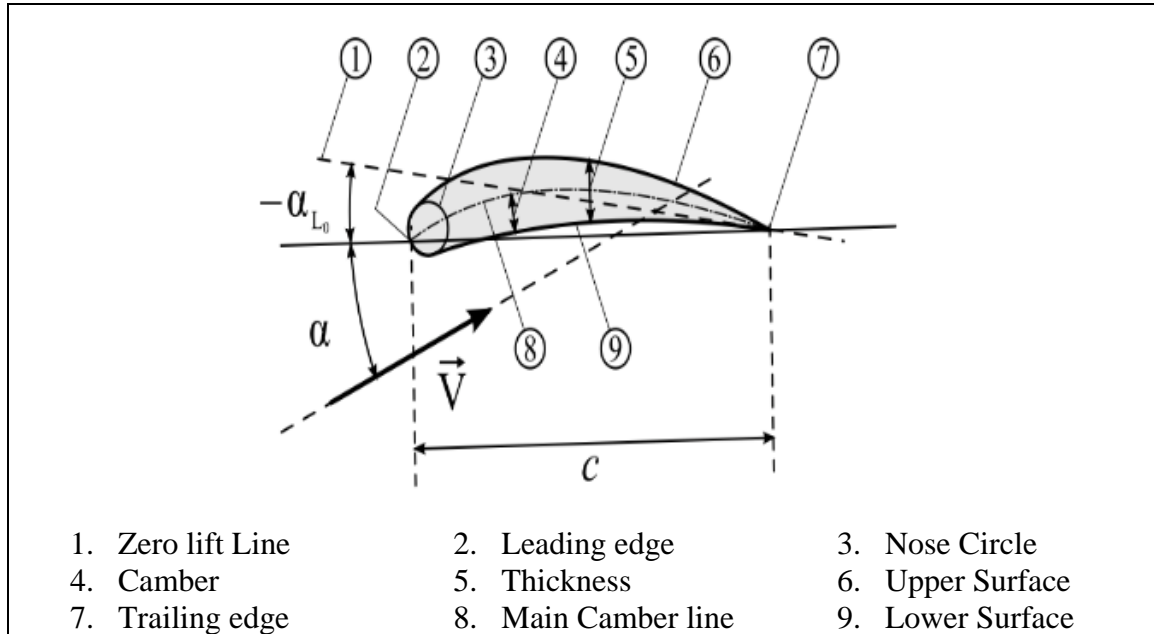


Figure 9: airfoil variables and characteristics.

Figure 9 illustrates the variables that control the airfoil, where manipulating these variables might result in different applications. The NACA 4412 is a well-established airfoil, and is great for research studies. It offers a great lift as compared to drag and great for the wind turbine studies. The NACA family has a wide range of airfoils for different purposes. The number 4412 corresponds to distinct characteristics of the foil, these characteristics are tabulated in Table 4.

Table 4: NACA 4412 characteristics

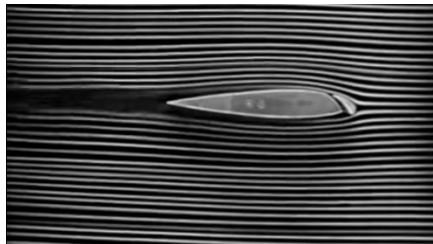
NACA-4412	
Max. Thickness location (t)	12% of the chord (Airfoil length)
Camber (m)	4% of the chord (Airfoil length)
Location of camber (p)	40% of the chord (Airfoil length)

After exploring the options of wind turbine design, we list the factors of our design to be based on the following parameters:

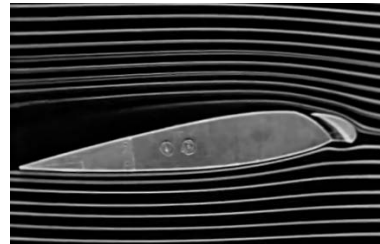
- Horizontal axes wind turbine
- Lift induced propulsion
- Three blade arrangement
- NACA 4412 airfoil

Slotted Blade Design

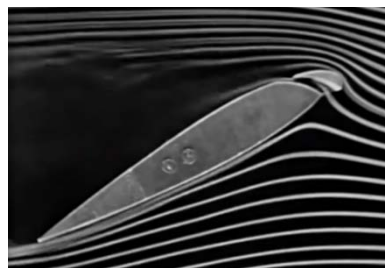
High lifting surfaces has been developed since the early 1900's, and still ongoing research for decreasing the energy consumption for civil, commercial as well as military aviation applications. One type of high-lift devices is the leading edge slot, or what is called, leading edge root extension (LERX). The leading edge slots are standard on modern fighter aircrafts, and seen on civil types as well.



a. Wing slots at $\alpha = 0^\circ$



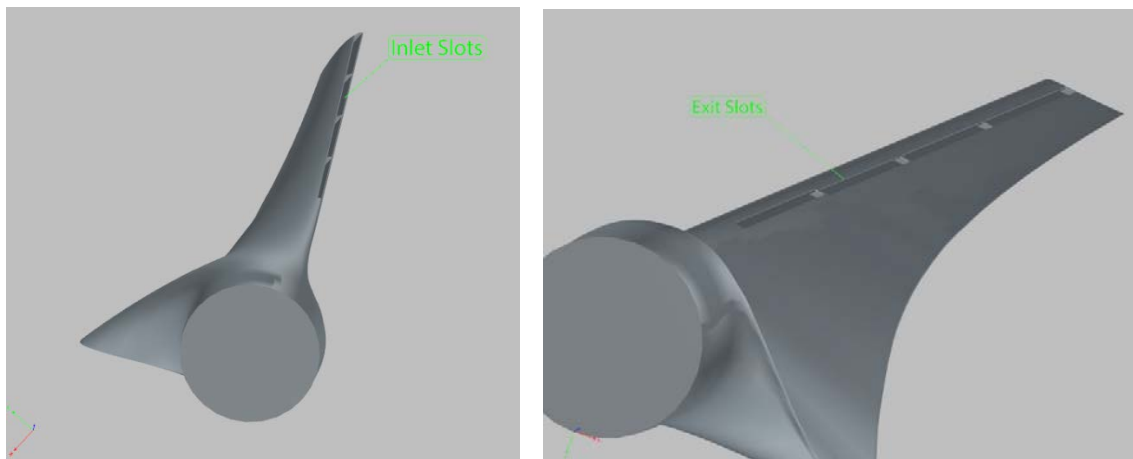
b. Wing slots increasing angle of attack



c. Wing slots at Stall conditions

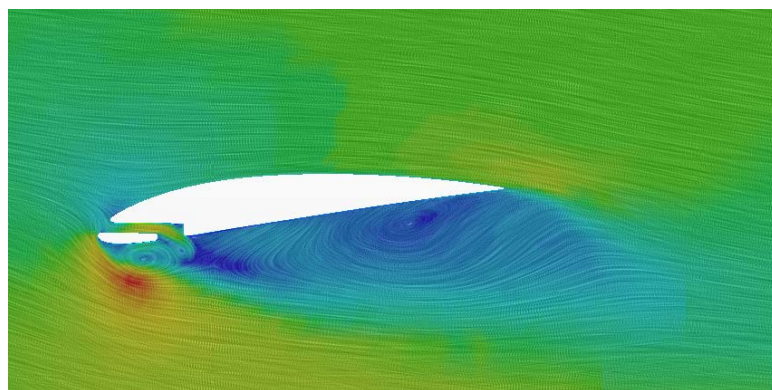
Figure 10: Circa 1938, NACA Langley wind tunnel testing for Leading edge slots

“The leading edge slots provides additional lift by delaying the upper body separation until higher angles than possible for plain wings, while the increasing the minimum drag” (Circa 1938, NACA Langley). The slots have been successfully tested and implemented on wings as seen in figure 10, which was a motivation to explore its addition into wind turbine blades. The addition of slots to wind turbine blade design came to tackle a problem else than the excessive angle of attack. Slots are deployed on the leading edge to introduce an internal flow within the blade. Figure 11 (a and b) shows the slots on the wind turbine blade.



a. Inlet Slots

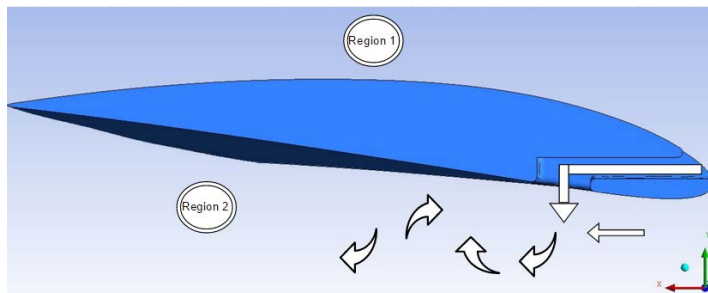
b. Exit slots



c. Side view of slotted blade showing the jets exiting slots and creating separation on lower surface.

Figure 11: Slotted blade inlet and exit slots.

Figure 11 c. gives a clear view how the flow behaves around the slotted blade. Furthermore, the slot channel depicted in figure 12 a will increase the velocity of air as it exits the slot from underneath the blade. This stream exiting the blade will adhere to the incoming stream. The resultant flow from the two streams then slows down further on region 2, Forcing the streams away from the body, creating a higher pressure on the bottom portion of the blade body permitting for separation to take place. Now, comparing the slotted blade with the straight blade. An apparent decrease in velocity can be seen in region 2 of the slotted blade when compared to the same region on the straight blade. This dictates that region to posses more pressure, translated directly to an increase in differential pressure, resulting in higher lift force as well as more torque generation.



a. Flow over slotted blade

	Region 1	Region 2
Velocity	High	Very Low
Pressure	Low	Very high



b. Flow over Straight blade

	Region 1	Region 2
Velocity	High	low
Pressure	Low	high

Figure 12: Explanation of slotted blade Vs. Straight blade

The slots were placed carefully on the stagnation point on the leading edge of the blade and the dimensions that were used to make the blade are referenced to the chord length, as a percentage. Figure 13 shows the dimensions used for the slots.

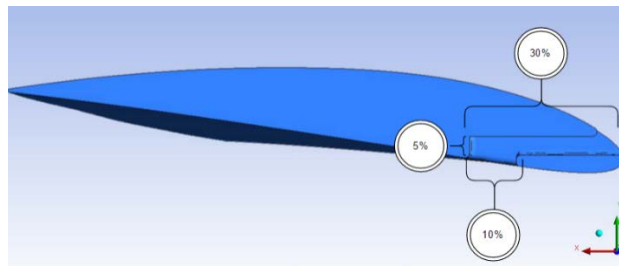


Figure 13: Dimensions of slots as a percentage of chord

Tubercle Blade Design

Since the beginning of ages, humans observed their surroundings in order to learn and enhance their lifestyles and nowadays, we can observe an emergence in biomimetic technology, ranging from Nanoscale to larger scales. This fact brings us to one of the nature wonders, the humpback whale.



Figure 14: Humpback Whale flippers

The marine biologist researchers observed the humpback whale in its habitat and concluded its superior control over turns utilizing the tubercles located on the flippers. Since whales have a relatively stiff body they cannot bend into a turn like many other sea creatures. Instead, whales rely on the lift forces generated by the tubercle flippers to manipulate its direction. A whale utilizes tubercles at the trailing edge of the flipper as depicted in figure

14. The additional lift force is generated by the troughs resembling tubercles on the flippers. As the fluid moves along the body of the flipper, the fluid is accelerated into an organized rotating flow behind the tubercles. The acceleration of the fluid flow increases the velocity of the flow which increases the angle of attack at which stall occurs (Kumar, S., & Amano, R. S.). The additional lift produced by tubercles was a motivation to explore further the advantages of trailing edge tubercle wind turbine blade.

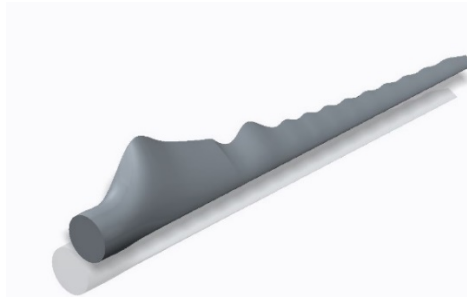


Figure 15: tubercle blade design

The trailing edge tubercle blade design, seen in figure 15, was created based on the straight blade root, manipulating the chord lengths throughout the blade span. None the less, the tubercle has a consistent decrease in chord, from root to tip, decreasing incrementally in three distinct steps, 100%, 90% and 80%. The incremental design process can be seen in figures 16 and 17, where 100% corresponds to the chord length of the straight blade (Control), located at the same distance from the root. Followed by a chord section, equivalent to 90% of the original chord, marked as 100%. Follows that a section, possessing a chord length equal to 80% of the original. Finally, the last chord decreases to merge with the length of the straight blade by taking that chord to be equivalent to 90% of the 90% section. Table 5 shows the dimensions used to make the tubercle blade.

Table 5: Tubercle blade design parameters

Span wise length	Datum#	Chord	Tubercle Chord 80%	Tubercle Chord 90%
93.75	DTM1	32.67		
104.06	DTM12			29.41
114.38	DTM2		26.14	
124.69	DTM13			28.75
135.00	DTM3	25.43		
145.31	DTM14			22.88
155.63	DTM4		20.34	
165.94	DTM15			22.37
176.25	DTM5	20.52		
186.56	DTM16			18.47
196.88	DTM6		16.42	
207.19	DTM17			18.06
217.50	DTM7	17.10		
227.81	DTM18			15.39
238.13	DTM8		13.68	
248.44	DTM19			15.05
258.75	DTM9	14.73		
269.06	DTM20			13.26
279.38	DTM10		11.78	
289.69	DTM21			12.96
300.00	DTM11	13.73		

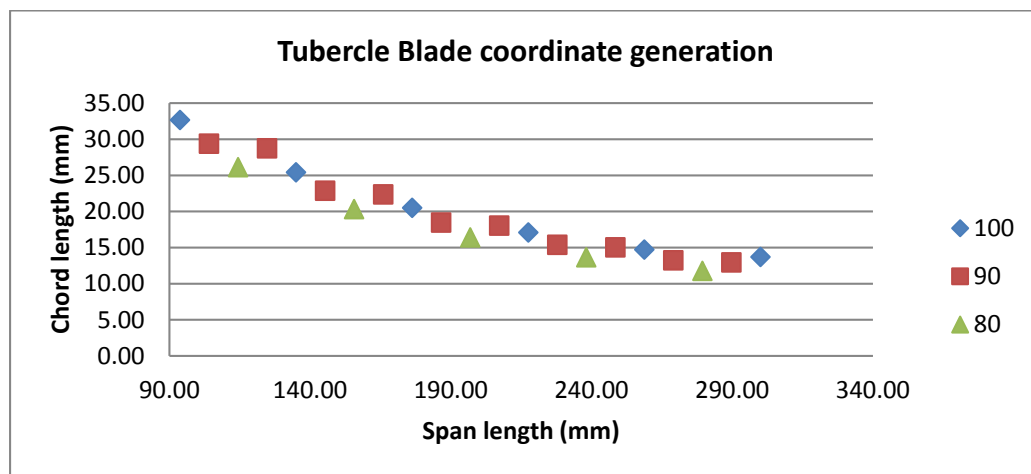


Figure 16: visualizing the tubercle blade coordinates

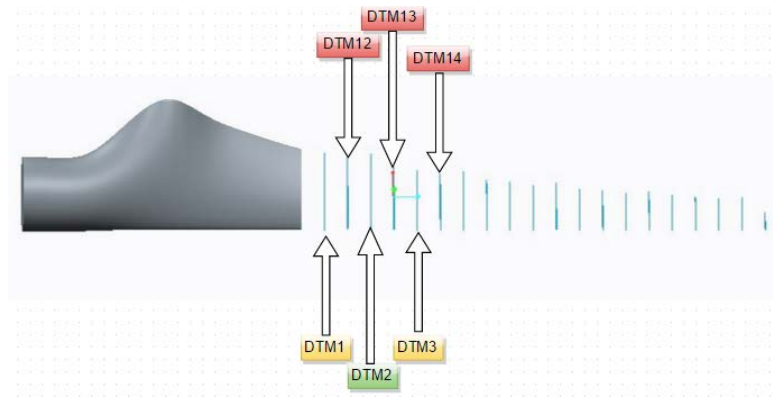


Figure 17: implementation of tabulated coordinates on straight blade to make the tubercle blade

In figure 17, the datum planes are colored by the correspondent length, found in table 5. Where yellow is chord length of the original straight blade, red corresponding to 90% chord and green corresponds to 80%.

Upstream curved Winglet Blade Design

Many wind turbine sites have a restriction on the rotor diameter in one form or the other. In those cases, the only way the power production can be optimized at any specific wind velocity is through maximizing the power coefficient (C_p) of the wind turbine (Gaunaa, M., & Johansen). Adding a winglet to the wind turbine blade improves the power production without increasing the projected rotor area. This is done by diffusing and moving the wing tip vortex (which rotates around from below the blade), away from the rotor plane, reducing the downwash and thereby the induced drag on the blade (Gupta, A., & Amano, R. S). The winglet converts some of the otherwise wasted energy in the wingtip vortex to an apparent thrust. Figure 18 shows the wingtip vortex being deflected away from the rotor plane and reduced in size in the case of the blade with a winglet attached to it, unlike the blade without the winglet.



Figure 18: Reduction in the wingtip vortex size with the blended winglet.

The six key parameters that govern the design of a winglet includes the winglet height, the sweep angle, the cant angle, the curvature radius, the toe angle and the twist angle

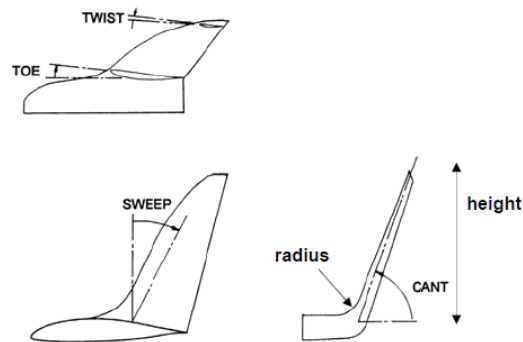


Figure 19: Key design parameters of a winglet

These parameters are shown in Figure 19. In wind turbine applications, it is more convenient to point the winglet towards the pressure side (pointing upstream) to avoid tower clearance issues. Also, some literature points out that the winglets pointing towards the pressure side give an overall better power production. After some research, it was found that studies has proven that winglets with a cant angle of 45 degrees and a winglet height of 4 percent of the rotor radius generated more power. After generating the straight blade, a winglet was added to the tip. This was done by sweeping the cross-sectional area at the blade tip along a path such that the radius of curvature of the bend was 50 percent of the

rotor radius, maintaining the cant angle of 45 degrees and the winglet height of 4 percent rotor radius. Figures 20 shows the winglet blade in various views.

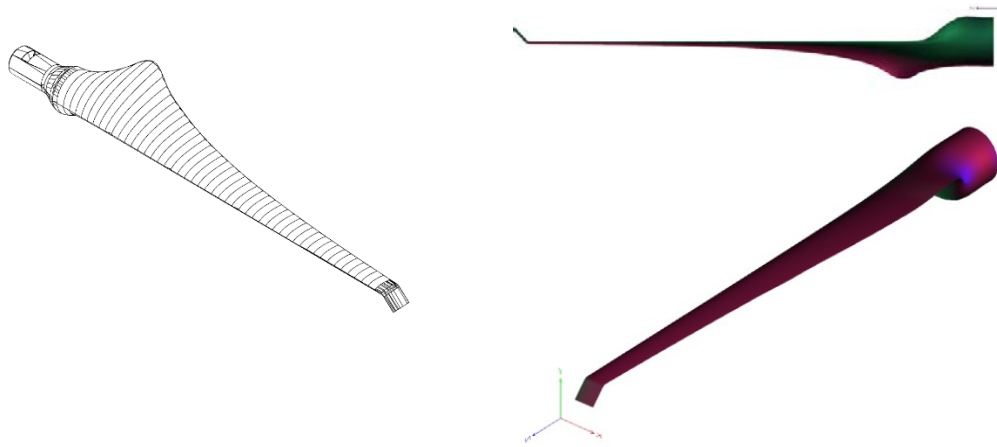


Figure 20: Different views of the winglet blade

Chapter III. Experimental Facility

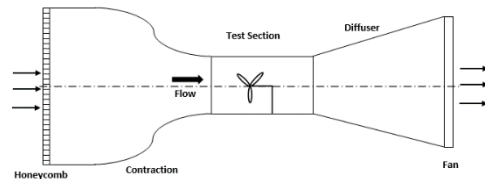
This chapter gives a detailed description of the experimental facilities, listing all devices and processes used to complete this study.

Wind tunnel Facility

The wind tunnel facility used for this study shown in figure 21, was built in 2010 and considered one of the largest wind tunnels in the United States.



a. Wind tunnel facility in UW-Milwaukee



b. Illustrative drawing of wind tunnel components

Figure 21: Wind tunnel facility and research lab at UW-Milwaukee

This wind tunnel is able to produce subsonic flows, in the range (0-25m/s) and is 12.8 meters long. The test section is 1.2x1.2 meters and 2.4 meters long. The inlet nozzle of the tunnel has 3.2x3.2m cross-section that is covered by five fine-meshed honeycomb mesh plates to foster an evenly distributed flow profile. The converging section then connects to the test section. The 40hP electric motor drives the eight blade fan at the exit; each blade is 1.8 m in radius. This wind tunnel is classified as “sucker type”, where the fan induces air through the test section at the central region of the tunnel. Air leaves the wind tunnel through a diffuser section characterized by a linearly increasing side length and square cross section.

Blades and Hub

The experimental study was based on a blade at a scale of $\frac{1}{65}$ of the 20 m commercial blade, and were used in adjacent to one hub that fits all designs, to keep the differences to a minimal. Advanced wind turbines will have hybrid airfoils that are combinations of many different airfoil types at different locations on the blade. But for comparing the effect of different alterations on the blade, the same NACA 4412 was used with all the different designs. A turbine diameter of 60 cm was chosen to ensure that the wake region effect is fully captured within the area range of the test section, i.e. no significant blockage of the test section.

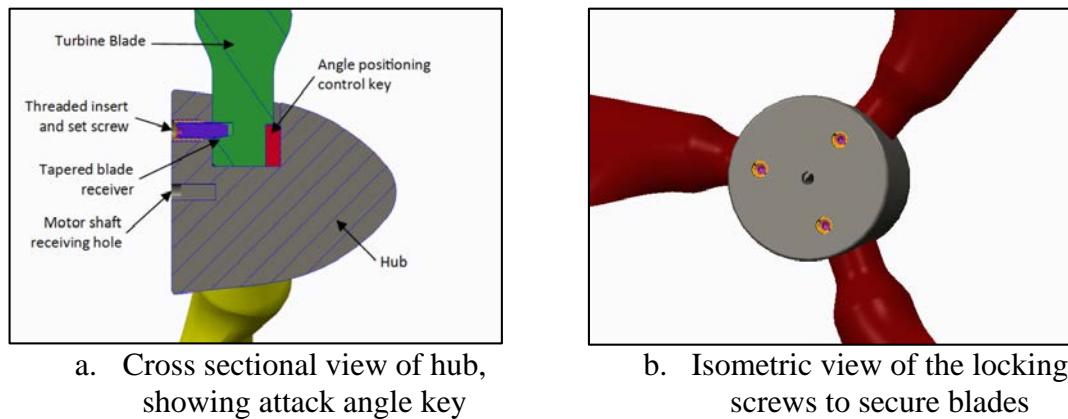


Figure 22: Different views of the Hub design

This versatile hub, depicted in figure 22, allows us to implement any wind turbine blade as well as to control the angle of attack by inserting different correspondent angle keys.

FEA, 3D Printing and materials

The 3D printing was the best choice to manufacture the blades, due to the fact that it is the best economic choice to maintain an acceptable surface resolution and to capture the geometric features. To make use of this technology, we should understand the behavior of the materials used. For this study, two 3D printing candidate materials were selected and

an FEA (Finite Element Analysis) study was performed for them. Moreover, The FEA was done on the straight blade, against the tubercle and the slotted blade design, because the winglet blade is geometrically very close to the straight blade. This study was to guide us to what is the best choice of material to be used for this desired research. Table 6 shows the properties of the materials candidates for this study:

Table 6: 3D printing candidate materials for FEA study

Material	Density(kg/m³)	Young's Modulus (MPa)	Poisson's Ratio
Renshape SL 5220 (Polycarbonate)	1,130	2,951	0.375
P430 ABS plus	1,040	2,206	0.4

This analysis investigated the deflection of wind turbine blades when subjected to the pressure load equivalent of a wind velocity delta of 15 m/s. The centrifugal force generated by the rotation of the blades will be disregarded for this study due to their negligible effect on blade deflection. Since the rotation speed will also be held at 300 RPM, the stress exerted by this force will also not be significant in generating stresses high enough to cause part failure. This difference in wind velocity can be converted to a pressure load applied to the frontal surface of the blades based on the following equation.

$$P = \frac{1}{2} * \rho * V^2 \quad (1)$$

Using an air density of 1.204 kg/m³ and a velocity differential of 15 m/s it can be determined that a pressure load of 135 Pa is being exerted on the wind turbine blades. This value was chosen by calculating the pressure applied on an object where the difference in wind speed is 15 meters per second. This means that the wind speed in front of the turbine blades should be traveling at a velocity of 15 meters per second more than the air in the wake of the wind turbine. This effect occurs when the turbine blades are traveling more

slowly than the lift generated by the blades and is achieved by applying a load to the turbine motor causing the blades to reduce their rotational velocity.

Table 7: FEA study showing Von mises stress and displacement result for straight, tubercle and slotted blade.

Blade Design	Renshape von Mises Stress	P430 von Stress	ABS Mises	Renshape Max Displacement	P430 Abs Max Displacement
Traditional	1.45 MPa	1.45 MPa		5.73 mm	7.66 mm
Tubercle	1.96 MPa	1.96 MPa		7.64 mm	10.20 mm
Slotted	3.18 MPa	3.16 MPa		5.66 mm	7.57 mm

Table 7 depicts the findings for the FEA study done for the blades. Moreover, the von Mises stress and the deflection plot for the straight blade can be found in Table 8

Table 8: Straight blade plots of deflection and Von misses stress

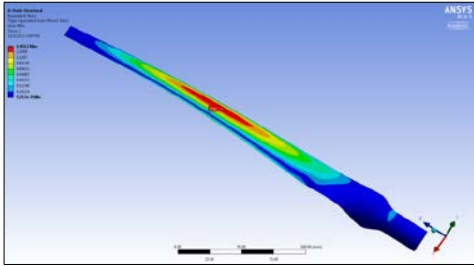
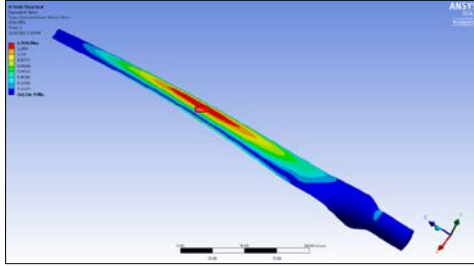
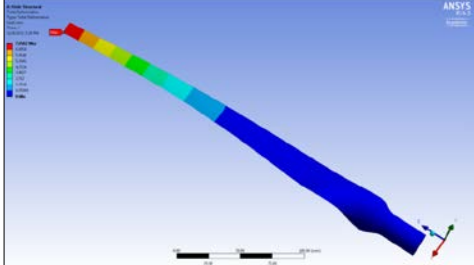
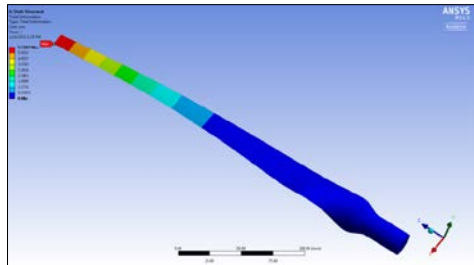
Straight blade		
Design	ABS 430	Renshape SL5220 Polycarbonate
Von Mises		
Displacement		

Table 9 shows the findings for the slotted blade from the FEA study.

Table 9: Slotted blade plots of deflection and Von mises stress

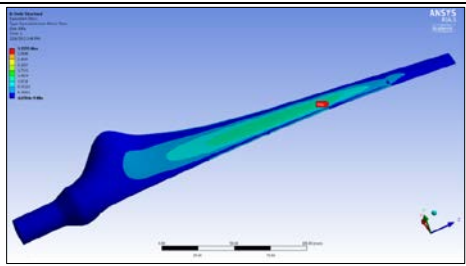
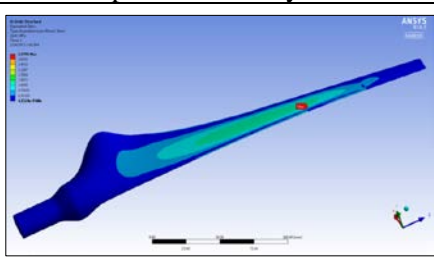
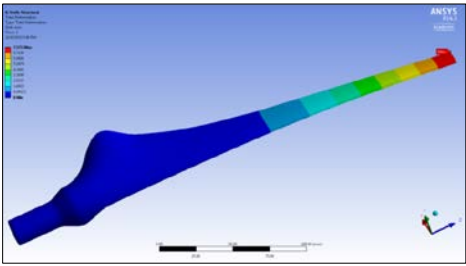
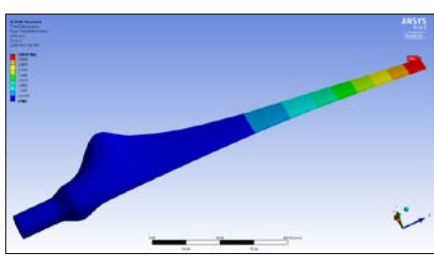
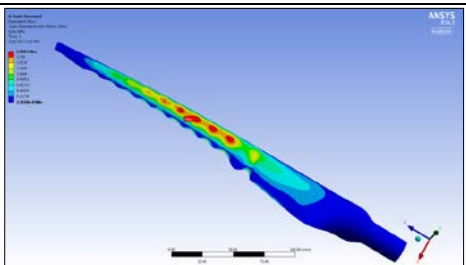
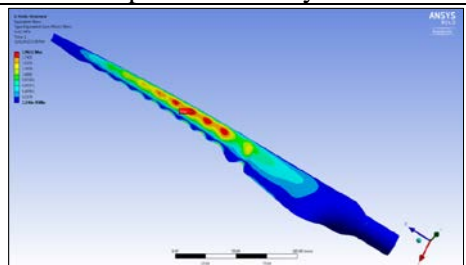
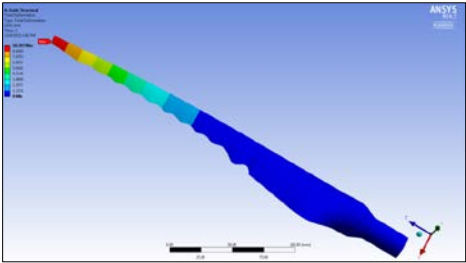
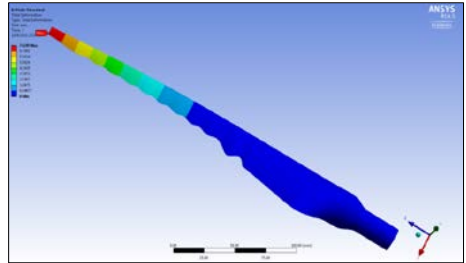
Slotted blade		
Design	ABS 430	Renshape SL5220 Polycarbonate
Von Mises		
Displacement		

Table 10 depict the resultant von Mises stress as well as the displacement values.

Table 10: Tubercle blade plots of deflection and Von mises stress

Slotted blade		
Design	ABS 430	Renshape SL5220 Polycarbonate
Von Mises		
Displacement		

The results found through the aforementioned study concluded the superior performance of Renshape material compared to the P430 ABS, which consequently was implemented for the three blade designs under experimental investigation. Finally, figure 23 shows the final blades set that was printed utilizing Renshape material and the 3D printing. In addition, the mass was measured for the three blades, and can be found in table 7.



a. Straight and tubercle blade with hub and attack angle inserts



b. (top) tubercle blade (Middle) slotted blade (Bottom) straight blade

Figure 23: 3D Printed Blades using Renshape material.

Hot Wire, Data Acquisition Devices and Wind tunnel Flow field

The airflow velocity is measured using a hotwire sensor. The hot wire sensor has two prongs, recording both the U and V components of velocity. Additionally, the anemometer is mounted on a robotic traverse system, depicted in figure 24, capable of moving in three directions within the test section.

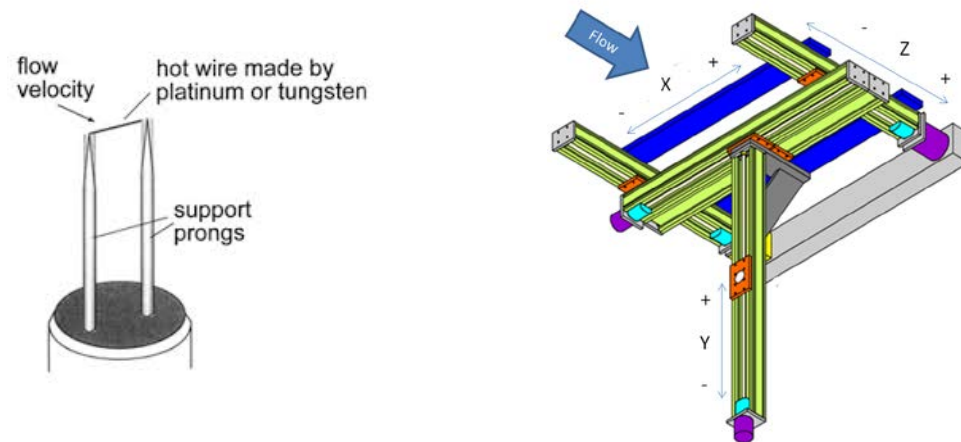


Figure 24: Hot wire anemometer used for flow field mapping and three axes robotic traverse system

The bridge voltages from the Hotwire are acquired via fast Analog/Digital Data Acquisition (A/D DAQ) boards (up to 1 MHz, 5kHz was used in this research) after proper low-pass filtration the data are then converted to velocities by utilizing calibration curves generated prior to any experiment as an experimental routine, a sample from the calibration curve is provided in figure 25.

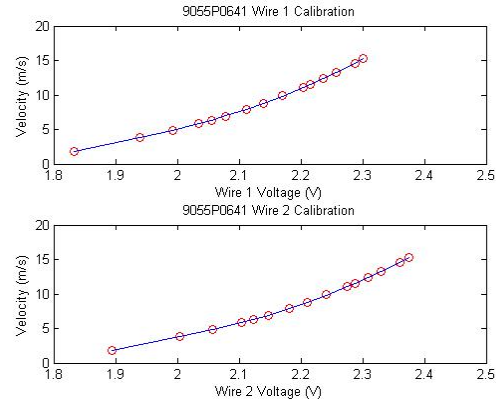


Figure 25: Sample calibration curve for the hot wire sensors U and V components

The traverse system is designed for high-resolution plane capturing, up to 3.6 K measurement node per plane, with a 12.7 mm minimal increment, figure 26.

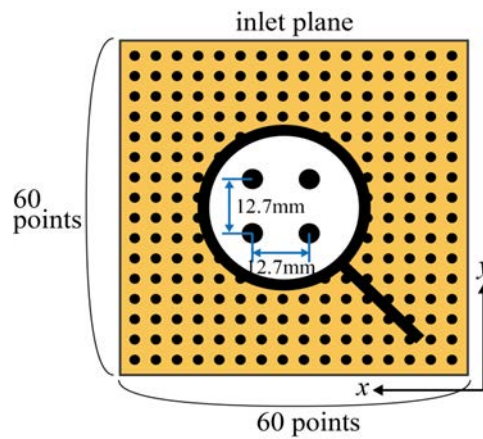


Figure 26: Robotic traverse system resolution demonstration

Hotwire is calibrated by establishing a relation between voltage output and the flow velocity, calibration enables converting the measured voltage data to velocity. It is performed with a dedicated calibrator. The relative standard uncertainty of the calibrator can be expressed as:

$$U(U_{\text{cal}}) = \frac{1}{100} (\pm 1\% \pm 0.02\text{m/s}) \quad (2)$$

The temperature variations from calibration to experiment or during an experiment introduces systematic errors. Since the velocity U_{cal} actually represents the mass flux, ρu ,

variations in density, ρ , temperature will add to the uncertainty. The relative standard uncertainty due to temperature can be expressed as:

$$U(U_{\text{temp}}) = \frac{1}{\sqrt{3}} \cdot \frac{\Delta T}{273} \quad (3)$$

As depicted in figure 27, the boundary layer in a wind tunnel changes when a wind turbine is installed. It is important to understand the capabilities of the wind tunnel facility and how the flow field change as we incrementally move further downstream from the wind turbine. For this purpose, four measurements of the flow were mapped on four planes behind the wind turbine.

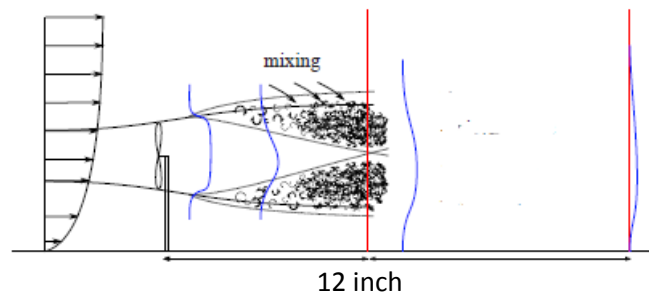
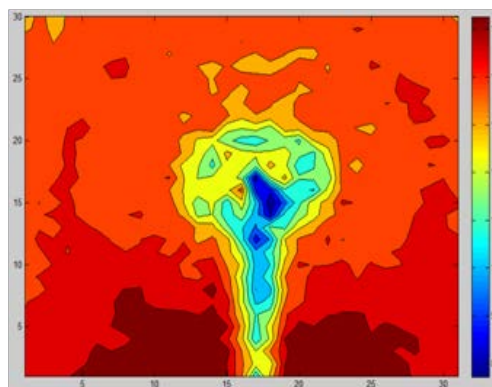
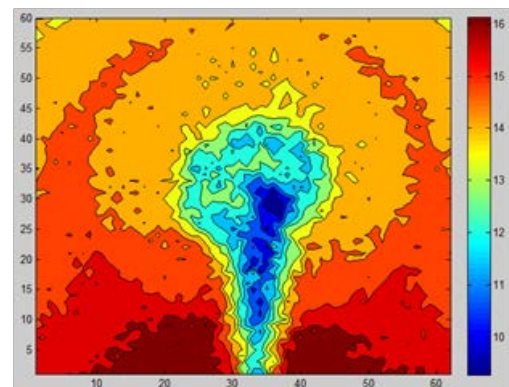


Figure 27: Wind tunnel boundary with the wind turbine installed

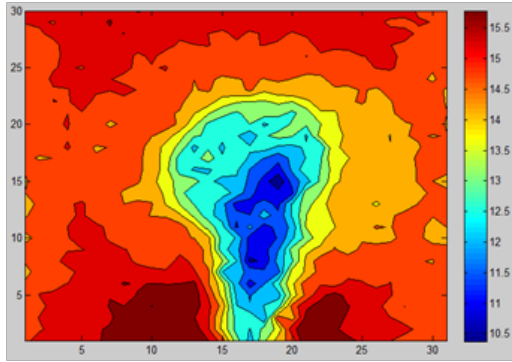
These measurements in figure 28, were taken at 6, 12, 24 and 36 inches behind the wind turbine. Turbulence intensity was also calculated with a high-speed DAQ system and was found to be 1.5% maximum for all velocity ranges.



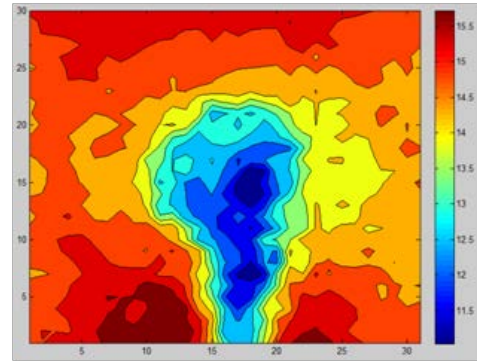
a. Experimental flow mapping, 6in behind wind turbine



b. Experimental flow mapping, 12in behind wind turbine



c. Experimental flow mapping, 24in behind wind turbine



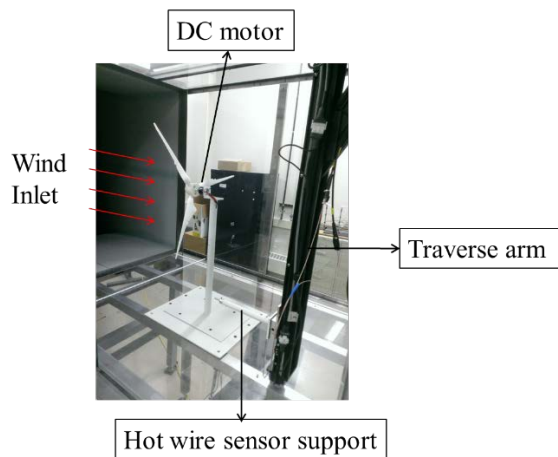
d. Experimental flow mapping, 36in behind wind turbine

Figure 28: flow field mapping of velocity behind the wind turbine.

After plotting these contours of velocity, it became apparent that the best resolution of the flow would be achieved measuring the velocities at 12 inches from the wind turbine.

Chapter IV. Experimental Procedures

In this chapter, the details of the experimental procedures done to complete this study are explored. It is important to note that the different blade designs were mounted on a hub that was constructed to accommodate all the four different blade designs to ensure the uniformity of test parameters. The hub constructed fits on a DC brushless motor, which generates the electrical power. The output from the motor was monitored using Data acquisition devices to determine the power generated by the wind turbine blades. The motor was placed on a tower, seen in figure 29, to hold the assembly. The tower height was 57 cm with a diameter of 4 cm. This tower was placed 84 cm away from the inlet section, and placed 61 cm away from both side walls of the test section.



a. Testing apparatus in wind tunnel test section



b. Wind turbine blade mounted on motor and column

Figure 29: testing apparatus and wind turbine blades connected to the measurement column

Power Extraction

The power extracted was measured by observing the generated voltage utilizing a data acquisition device called National instrument NI9215.

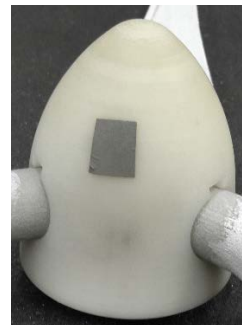


Figure 30: National instrument NI 9215 Analog Data acquisition device.

This device seen in figure 30, can monitor analog inputs as well as logging the data at very high rate, with high accuracy. This device was used to monitor the voltage output from the generator plotted against the time duration of the test. The rotational velocity was monitored using a tachometer device called MONARCH PLT200. This device can be seen in figure 31, where it uses a laser beam which is pointed at a refractor sheet, this sheet repels the laser beam per rotation, and is monitored by an optical sensor. The tachometer was placed on the outside wall of the test section, at a constant location throughout the study, and the refractor sheet was placed on the universal hub, to decrease the error of the experiment.



a. Monarch Tachometer



b. Refractor sheet on the hub

Figure 31: Monarch tachometer used to monitor the angular velocity at the hub.

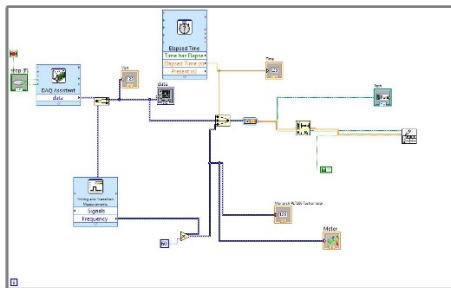
In order to increase the experiment accuracy, the voltage and angular velocity data has to be taken simultaneously, and for that reason, a second data acquisition device is introduced. The job of such data acquisition device is to read the output from the tachometer, which is

digital, then convert this data to angular velocity. The device used was National Instrument NI9402 depicted in figure 32.

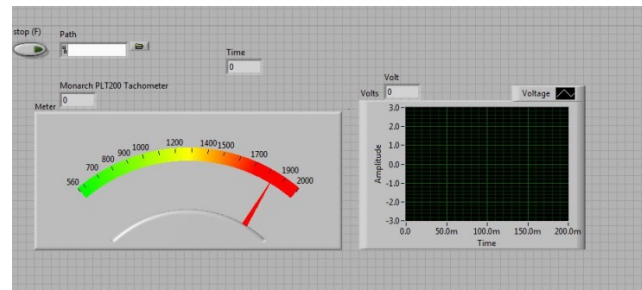


Figure 32: National instrument NI 9402 Digital Data acquisition device

After compiling the above mentioned devices, one needs to join all acquisition systems together. Particularly for that reason, a dedicated program was designed to interface the data and log them across time. For the programming, Labview program was used to interface and log the data with respect to time. Figure 33 shows the building blocks for the program.



a. block diagram



b. User interface

Figure 33: Labview program designed for voltage, RPM and time logging

In order to measure power from wind turbine, a load has to be applied, resembling an obstacle for the wind turbine to overcome, which can be a measure of performance. The load in this case is simulated by an electrical resistance, neglecting the mechanical losses. For this study, five discrete values of resistance were selected, corresponding to (0.2, 0.3, 0.5, 1.0 and 2.0 Ohms). Electrical power is derived from the following equation:

$$P = \frac{V_{RMS}^2}{R} \quad (4)$$

From an electrical point of view, running a current through a resistance generates heat. As equation 4 shows, the power is proportional to the inverse of the resistance, meaning the less the resistance value, the more power generated and the more hardship the wind turbine witness. One thing to note, the voltage acquired is in the shape of a sinusoidal wave, where the voltage oscillates between two distinct values. This is not the practical voltage used to calculate the power, thus, a Root Mean square (RMS) voltage has to be applied by equating the V_{RMS} using the following equation:

$$V_{RMS} = \frac{V}{\sqrt{2}} \quad (5)$$

Experimental power calculation

Every flow stream possesses energy, and this energy can be harvested in many ways. By applying the well-known Albert Betz theory we can understand the behavior of the blade designs. The difference in the flow stream energy before and after the test wind turbine can be determined for an ideal case, and, as a result, the energy harvested by the system can be captured. By using Equation 6 the mass flow rate is obtained, since the upstream flow velocity is known.

$$\dot{m} = \rho v A \quad (6)$$

Equation 7 provides the volumetric flow rate of the air stream.

$$\dot{V} = v A \quad (7)$$

These two equations are then used to calculate the kinetic energy possessed by the flow using Equation 8.

$$E = \frac{1}{2} m v^2 \quad (8)$$

Equation 9 is the result of combining the three previous equations which gives the amount of energy passing through a cross-section per time period.

$$P = \frac{1}{2} \rho v^3 A \quad (9)$$

If the wind velocity is measured right before the turbine and after the turbine, the amount of energy the turbine acquires from the wind can be determined by utilizing Equation 10.

$$P = \frac{1}{2} \rho (A_1 v_1^3 - A_2 v_2^3) \quad (10)$$

Taking into consideration that the area is the same, before and after the wind turbine, the mass flow rate as a common factor for both cases, before and after the wind turbine gives Equation 11.

$$P = \frac{1}{2} \dot{m}(v_1^2 - v_2^2) \quad (11)$$

This gives the analogy that the wind turbine power production is related to the air velocity before and after the wind turbine and the bigger the difference, the more power extraction to take place.

Flow Mapping

The first step in mapping the flow field, using a hot wire, is to construct a calibration curve for the voltage difference witnessed by the data acquisition. In order to calibrate the hot wire, a special calibrator is used. The calibrator is shown in figure 35.



a. Calibration of the U component



b. Calibration of the V component



c. Calibrator used with Air flow meter and volt meter to construct calibration curve

Figure 34: Dedicated hot wire calibrator.

After the calibration, a fourth order calibration curve is constructed for each member of the flow, (i.e. U and V components), and the constants are acquired. The calibration polynomial is expressed as:

$$U = C_0 + C_1 E_{corr} + C_2 E_{corr}^2 + C_3 E_{corr}^3 + C_4 E_{corr}^4 \quad (12)$$

Where C_0 to C_4 are calibration constants.

The values of the constants then are fed into MATLAB program designed to post process the data, generating contours of velocity and turbulence intensity.

The flow was mapped using the hot wire anemometer, in conjunction with the Travers robotic system. For this purpose, a program was built to integrate both devices to work simultaneously, seen in figure 36. The program is designed to control the motion of the three motors controlling the travers arm as well as to control the CTA anemometer, which is the device that control the temperature of the hotwire element. The physical connection diagram is depicted in figure 37.

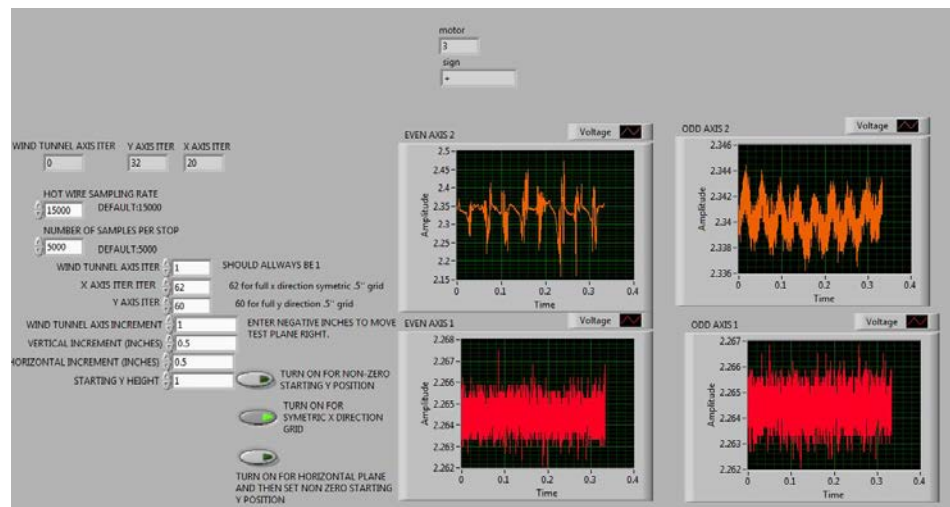


Figure 35: Hot wire and travers controlling program

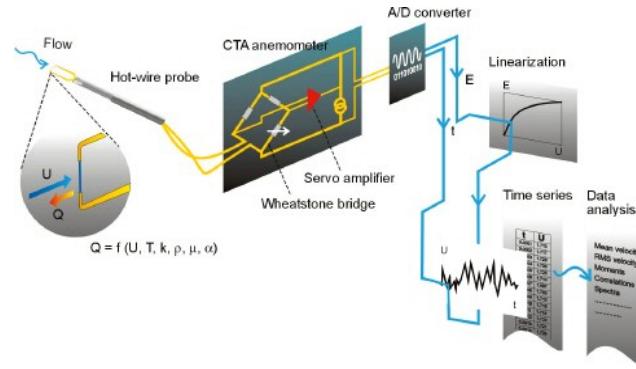


Figure 36: hot wire acquisition system

The flow was mapped at two discrete positions throughout the study, the inlet section of the wind tunnel, as well as 12 inches behind the wind turbine tower, due to reasons discussed in chapter III. The mapping of the flow took place over a range of wind velocities to determine the power coefficient (C_p) for each blade. This coefficient is found by equating the energy possessed by the flow stream before the turbine, using equation 9, comparing it to the energy present in the flow right behind the wind turbine. The C_p is calculated using equation 13:

$$C_p = \frac{P_{pre-turbine}}{P_{post-turbine}} \quad (13)$$

Where $P_{pre-turbine}$ depicts the power present in the mapped flow taken in the inlet section of the wind tunnel and $P_{post-turbine}$ is the power in the field right behind the wind turbine.

Chapter V. Computational Fluid Dynamics (CFD)

A complete three-dimensional computational fluid dynamic (CFD) analysis was performed for a blade of $R = 0.3$ m rotor radius. This was done to each of the designs discussed in Chapter II - slotted blade, winglet blade and tubercle blade - including the straight blade CFD analysis for comparison purpose. The goal for this CFD investigation is to find the torque generated due to the flow driving the wind turbine blade, which is going to be used to determine the power output using the following equation:

$$P = \tau\omega n \quad (14)$$

Where P is the power generated in Watts, ω is the angular velocity in radians/seconds and n is the number of blades desired on the wind turbine.

Computational Domain Construction

A simplified case was considered for numerical simulations with only one-third of the flow region (120 degrees sector). This domain consisted of a single blade attached to the hub with the effect of the tower being ignored, as depicted in figure 38.

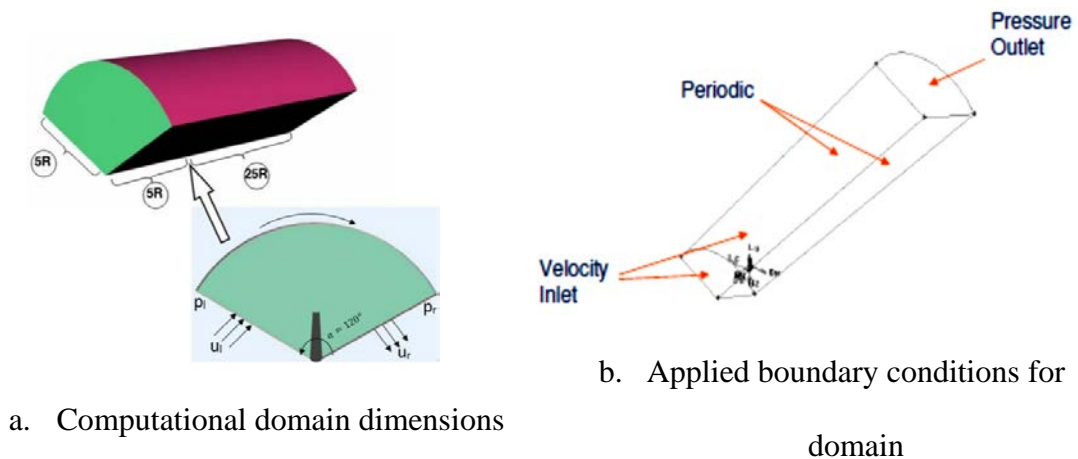


Figure 37: computational domain

A periodic boundary condition was assigned to each side of the domain. The front facing and the top arc planes were given as velocity inlets, for the front plane, the vectors were in the normal direction, as for the arc, a specified direction was set, moving the velocity vectors in plane, forward towards the blade. The rear plane was considered as a pressure outlet boundary condition. The computational domain stretched $5R$ upstream, equivalent to 1.5 m from the blade and $25R$ downstream, equivalent to 7.5 m. Both the inlet and the outlet regions at upstream and downstream, respectively, had a radius of $5R$. This size of the domain was selected in order to eliminate the effect of boundary conditions on the flow around the blade.

The periodic boundary conditions are intended to ensure that the flow conditions are exactly the same on both sides of the domain. The computational domain was given a rotational speed, different for each wind velocity, about the y-axis. By keeping the blade at rest and setting the complete fluid volume to motion, this has the same effect as when the blade was in motion, and is referred to as flow induced motion. This was done to avoid the complexity of dynamic meshing, which involves more computational power. The upstream and the radial surfaces were specified as velocity inlets. The velocities were determined in component form with specified magnitude, directing the flow in the axial direction. The downstream boundary was specified as a pressure outlet where a zero gauge pressure was set. The hub and the blade surfaces were considered as walls with a no-slip condition.

Mesh Generation

The accuracy of the CFD solution depends on the quality of the grid used to perform the calculations. A fine mesh is required near the wall regions to resolve accurately near-wall

viscous effects while a coarser mesh is sufficient away from the wall to maintain Computational efficiency in wake regions. For this analysis, the area of interest is the region surrounding the aerodynamically active portion of the blade. A structured mesh was deployed along the computational domain, and a mesh refinement took place near the blade. The straight blade will be used as a sample for demonstrating the mesh used for this study. Figure 39 shows the mesh constructed for the straight blade as a sample for the CFD study.



a. Computational domain mesh

b. Transparent wireframe showing the blade inside the computational domain

Figure 38: Straight blade computational domain mesh

A very fine structured mesh was implemented for the region near the blade surface. Since the finer mesh yields more accurate results due to its superiority in implementation of the low-Reynolds number models in the near-wall region. On the other hand, the outer region where the flow is mostly vortex and/or potential flow, a less refined mesh was employed. A structured mesh was generated such that a y^+ value of approximately 1 was achieved on the blade surface, which is suitable for boundary layer resolution. Figure 40 shows the mesh generated for the (a) straight blade, (b) winglet blade, (c) tubercle blade and (d) slotted blade.

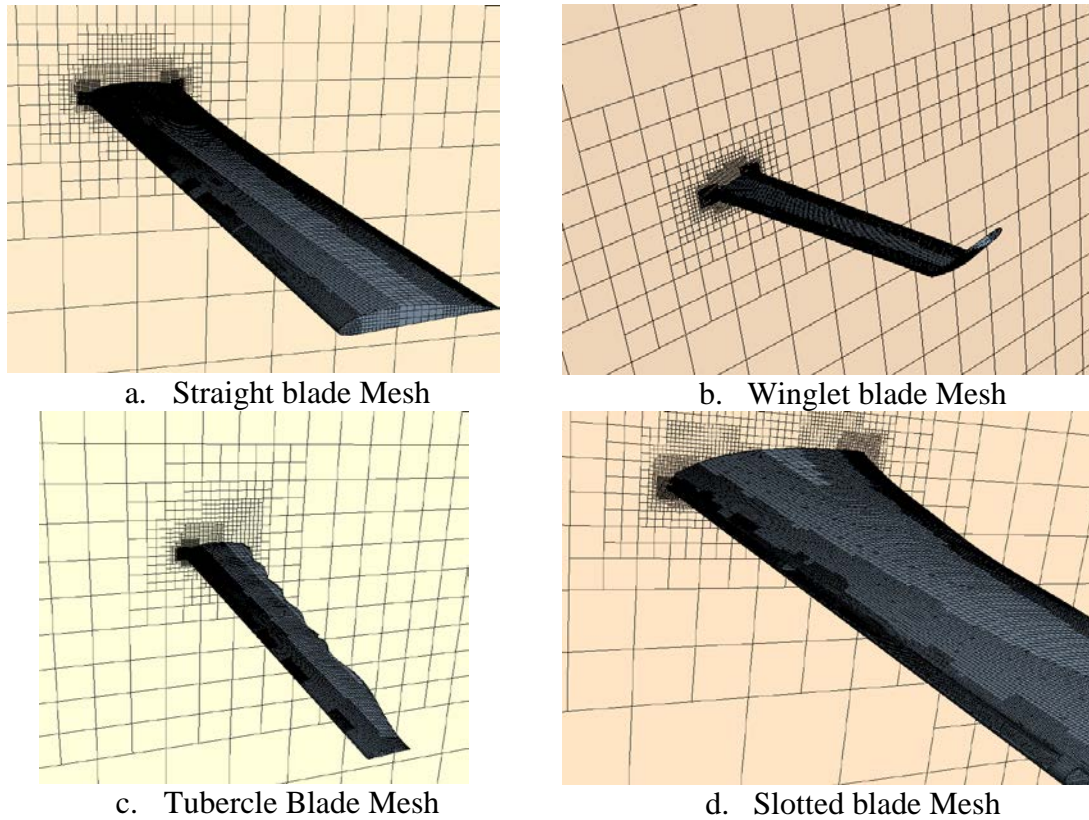


Figure 39: Mesh deployed for all blade designs

The mesh statistics for different designs can be seen in Table 11. It can be seen that the slotted blade needed a more refined mesh. The reason for this increase was to deploy more mesh within the slot channel, in order to capture the flow passing through the slots, while other designs were kept in the same mesh scale.

Table 11: Mesh statistics for different blade designs.

Mesh statistics	
Design	Mesh cell count
Straight Blade	5,582,929
Slotted blade	5,205,179
Tubercle blade	5,273,957
Winglet blade	5,871,116

Turbulence model selection

The choice of turbulence model significantly affects the accuracy of the solution. Extensive research has been done to evaluate the turbulence models for the prediction of

wind turbine aerodynamics. It was observed that the $k - \omega SST$ turbulence model is one of the most suitable models for capturing the flow physics around the wind turbine blades because of its capability of considering all three-dimensional secondary flow effects and non-isotropic turbulence. Good predictions for the adverse pressure gradients and separating flow have been reported by researchers who employ $k - \omega SST$ model. Based on these advantages this model was deployed. For the present study the $k - \omega SST$ model was chosen for all the simulations performed for the various blade designs. Computations were performed using the Star-CCM+ software assuming a steady, incompressible and isothermal flow.

Grid independence Test

The grid independency test was performed on two designs, the straight blade, and the slotted blade. The slotted blade was tested under three mesh grids, 3.5, 5 and 7.2 million cells respectively. The torque generated was selected as a factor to conclude the grid independency test results. Figure 41 shows the test results for the slotted blade, where it can be seen that the line is coming to a plateau as the cell count moves beyond 5 million cells.

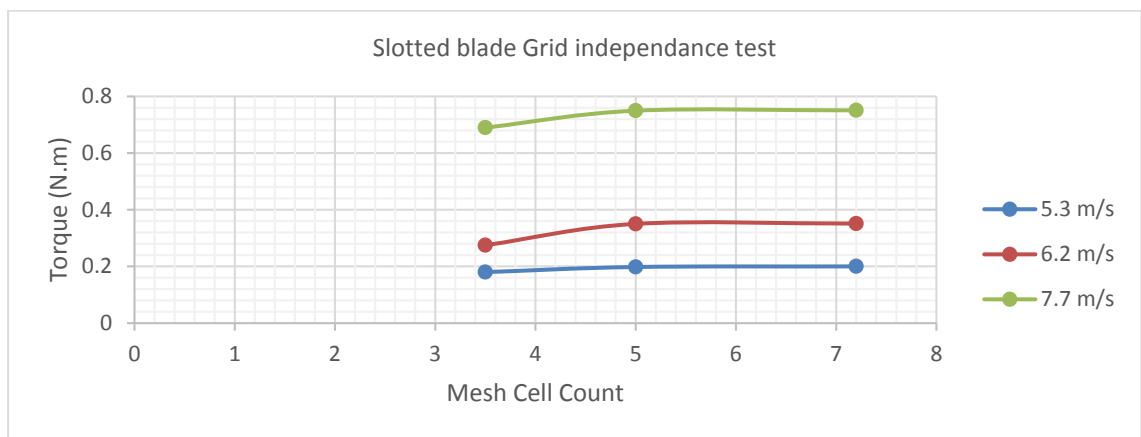


Figure 40: Slotted blade grid independency test

Additionally, Figure 42 shows the grid independent study performed on the straight blade with 3.2, 5.5 and 7 million elements. It was found that the accuracy of results changed less than 5% for a higher sized mesh and so to save computational efforts the 5.5M size was used.

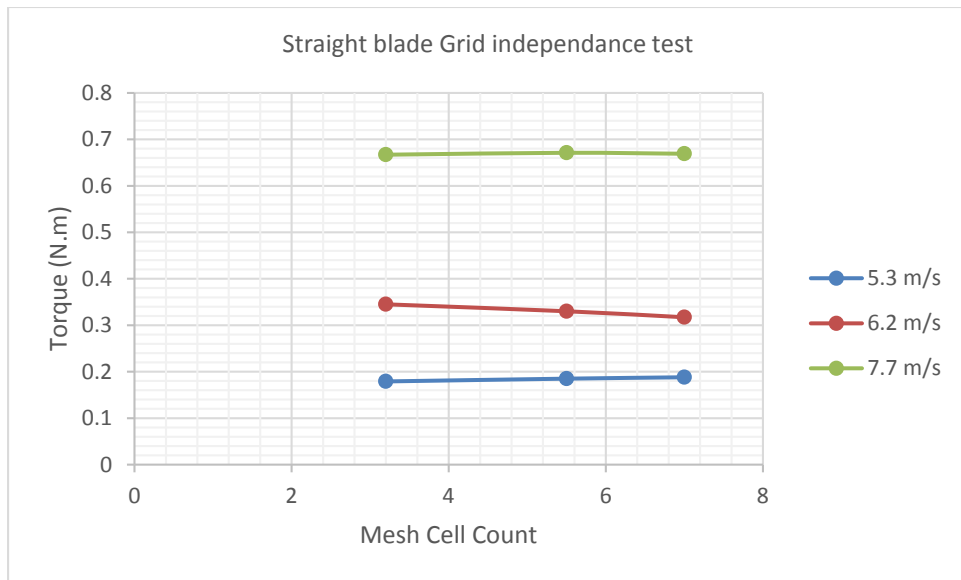


Figure 41: Straight blade grid independency test

Chapter VI. Results

This section presents the results of experimental and numerical investigations. Where the experimental work covered the straight, slotted and tubercle while the CFD was done for all designs. The 3D printing performed for the three blades was of high accuracy, resulting in the straight, slotted and tubercle blade. The winglet, on the other hand, was outsourced to a different supplier, resulting in a less efficient finish. The concern here was that this print had different mechanical properties, weight is one major concern, so it was opt-out from the experimental work to maintain a high level of experiment integrity.

Experimental results

The experimental work done for this study is tabulated here, comparing the behavior of slotted, tubercle and straight blade, in means of power, angular velocity, torque, Tip Speed Ratio (TSR), the coefficient of performance (C_p) and turbulence intensity contours. This was done utilizing the varying resistance method, and flow field mapping, where the findings are presented in this section.

In this study, the blades had to produce energy in the form of heat leaving the body of the resistance, which was connected to the output of the wind turbine motor. This method was inferred by the work of Jason R Gregg, who tested the performance of small-scale wind turbines. The resistances used for this study were 0.2, 0.3, 0.5, 1.0 and 2.0 Ω respectively. It is important to note that the least resistance value should produce the most energy, for reasons discussed in Chapter IV. The voltage then is measured across the resistance to monitor the voltage and conclude the energy production. The results presented here were measured over three trials, and averaged among them. To start, it is important to characterize the behavior of the blades under various resistive loadings holding the velocity

at a constant, in order to understand the peak power generation. For this demonstration, the slotted blade and the straight blade were chosen.

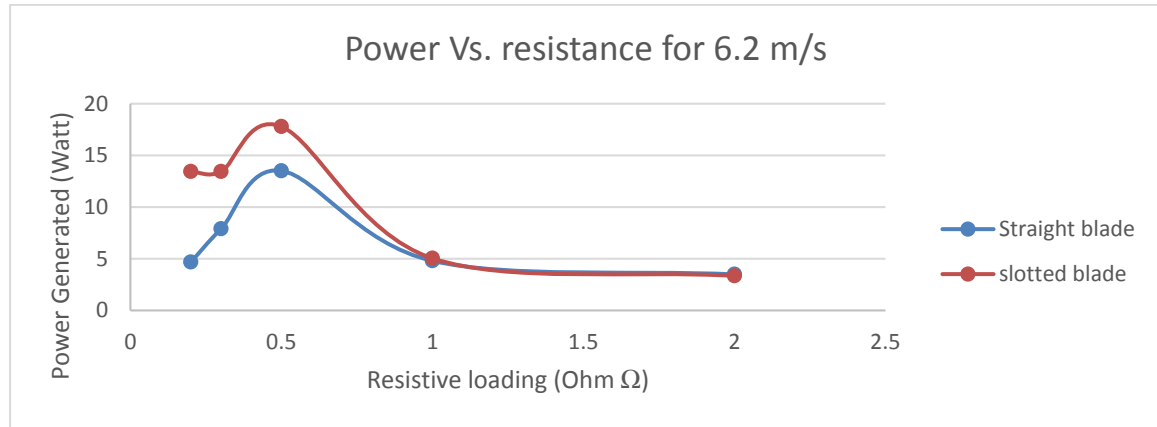


Figure 42: Power Extracted Vs. Resistive loading at 6.2 m/s

From Figure 43 we can see that the maximum power is generated when a resistance of 0.5Ω is used. This is confirmed by the two designs, slotted and a straight blade. This finding complements the observed behavior of the power generation employing this resistance. The power generation curve tend to have more linear behavior along different velocities, so for this analysis, the power tabulated , utilized the 0.5Ω resistance as a load. The complete data set for the findings using different resistance values will be provided in the appendix A.

Straight blade (Control)

The straight blade was constructed as a baseline to understand the impact of the alterations done producing the slotted, and tubercle blade. Here, the behavior of the straight blade is tabulated in means of power, angular velocity, torque, Tip Speed Ratio (TSR), the coefficient of performance (C_p) and turbulence intensity contours. These factors are then used as a comparison reference. The power extracted from the straight blade can be seen

in figure 44, where a constant increase in power production can be observed, as the velocity increases.

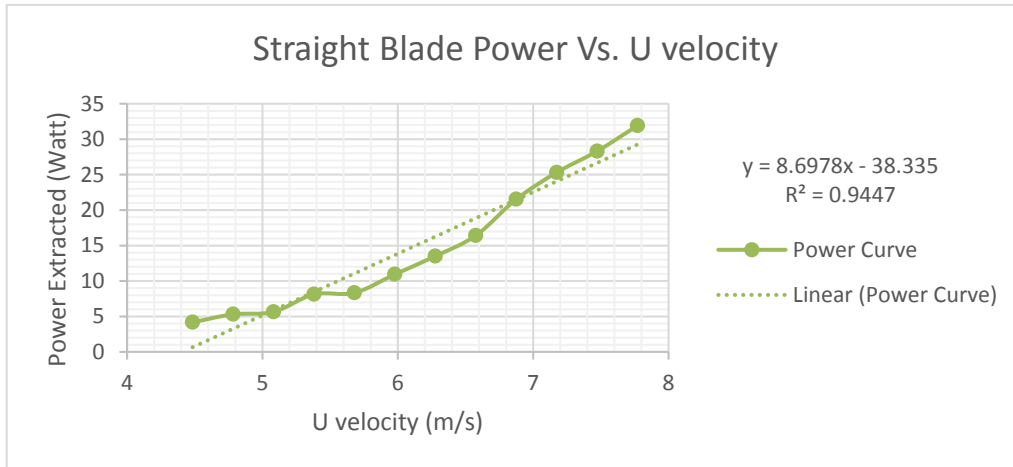


Figure 43: Power Extracted from Straight blade using different velocities

This power depicted in figure 44 was directly measured from the motor, across the resistance, using the data acquisition devices. This was done utilizing both equation 4 and 5. The Angular velocities was also measured, using the tachometer, logging the data with the acquisition devices.

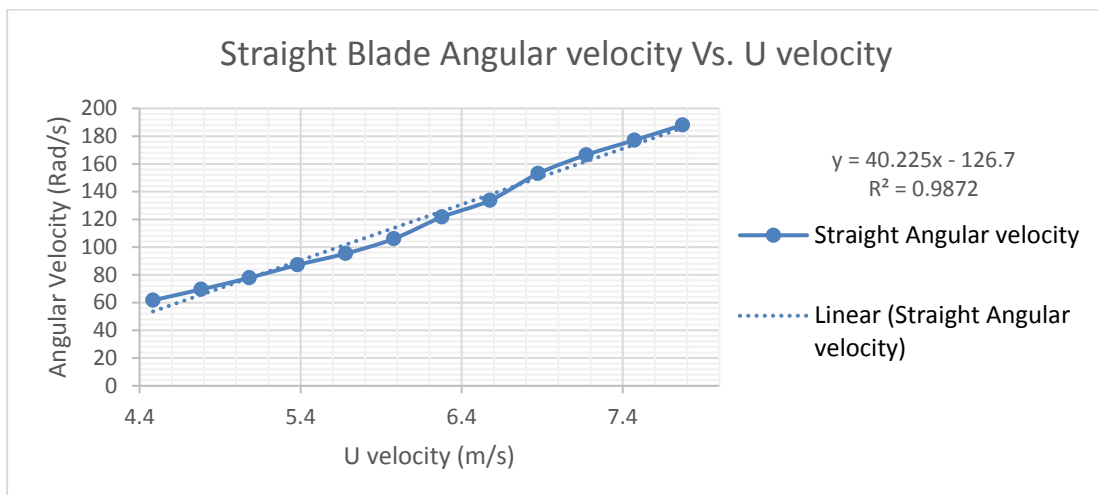


Figure 44: Straight blade Angular velocity Vs. U velocity

Figure 45 shows the Angular velocity readings, measured at the hub. These readings corresponds to the power measured, where each value was taken simultaneously with the power at that discrete velocity value. These values of angular velocity are then used to determine the torque generated, utilizing equation 14. Now, manipulating this equation to solve for the torque, we get

$$\tau = \frac{P}{\omega n} \quad (15)$$

Where τ is the torque, P is the power, ω is the angular velocity and n is the number of blades, 3 in the case of this study. Now, using equation 15 to determine the torque, we get

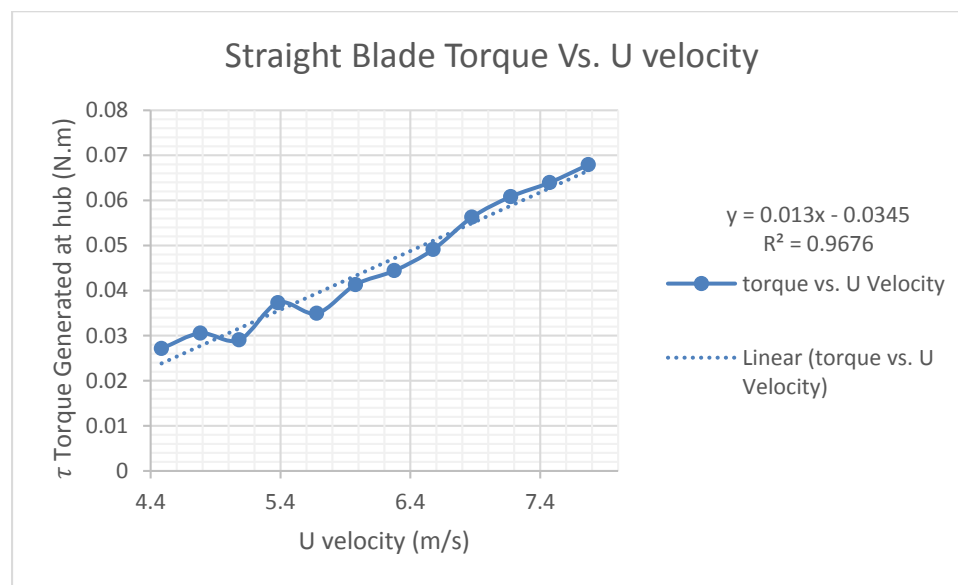


Figure 45: Straight Blade Torque Generation

The straight blade as observed from figure 46, showed a consistent increase in torque generation, hence the constant increase in power, which was measured carefully, as the error is minimal.

The Tip speed ratio, (TSR) is the ratio between the tangential velocities, as oppose to the incoming velocity, which is a dimensionless number to quantify the efficiency of a blade to capture the wind. The TSR is equated using the following equation:

$$TSR = \frac{\omega r}{U} \quad (16)$$

Where ω Here stands for the angular velocity in (Rad/s), r is the radius of the blade in (m), constant for all blade designs equal to 0.3m, U is the incoming velocity. (m/s)

Figure 47 depicts the TSR values of the straight blade.

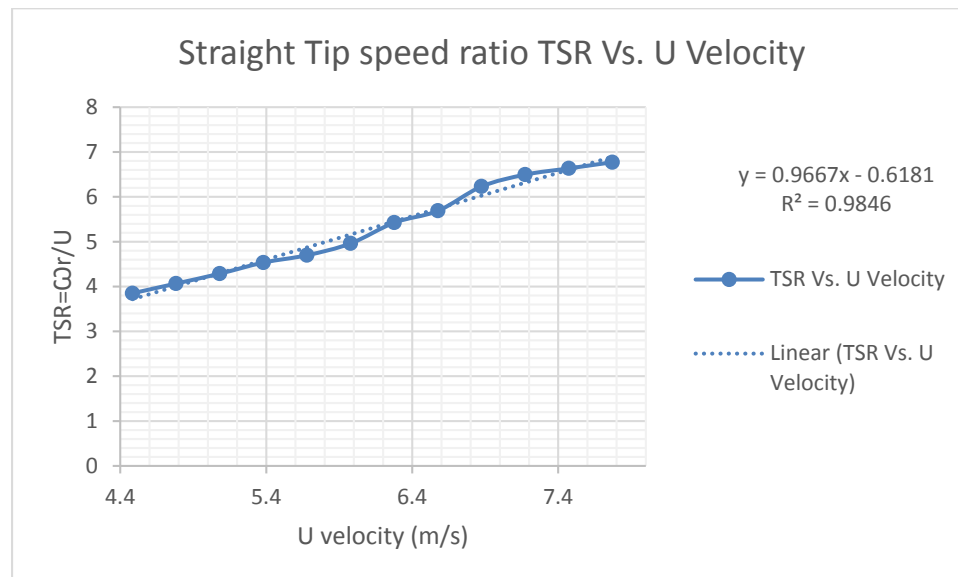
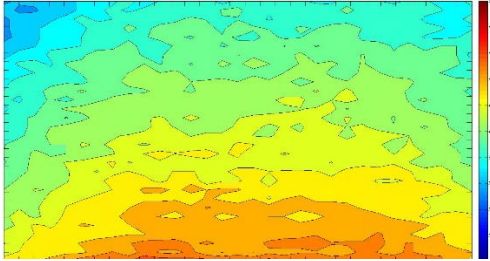
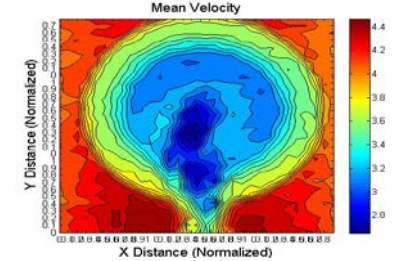
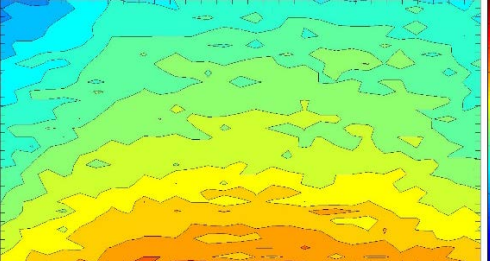
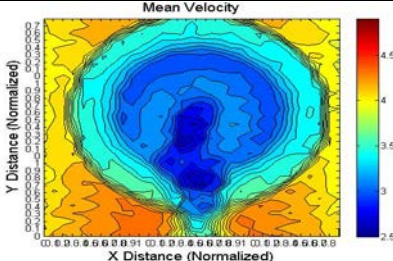
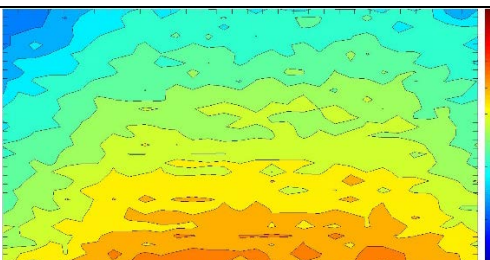
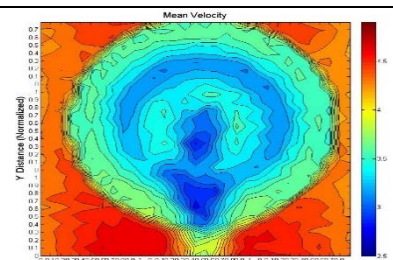
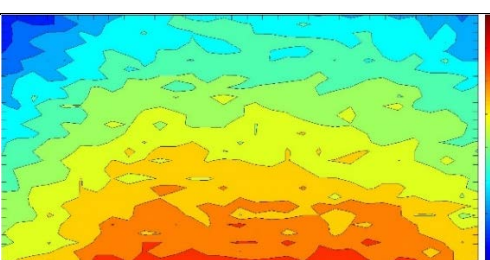
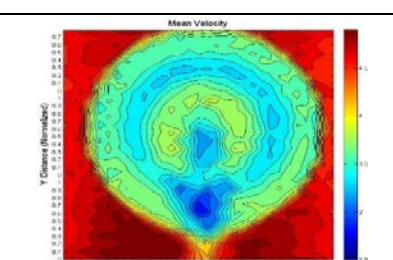
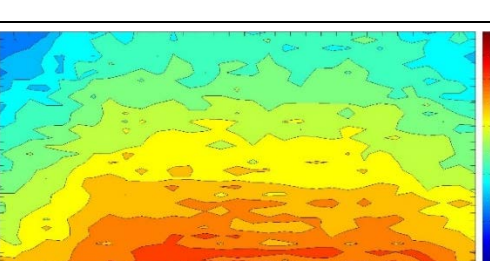
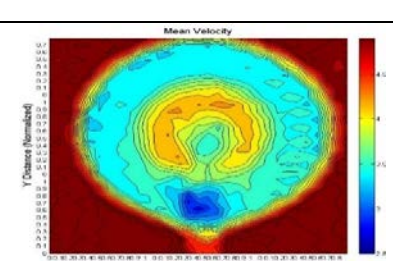


Figure 46: Straight Blade Tip Speed Ratio

The values of TSR collected from the straight blade obeys the optimal TSR range found in many wind turbine literature, where it was found to be in the range (3.8-6.7).

Now, moving to the flow field, where the field is analyzed for the coefficient of performance

Table 12: Flow Field Mapping for Straight blade at different velocities, taken at inlet section of wind tunnel and 12in behind wind turbine

Velocity	Before Wind Turbine	After Wind turbine
4.78 m/s		
5.08 m/s		
5.38 m/s		
5.67 m/s		
5.97 m/s		

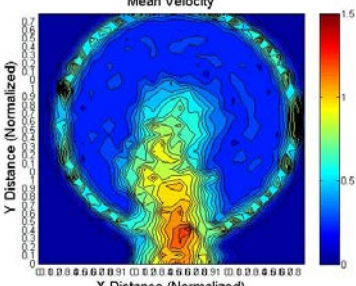
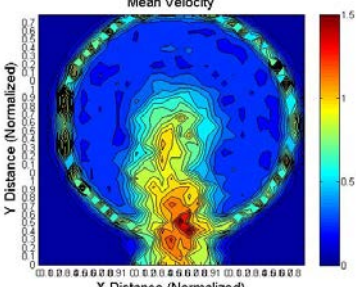
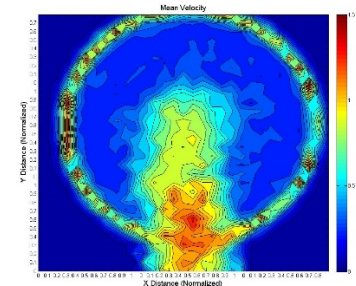
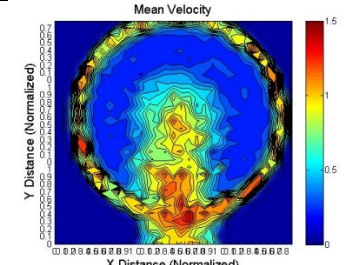
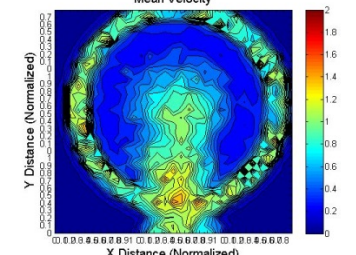
The flow field mapping was done using a hot wire anemometer to understand the energy drop across the wind turbine. The energy possessed by the flow is equated using equation 9 and then compared to the initial flow, taken at the inlet, and the flow behind the wind turbine. This drop in energy was discussed by Albert Betz, in means of conservation of mass and energy, where he tabulated his theories concluding with the Betz limit. This theoretical limit equivalent to $1/3$ or 0.593 was derived by mathematical manipulation and curve optimization which dictates the maximum achievable efficiency of a wind turbine. Using the flow field mapping presented in table 12, we were able to calculate the energy drop to conclude the Coefficient of performance as per as Betz Limit theories in table 13.

Table 13: Straight Blade Cp Values

	Straight blade Coefficient of performance					Average Cp Value
Velocity (m/s)	4.782	5.081	5.380	5.679	5.978	
C _p	0.199	0.418	0.409	0.390	0.377	0.359

The turbulence intensity was measured in order to understand the behavior of the blades and is presented in Table 14.

Table 14: Straight blade Turbulence intensity

Velocity	Turbulence intensity
4.78 m/s	 <p>Mean Velocity contour plot showing turbulence intensity distribution for a velocity of 4.78 m/s. The plot is circular with X and Y distances normalized from 0 to 1.0. A color scale on the right ranges from 0 (blue) to 1.5 (red). The highest intensity (red) is concentrated in the lower half of the circle.</p>
5.08 m/s	 <p>Mean Velocity contour plot showing turbulence intensity distribution for a velocity of 5.08 m/s. The plot is circular with X and Y distances normalized from 0 to 1.0. A color scale on the right ranges from 0 (blue) to 1.5 (red). The highest intensity (red) is concentrated in the lower half of the circle.</p>
5.38 m/s	 <p>Mean Velocity contour plot showing turbulence intensity distribution for a velocity of 5.38 m/s. The plot is circular with X and Y distances normalized from 0 to 1.0. A color scale on the right ranges from 0 (blue) to 1.5 (red). The highest intensity (red) is concentrated in the lower half of the circle.</p>
5.67 m/s	 <p>Mean Velocity contour plot showing turbulence intensity distribution for a velocity of 5.67 m/s. The plot is circular with X and Y distances normalized from 0 to 1.0. A color scale on the right ranges from 0 (blue) to 1.5 (red). The highest intensity (red) is concentrated in the lower half of the circle.</p>
5.97 m/s	 <p>Mean Velocity contour plot showing turbulence intensity distribution for a velocity of 5.97 m/s. The plot is circular with X and Y distances normalized from 0 to 1.0. A color scale on the right ranges from 0 (blue) to 2.0 (red). The highest intensity (red) is concentrated in the lower half of the circle.</p>

It was found that in the depicted range of velocities, the maximum value of turbulence intensity yielded from the straight blade is bounded in the range of (1-1.2).

Slotted Blade

The slotted blade was tested with the same methodology as the Straight blade, and here we present the experimental findings, under a resistive loading equal to 0.5Ω . The power presented here will be described as percentage difference over the straight blade, since all the blades are alterations from those above.

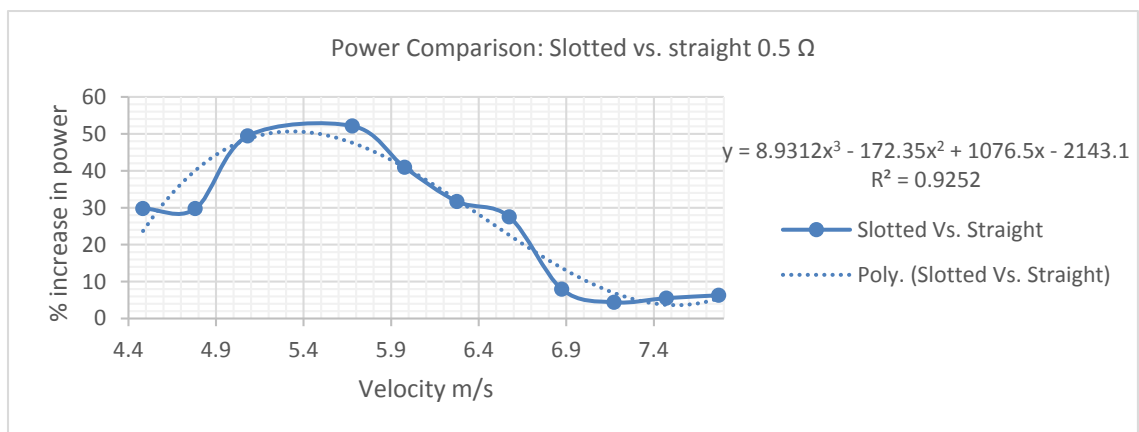


Figure 47: Slotted blade Power, Depicted as percentage of Straight Blade

The slotted blade cut in speed was lower than the straight blade. It was observed that the slotted cut in speed was $\approx 7\%$ less than the straight, where it was able to generate power at ≈ 4.2 m/s compared to ≈ 4.5 m/s under the same conditions. From figure 48, it can be seen that the slotted blade locally generates about 50% more power compared to the straight blade, and 26.1% on average under the same conditions. The reason for the increase is due to the slots capturing more wind for smaller velocities. The advantage of the leading edge slots is apparent for low wind velocities. This advantage seems to show less effectiveness moving to higher wind speeds, where the drag influence increases, causing the extracted power to slowly match the power extracted from the straight blade. The slotted blade offers

high utility to locations of low wind velocity, since it proved to be more effective than the traditional blade. As mentioned in Chapter II, the slots offers additional lift forces, though it increases the minimal drag, hence the power curve marches slowly to match the power from the straight blade.

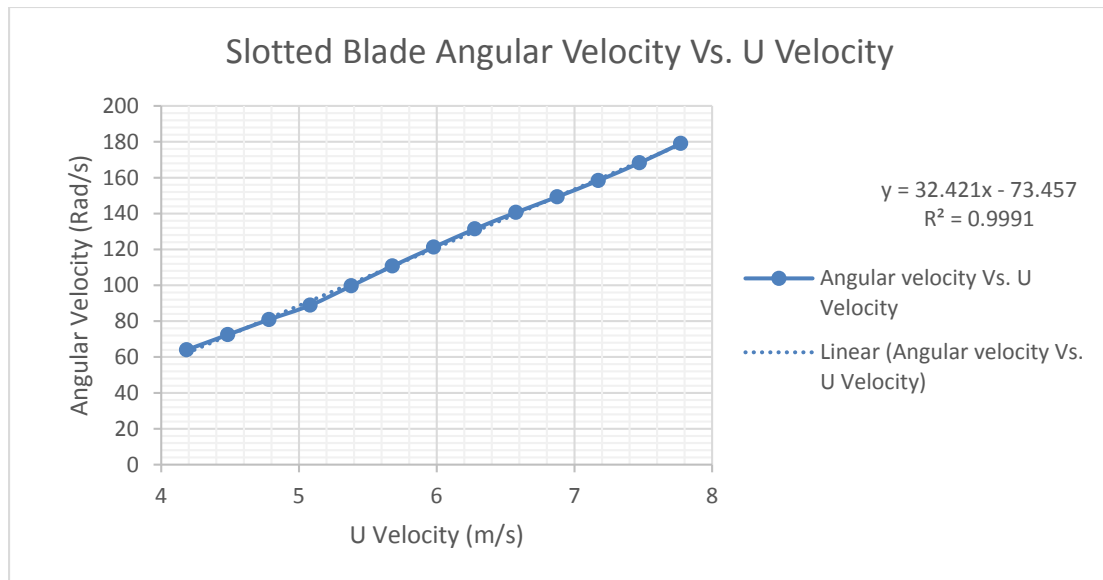


Figure 48: Slotted blade Angular velocity Vs. U velocity

As observed from figure 49, the angular velocity of the slotted blade shows a highly linear behavior. Compared to the straight blade, the statistical variance value is higher, where the straight blade yielded 0.98, while the slotted gave 0.99. This finding dictates that the slotted blade angular velocity can be predicted with better precision, which positively impact the design of the speed controllers, and power output prediction systems.

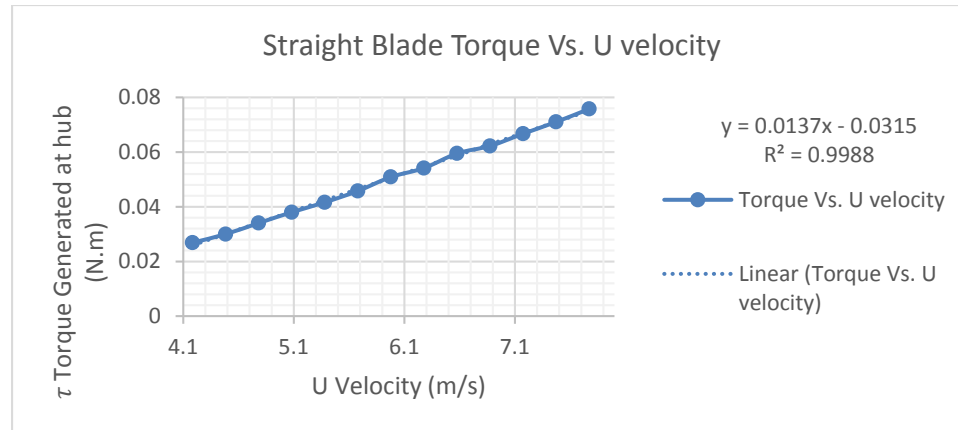


Figure 49: Slotted blade calculated torque.

The torque generated by the slotted blade is presented in figure 50 where it can be seen that the torque generated is more stable throughout the experiment. Another observation that can be inferred is that the slotted blade generated on average, 17.07% more torque as oppose to the straight blade, testing under the same conditions.

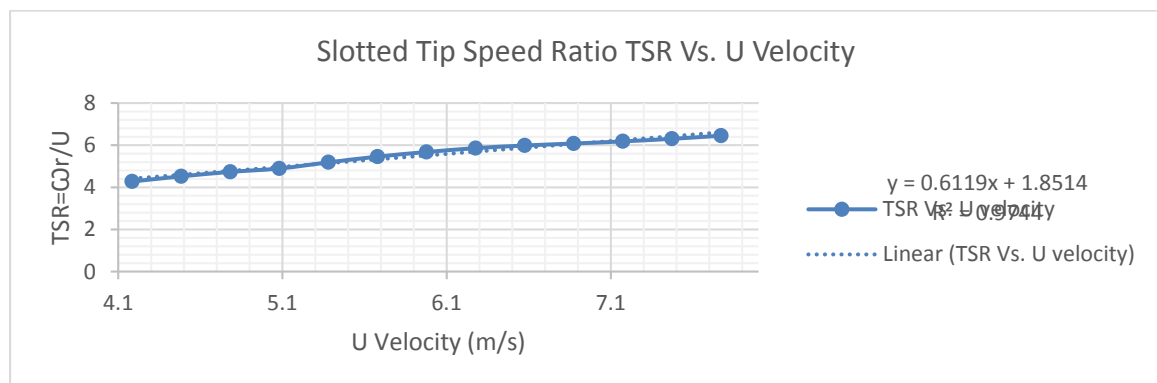
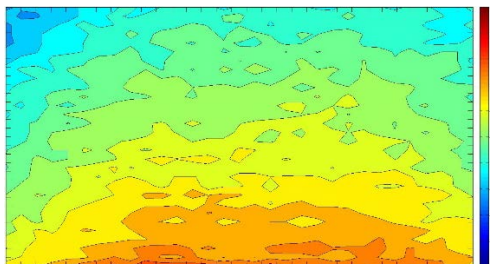
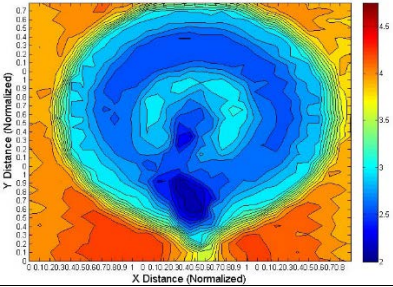
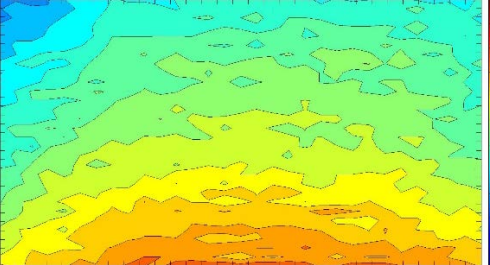
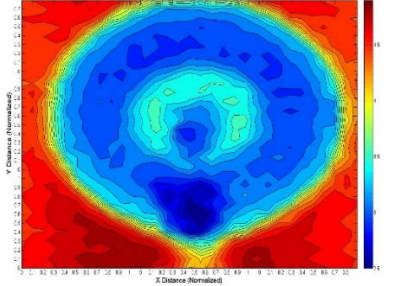
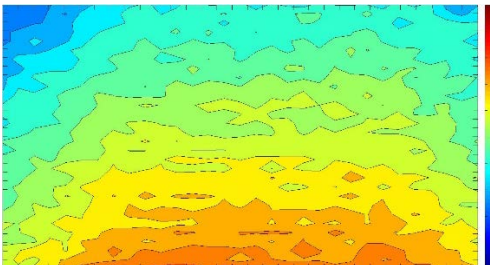
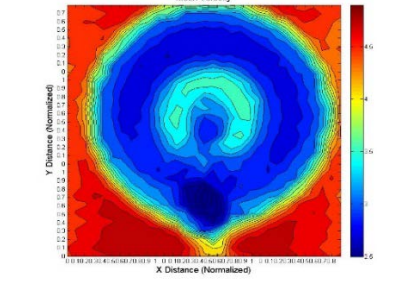
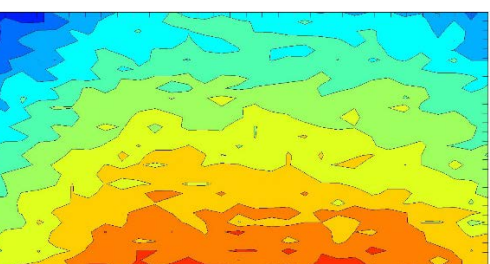
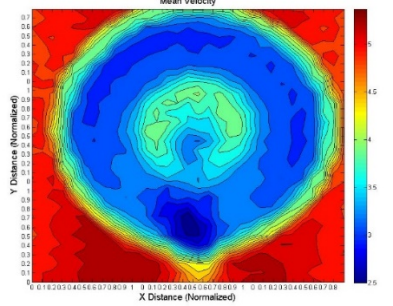
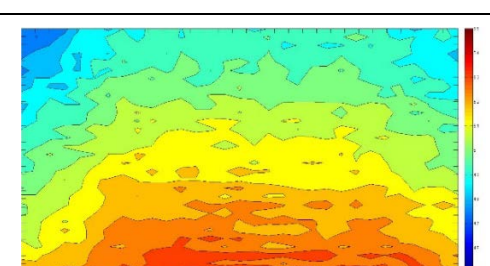
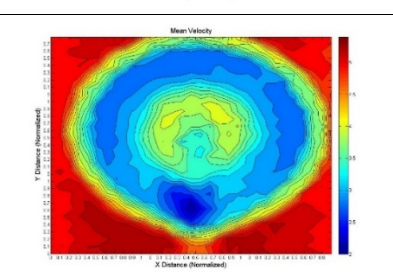


Figure 50: Slotted blade TSR values

The tip speed ratio of the slotted blade, as depicted in figure 51, was found very comparable to the values acquired from the straight blade. This is an indication that for the same TSR, the slotted design is exerting more power, converting energy captured from wind more efficiently to torque, which later translated to power. Furthermore, the TSR was found to be in the range (4.2-6.4), which is lower comparing to the straight blade.

Table 15: Flow Field Mapping for Slotted blade at different velocities, taken at inlet section of wind tunnel and 12in behind wind turbine

Velocity	Before Wind Turbine	After Wind turbine
4.78 m/s		
5.08 m/s		
5.38 m/s		
5.67 m/s		
5.97 m/s		

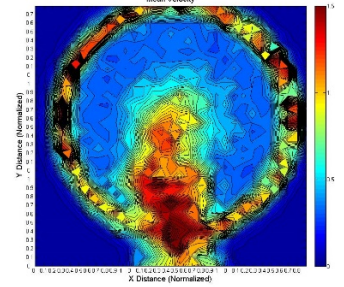
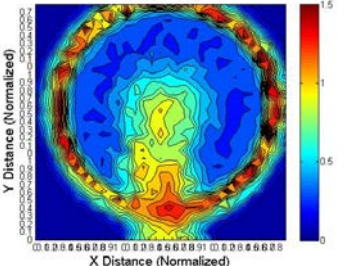
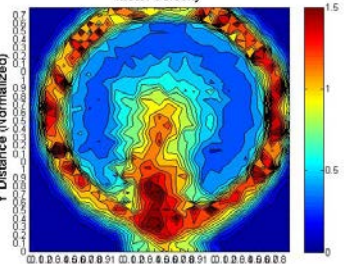
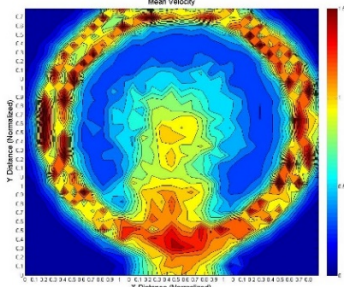
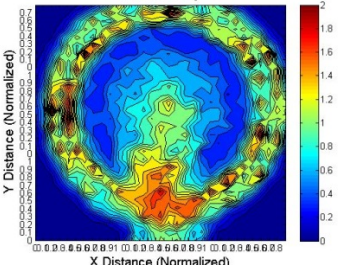
The performance coefficient was analyzed from table 15, for the slotted blade, utilizing different wind velocities, and the findings was tabulated in table 16.

Table 16: Slotted Blade Cp Values

	Slotted blade Coefficient of performance					Average C_p Value
Velocity (m/s)	4.782	5.081	5.380	5.679	5.978	
C_p	0.390	0.310	0.445	0.366	0.549	0.412

The slotted blade yielded higher C_p values compared to the traditional straight blade. The average C_p value was found to be 41.2% in the case of slotted blade and 35.9% in the case of straight blade. This increase in power coefficient would directly translate to more power generation, due to the fact that the C_p is used as a design parameter for any wind turbine project.

Table 17: Slotted Blade Turbulence intensity

Velocity	Turbulence intensity
4.78 m/s	 <p>A contour plot titled 'Mean Velocity' showing velocity distribution in a circular domain. The x and y axes are labeled 'X Distance (Normalized)' and 'Y Distance (Normalized)' respectively, both ranging from 0 to 1. A color scale on the right indicates velocity values from 0 (blue) to 1.5 (red). The plot shows a central region of high velocity (red/yellow) surrounded by lower velocity regions (blue/cyan).</p>
5.08 m/s	 <p>A contour plot titled 'Mean Velocity' showing velocity distribution in a circular domain. The x and y axes are labeled 'X Distance (Normalized)' and 'Y Distance (Normalized)' respectively, both ranging from 0 to 1. A color scale on the right indicates velocity values from 0 (blue) to 1.5 (red). The plot shows a central region of high velocity (red/yellow) surrounded by lower velocity regions (blue/cyan).</p>
5.38 m/s	 <p>A contour plot titled 'Mean Velocity' showing velocity distribution in a circular domain. The x and y axes are labeled 'X Distance (Normalized)' and 'Y Distance (Normalized)' respectively, both ranging from 0 to 1. A color scale on the right indicates velocity values from 0 (blue) to 1.5 (red). The plot shows a central region of high velocity (red/yellow) surrounded by lower velocity regions (blue/cyan).</p>
5.67 m/s	 <p>A contour plot titled 'Mean Velocity' showing velocity distribution in a circular domain. The x and y axes are labeled 'X Distance (Normalized)' and 'Y Distance (Normalized)' respectively, both ranging from 0 to 1. A color scale on the right indicates velocity values from 0 (blue) to 1.5 (red). The plot shows a central region of high velocity (red/yellow) surrounded by lower velocity regions (blue/cyan).</p>
5.97 m/s	 <p>A contour plot titled 'Mean Velocity' showing velocity distribution in a circular domain. The x and y axes are labeled 'X Distance (Normalized)' and 'Y Distance (Normalized)' respectively, both ranging from 0 to 1. A color scale on the right indicates velocity values from 0 (blue) to 2 (red). The plot shows a central region of high velocity (red/yellow) surrounded by lower velocity regions (blue/cyan).</p>

The turbulence intensity for the slotted blade is found in table 17, for selected velocities. It can be noticed that the slotted blade resulted in high turbulence intensity, compared to the straight blade, where it was found between (1-1.5) for the selected range of velocities. This increase in turbulence intensity can be translated to more noise generation as the flow leaves the blade body.

Tubercle Blade

The tubercle blade followed the testing methodology constructed for this study, and here we present the power findings as compared to the straight blade.

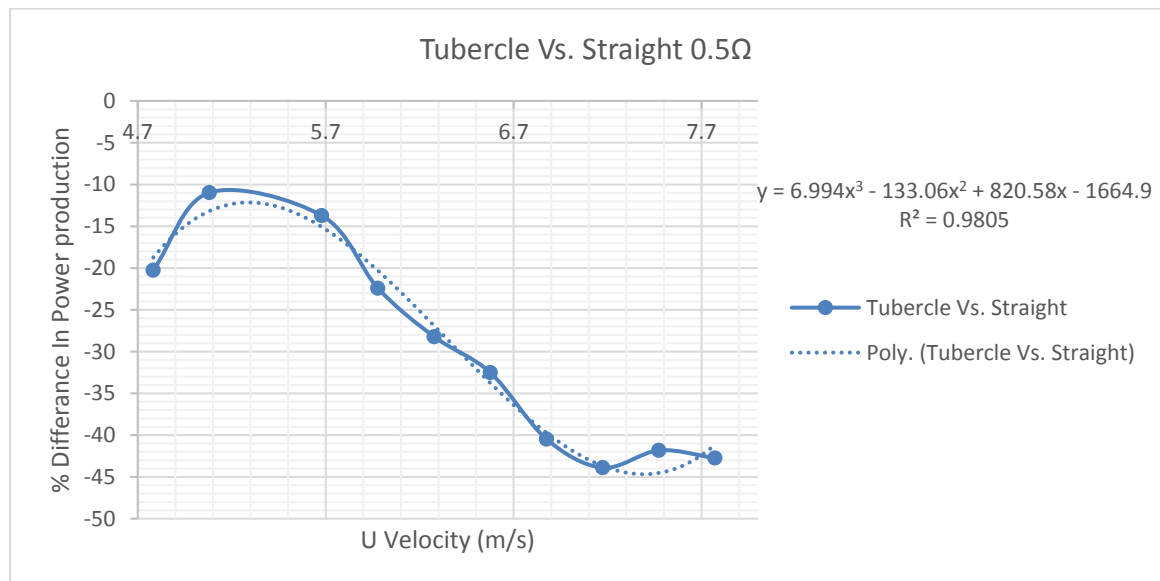


Figure 51: Tubercle blade power as compared to the straight blade

Figure 53 shows the power output from the tubercle blade in comparison to the straight blade. It can be noticed that the tubercle blade performed less efficiently than the straight blade, with an average decrease in power production equal to 29.16%. One reason that might be behind this drastic drop in power might be that the surface area of the tubercle blade suffered from a 14% decrease compared to the straight. The reduction in area was an anomaly ascended from the design stage, carried out to the testing, where the impact

became evident. Another observation that was noted for the tubercle blade that the cut in speed was high. Now, the straight blade started producing power at ≈ 4.5 m/s. On the other hand, the tubercle blade started at ≈ 4.7 m/s. The tubercle blade had an advantage over the straight and the slotted blade, the power production seemed to be continuing over a bigger range of velocities, while other designs seemed to be decreasing power production, the tubercle blade was still increasing.

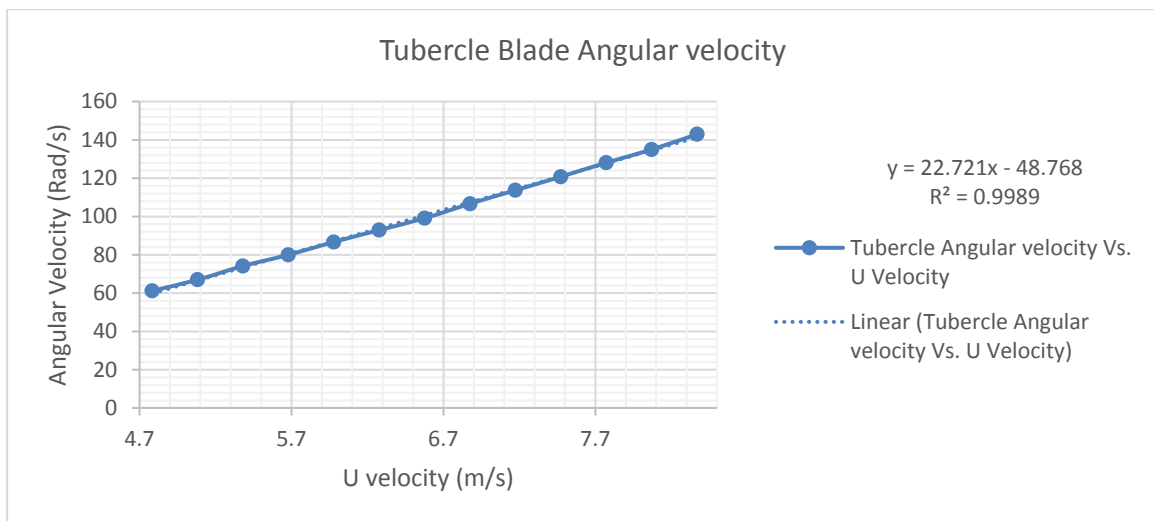


Figure 52: Tubercle blade Angular velocity Vs. U velocity

It can be seen from figure 54 that the tubercle blade showed a great transition in angular velocity in response to the varying the inlet velocity. This would enhance the prediction of angular velocity, where it can be achieved with high precision. This is inferred from the statistical variance value, where it is very close to unity, giving superior control characteristics for such blade. This highly desired characteristic is due to the fact that the tubercles on the blade breaks the vortices created while the flow separates from the blade body, breaking them into smaller vertices, increasing the response time to changing velocity.

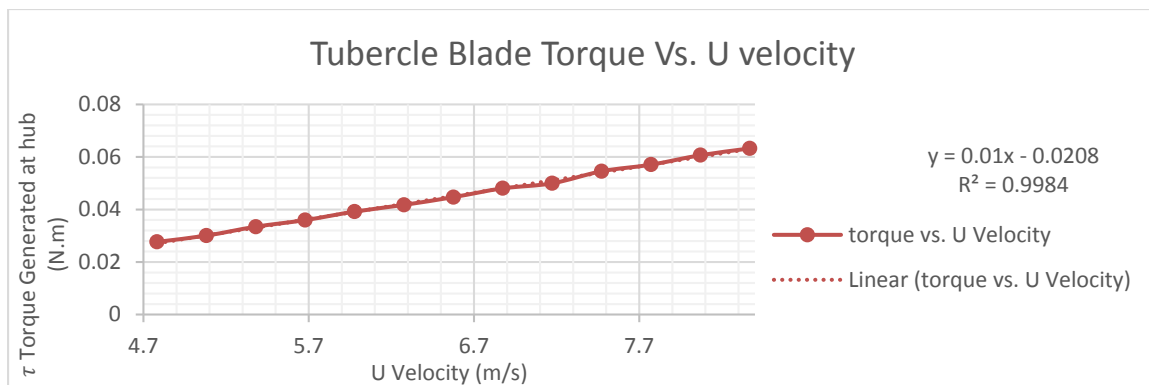


Figure 53: Tubercle Blade Torque vs. U Velocity

Figure 55 shows the calculated torque for the tubercle blade. The tubercle blade was able to generate constant power, with excellent response to wind velocity variations. Additionally, the blade generated 8.82% less torque compared to the traditional straight blade.

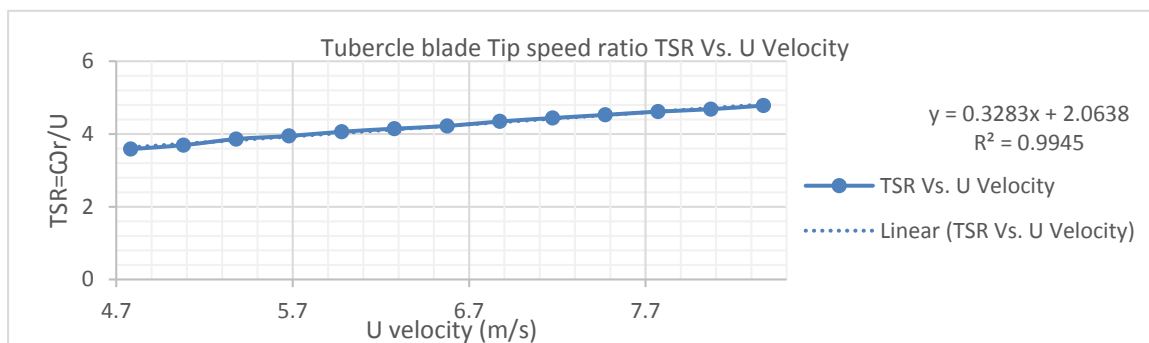
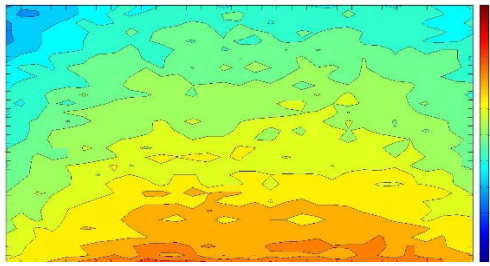
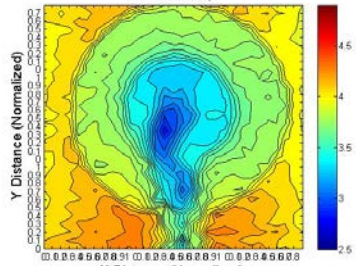
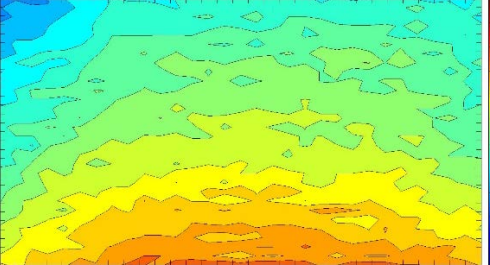
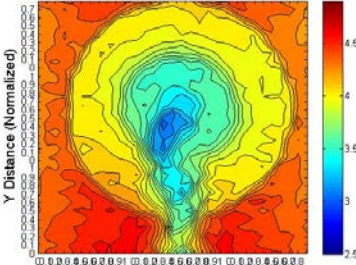
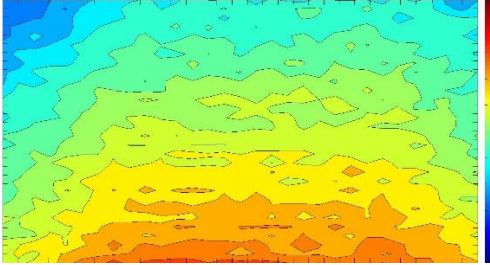
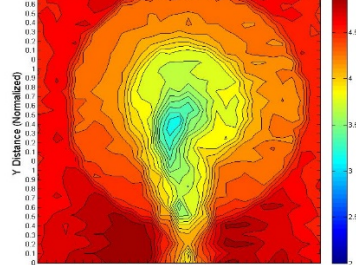
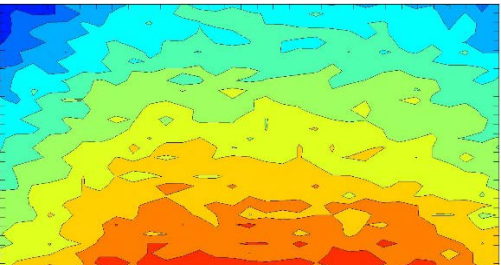
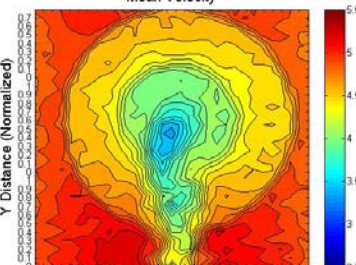
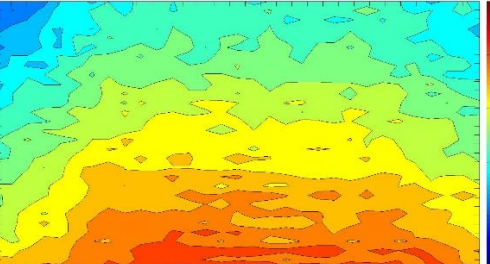
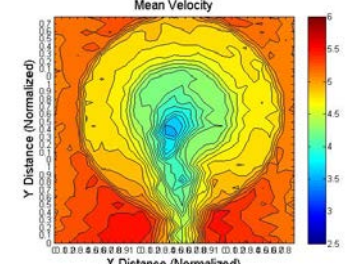


Figure 54: Tubercle Tip Speed Ratio

The range of TSR for the tubercle blade was found to be in the range of (3.5-4.7). Compared to the straight blade, it is a low value, though still acting within the optimal range.

Table 18: Flow Field Mapping for Tubercle blade at different velocities, taken at inlet section of wind tunnel and 12in behind wind turbine

Velocity	Before Wind Turbine	After Wind turbine
4.78 m/s		
5.08 m/s		
5.38 m/s		
5.67 m/s		
5.97 m/s		

The figures presented in Table 18 was analyzed for the coefficient of performance, and the values yielded were tabulated in Table 19.

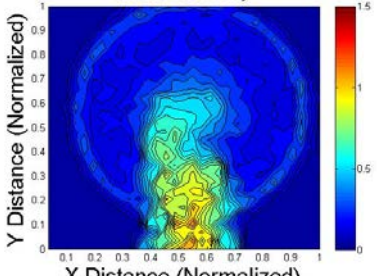
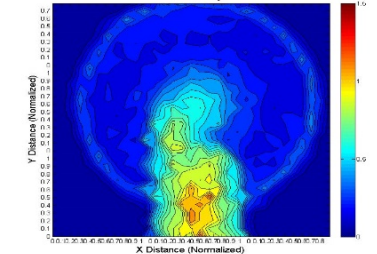
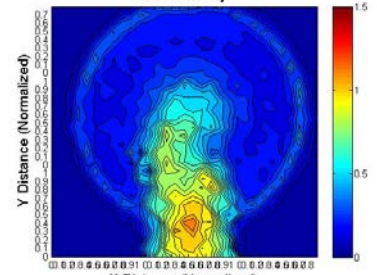
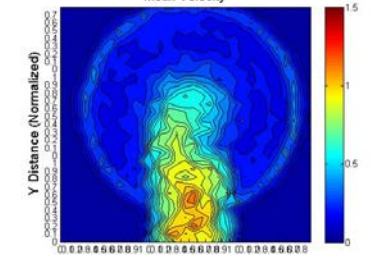
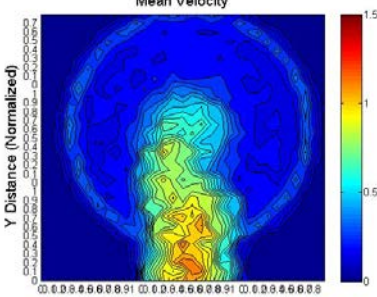
Table 19: Tubercle Blade Cp Values

	Tubercle blade Coefficient of performance					Average Cp Value
Velocity (m/s)	4.782	5.081	5.380	5.679	5.978	
Cp	0.132	0.173	0.160	0.120	0.123	0.142

The tubercle blade yielded low values of C_p , which was adhering to the findings of low torque generation.

The tubercle blade turbulence intensity contours can be found in figure 57, for selected range of velocities. It can be noticed that the tubercle blade had very low turbulence intensity, yielding values in the range (0-0.5), compared to both the slotted blade and the straight blade. This finding dictates that the tubercle blade is superior in suppressing the acoustics developed due to the blade body–fluid flow interactions, which is referred to as the tip flow noise. The results here seems to adhere to the hypotheses that the tubercles on the suction side of the blade would further break the vortex generated due to separation. This finding constitutes the creation of smaller vortices that has less turbulent kinetic energy (TKE), dissipating less energy while cutting through air.

Table 20: Tubercle Blade Turbulence intensity

Velocity	Turbulence intensity
4.78 m/s	 <p>Mean Velocity</p> <p>Y Distance (Normalized)</p> <p>X Distance (Normalized)</p>
5.08 m/s	 <p>Mean Velocity</p> <p>Y Distance (Normalized)</p> <p>X Distance (Normalized)</p>
5.38 m/s	 <p>Mean Velocity</p> <p>Y Distance (Normalized)</p> <p>X Distance (Normalized)</p>
5.67 m/s	 <p>Mean Velocity</p> <p>Y Distance (Normalized)</p> <p>X Distance (Normalized)</p>
5.97 m/s	 <p>Mean Velocity</p> <p>Y Distance (Normalized)</p> <p>X Distance (Normalized)</p>

CFD results

For the CFD study, three distinct velocities were used, 5.3, 6.2 and 7.7 m/s. These velocities were applied to all the four blade designs, additionally, these velocities were accompanied by a rotational velocity given to the fluid domain, to simulate the blade rotation. This process is called, flow induced motion, which is the driver behind the torque generation. The rotational velocities used were tabulated in table 21.

Table 21: flow parameters used in CFD study

CFD Investigation cases			
	Case#1	Case#2	Case#3
Inlet Velocity	5.3 m/s	6.2 m/s	7.7 m/s
Angular Velocity	80 Rad/s	105 Rad/s	150 Rad/s

Straight blade

The torque computed by the CFD study for the straight blade is presented in figure 58.

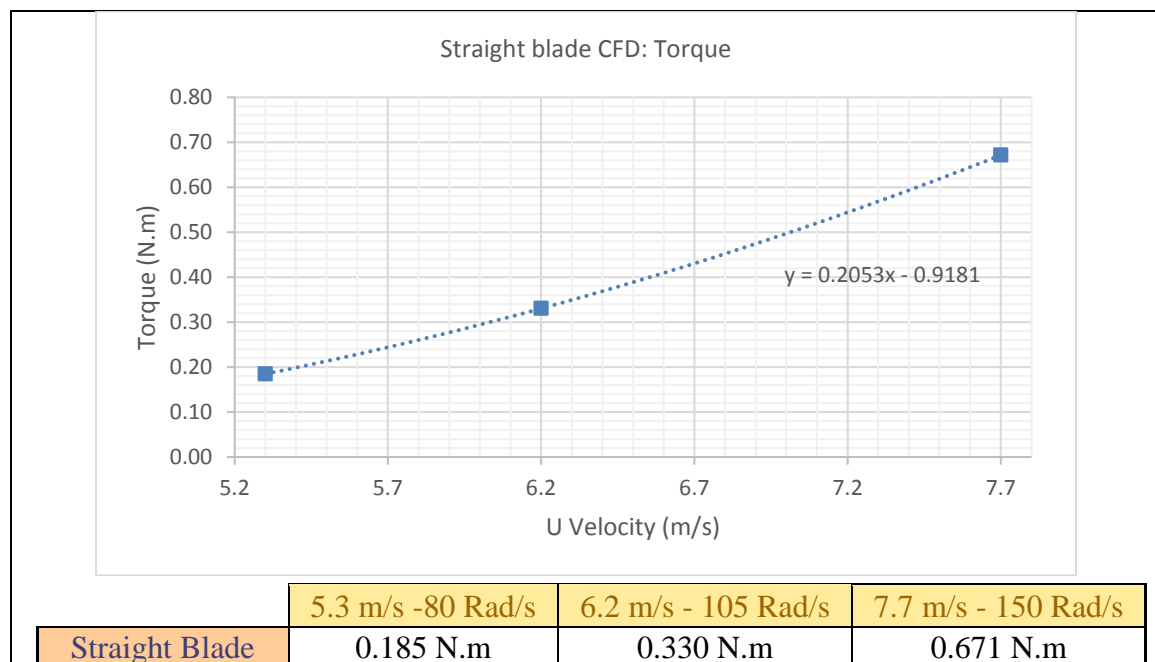


Figure 55: Straight Blade CFD results for torque

Here it can be seen from figure 58 that the torque is linearly increasing with increasing velocity.

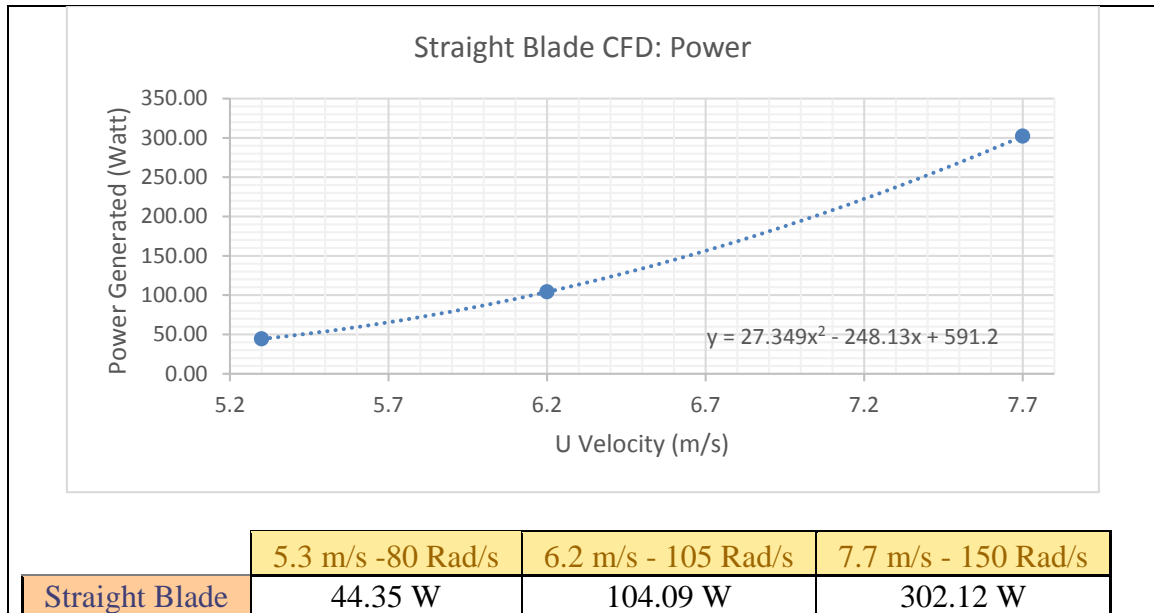


Figure 56: Straight blade CFD Result For torque

Figure 59 shows the power, resolved through CFD.

Slotted Blade

The CFD results for the slotted blade is depicted in this section, where figure 60 shows the torque generated by the slotted blade.

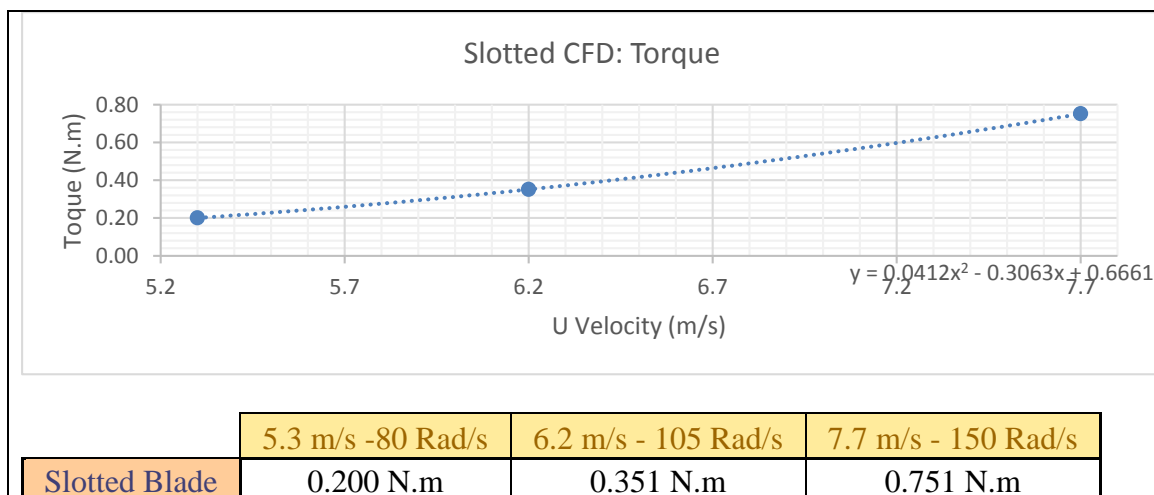


Figure 57: Slotted Blade CFD Results for Torque.

The Power findings Presented here are referenced to the straight blade as a baseline, and all values will be a percentage of the values discussed in the straight blade CFD section.

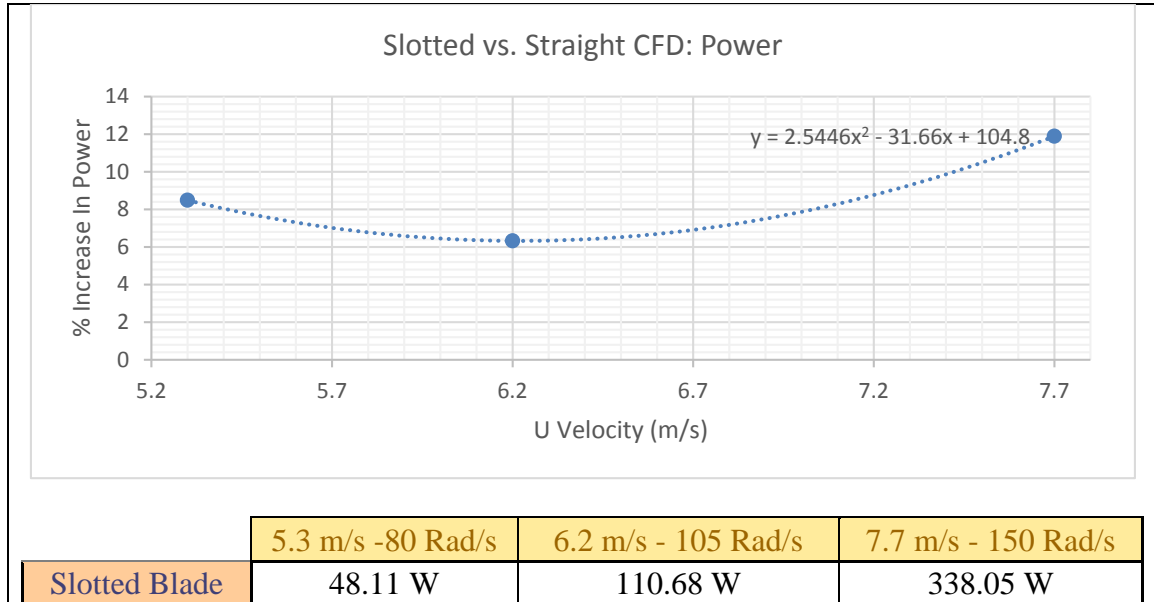


Figure 58: Slotted Blade CFD Results for Power Compared to straight blade

The slotted blade simulations and the experimental findings both verify that the slotted blade is generating more energy for the same conditions. It can be seen in figure 61 that the slotted blade achieved more power compared to the straight, on average the increase was recorded as 8.9%.

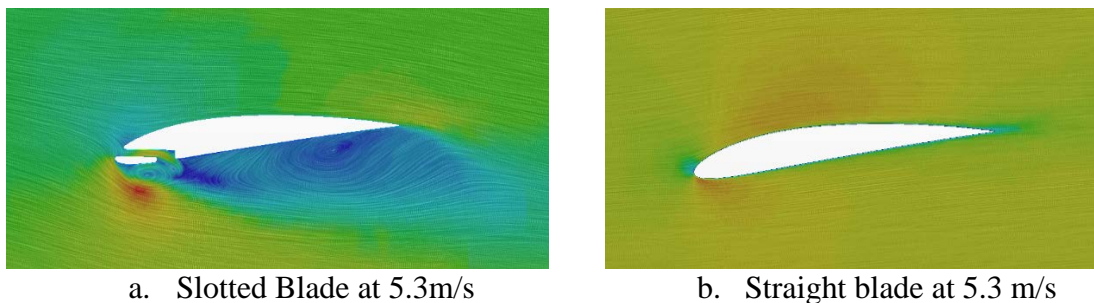


Figure 59: Slotted Blade Velocity Line integral Convolution

It can be seen from figure 62 that the stream exiting the slot impinges onto the incoming flow, further separating the flow away from the blade lower body, hence creating a larger region of high pressure. This addition in the high pressure region would increase the

differential pressure along the two sides, (suction and pressure), when compared to the plane straight blade.

Tubercle Blade

The tubercle blade computed simulation results are presented in this section. Figure 63 shows the torque resolved through CFD for the tubercle blade, where it is increasing with the increasing incoming velocity.

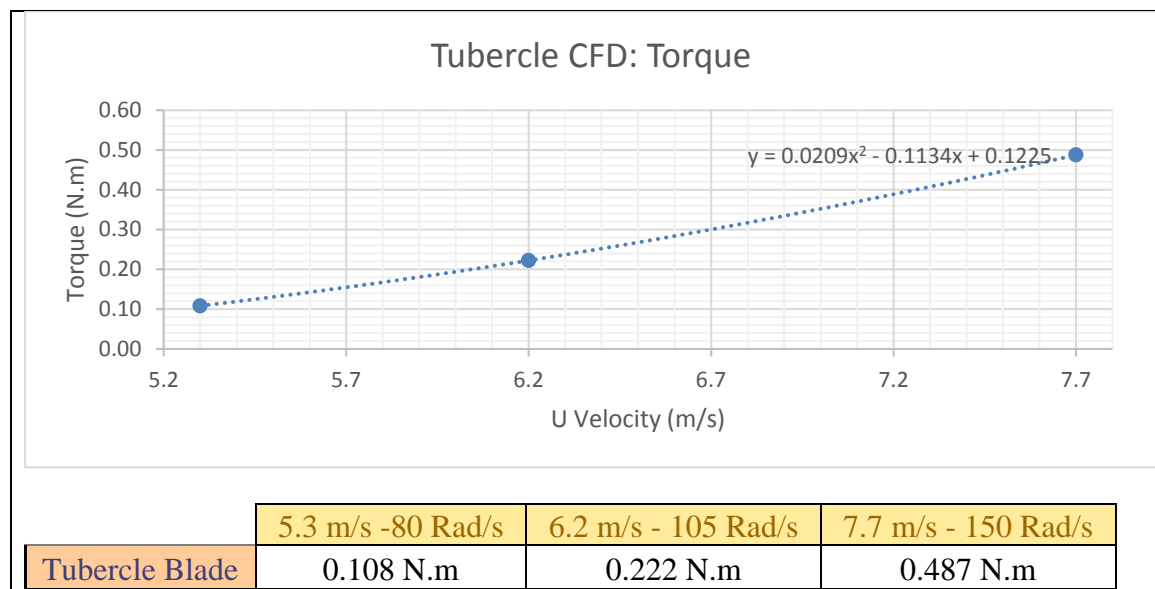


Figure 60: Tubercle Blade CFD results for torque

The tubercle simulations concurred the results of the experiment, where it was found that the torque generated computationally is $\approx 33.8\%$ less than the straight blade on average.

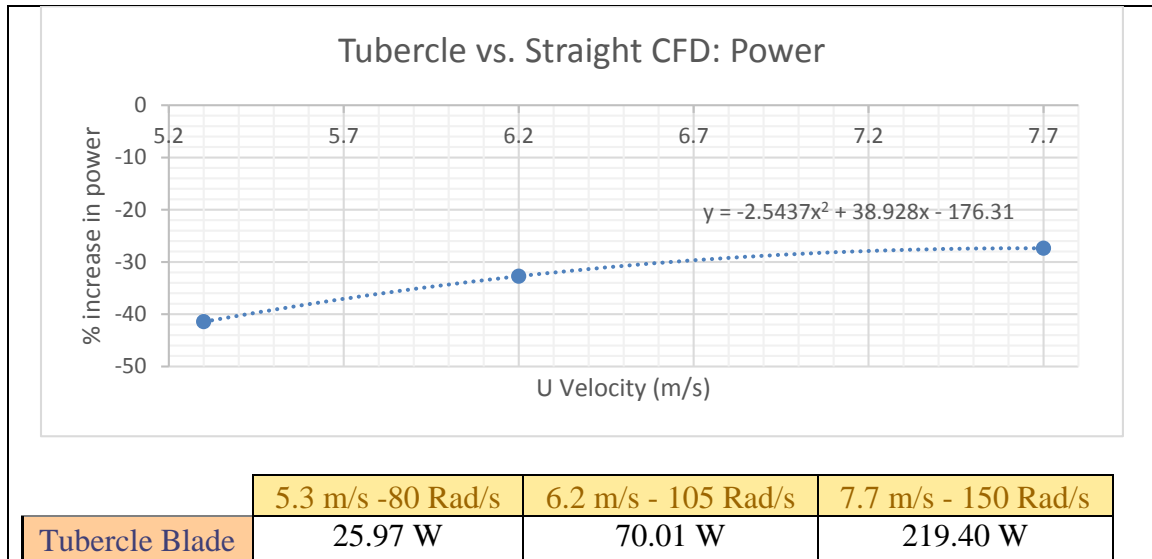
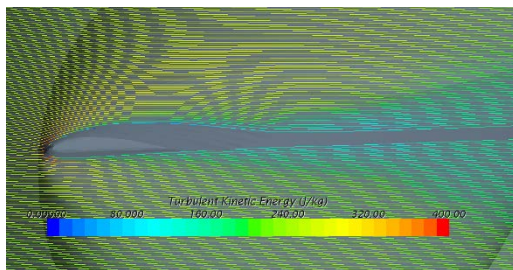
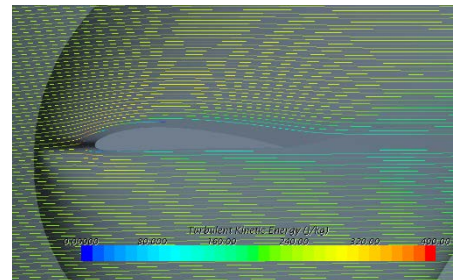


Figure 61: Tubercle Blade CFD Results for Power Compared to straight blade

As an effect of low torque, the power generated by the tubercle blade is of lower values comparing to the traditional straight blade.



a. Stream lines displaying TKE on Tubercle blade body at 6.2 m/s



b. Stream lines displaying TKE on Straight blade body at 6.2 m/s

Figure 62: Stream line plot colored by Turbulence Kinetic Energy for tubercle and straight blade.

Figure 65 shows the turbulence kinetic energy for both straight blade and tubercle blade. It can be seen in figure 65 a. that the tubercle has lower values of TKE as the flow leaves the body, compared to the straight blade. This is an indication that the tubercles truly minimize the trailing edge vortices by suppressing their size, which promotes higher characteristics.

Winglet Blade

In this section, we present the CFD findings for the Winglet blade.

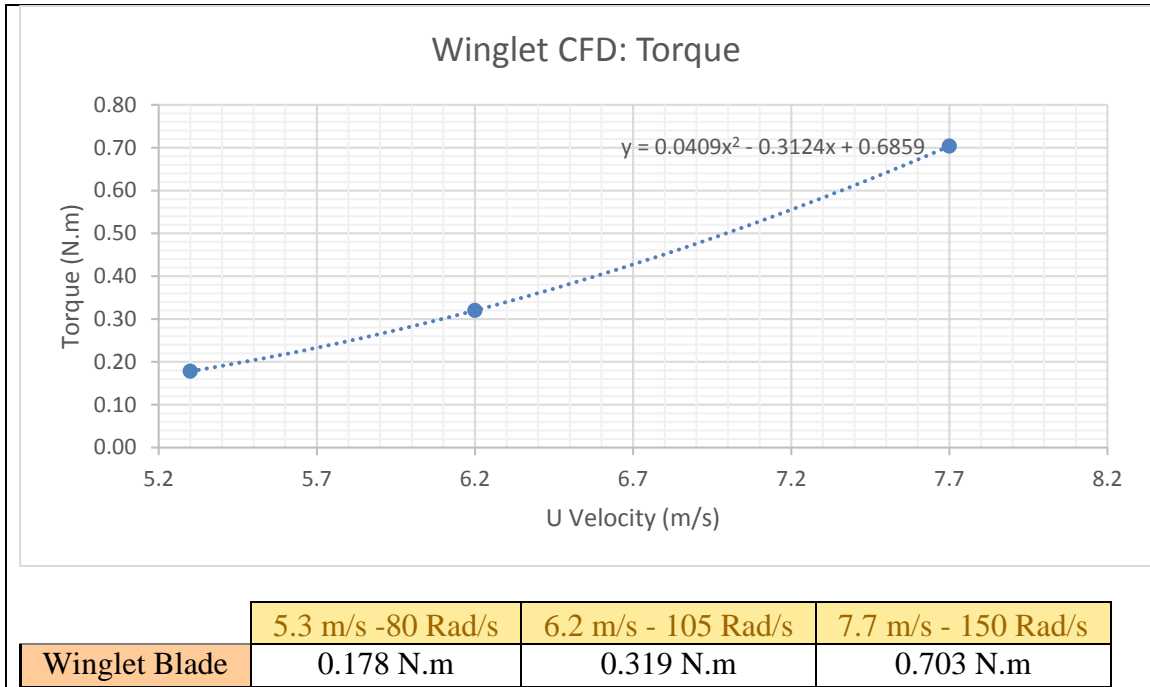


Figure 63: Winglet Blade CFD results for torque

The torque generated by the winglet blade can be seen in figure 66.

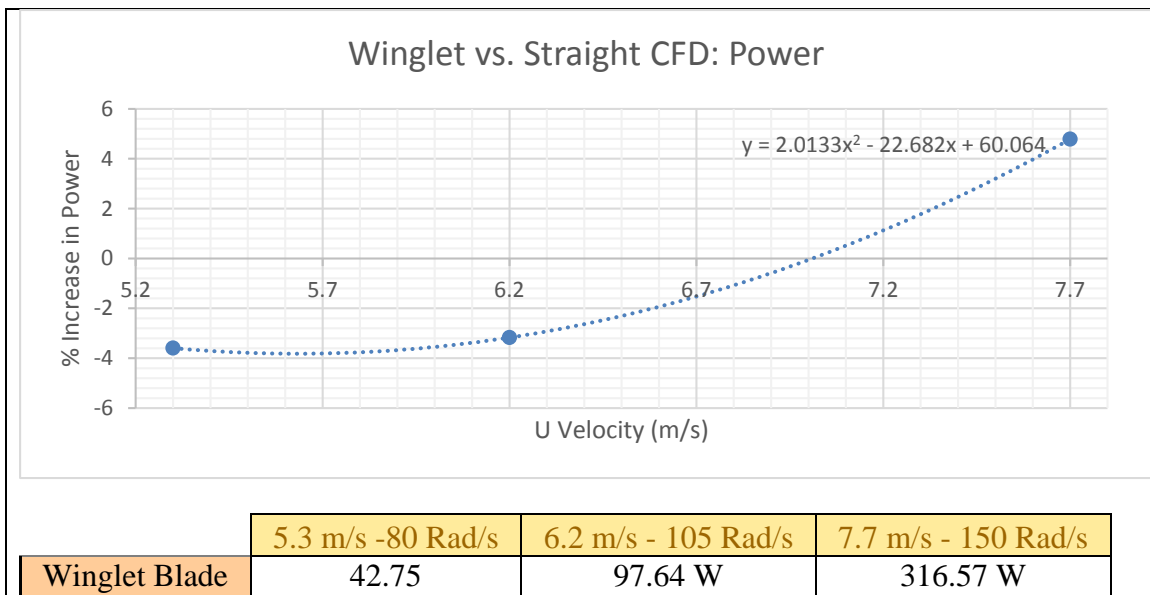


Figure 64: Winglet Blade CFD Results for Power Compared to straight blade

From figure 67, it can be seen that the findings for the winglet blade was meeting the expectations. Since the first two points show a decrease in torque equal to $\approx 3.2\%$ ending up with an increase equal to $\approx 5\%$. This is expected since the winglet blade has more mass pointing out of the body, increasing the inertial forces needed move the blade into the rotation direction, hence the decrease. In addition, when the winglet blade starts moving and starts cutting through the air at higher velocities, the inertial forces come as an advantage, increasing the centripetal forces, and propagating at higher efficiency within the fluid region.

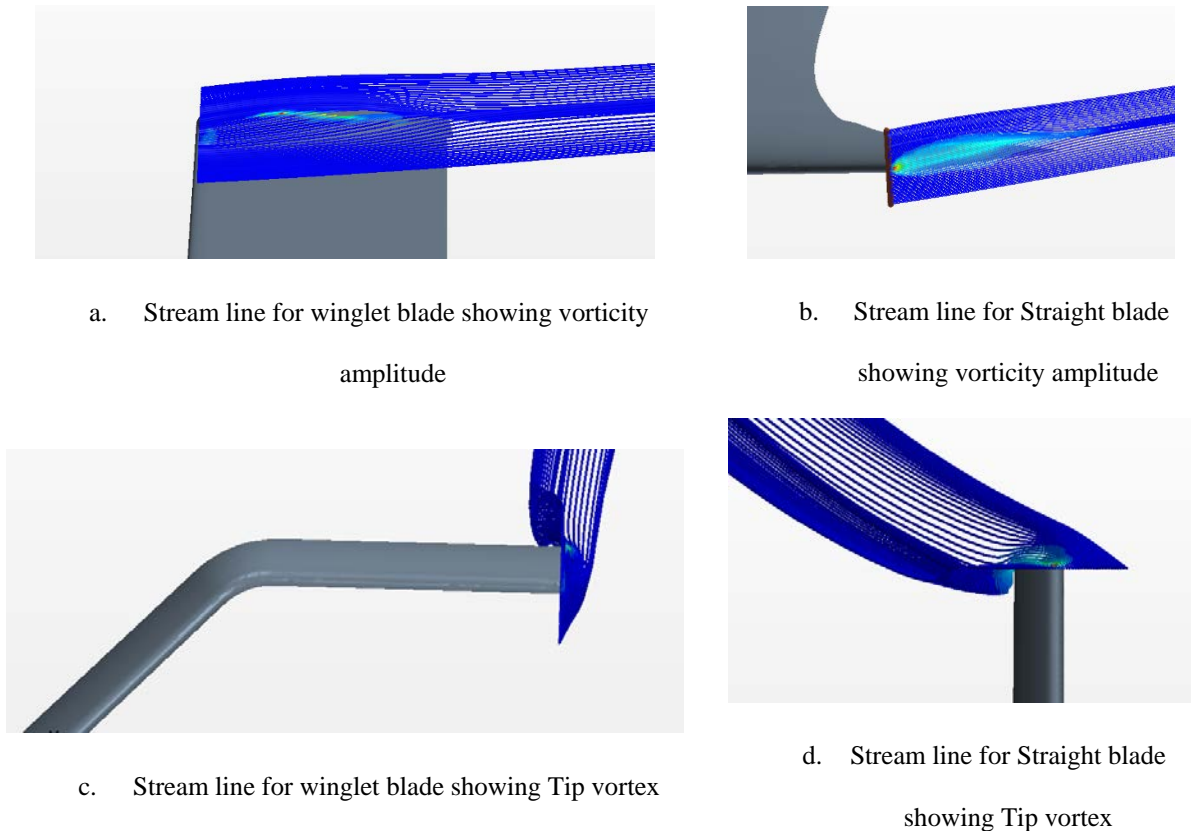


Figure 65: Tip vortex for straight and winglet blade

The winglet blade was aimed to solve one problem that negatively impact the efficiency of the wind turbine blade, which is the problem of tip vortex generation. This problem has been tackled in airplanes with the addition of winglets, and analogously in wind turbines.

As seen in figure 68 .a, the winglet blade is of lower vorticity magnitude compared to the straight blade, depicted in figure 68 .b, where it is apparent that the straight blade has a greater region of high vorticity. Figure 68 .c shows the size of the tip vortex generated by the winglet blade, where it is of less size and less intensity comparing to figure 68 d.

Chapter VII. Discussion of Results

In this section the findings of both experiment and computational studies are discussed in details.

Experimental results

The experimental results are summarized in table 22.

Table 22: summary of experimental findings for slotted, tubercle and straight blade.

	Mass (gram)	Cut in speed (m/s)	Power compared to straight Blade	Torque	TSR	C _p	Turbulence Intensity.
Straight	57.44	4.5	NA	NA	3.8-6.7	0.359	1-1.2
slotted	57.62	4.2	26.10%	17.07%	4.2-6.4	0.412	1-1.5
tubercle	56.45	4.7	-29.16%	-8.82%	3.5-4.7	0.142	0.0-0.5

The slotted blade was found experimentally to be generating more power than the straight blade, with an average increase in power production equal to 26.1%. This increase in power is due to the fact that the slots on the leading edge captures more wind, resulting in an increase in the resultant lift, increasing the torque generation, resulting in more power. It was also noted that the slots on the leading edge increases the form drag, decreasing the power output with higher wind velocities, but matching the power output from the traditional straight blade. Another finding was that the slotted blade started generating energy at lower values of cut in speed, compared to the straight blade, it started at $\approx 7\%$ less wind speed. The torque generated by the slotted blade was higher than that by the straight blade, which had an average increase equal to 17.07%. The tip speed ratio measured for the slotted blade was very comparable to the straight blade, yet produced more power, which is a sign that the addition of slots exerts more torque. The Coefficient of performance was found to be 0.412, which is a remarkable finding, since this new design competes with the best commercial wind turbines available in the market.

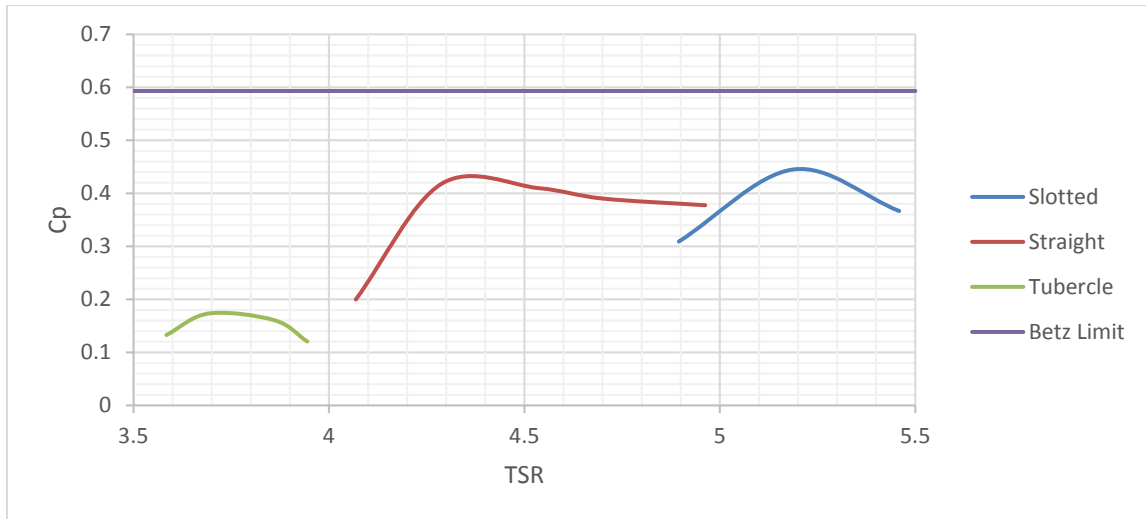


Figure 66: Coefficient of performance Vs. TSR for slotted, tubercle and straight blade.

The tip speed ratio is a nondimensional number, which is a good factor to be used to correlate the performance of the blades independent of the size and incoming velocity.

Figure 69 depicts the collected Cp values as oppose to the TSR to situate the blades among various commercially available wind turbines.

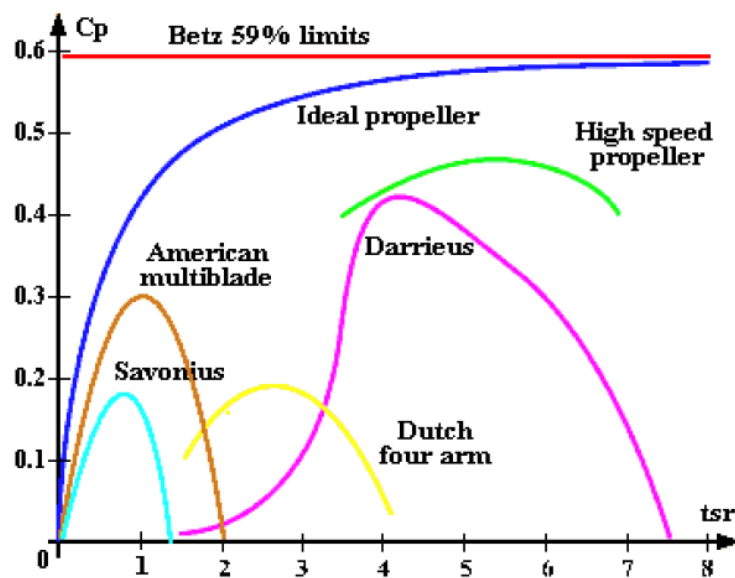


Figure 67: Typical Wind turbine Cp Values

(Source: <http://www.windturbine-analysis.netfirms.com>)

Figure 70 shows the typical values of C_p collected from common commercially available wind turbines. It can be seen that the slotted blade showed competitive performance compared to the commercially available wind turbines. The tubercle blade was found to be 29.16% less effective than the straight blade, one explanation that might be the reason of such decrease might be the active contact area being less by 14% than the traditional straight blade. This was a design flaw, carried out to the testing stage, and found after investigating the decrease in power output. The tubercle blade generates less torque than the straight blade, by a reduction equal to 8.82%. The average coefficient of performance was found experimentally to be equal to 0.142, which is low in comparison to the other designs. A significant finding for the tubercle blade was that the turbulence intensity was found very minimal, compared to other designs. This finding is an indication that this blade has great potential for development, since such behavior would positively impact the wind turbine in a wind turbine farm setting, resulting in minimal turbulence, not affecting other turbines in surrounding areas.

CFD Results

Table 23 summarizes the findings for CFD of the torque for all four blade designs.

Table 23: Torque CFD findings for the blades under investigation

	Torque generated at Hub (N.m)		
	5.3 m/s -80 Rad/s	6.2 m/s - 105 Rad/s	7.7 m/s - 150 Rad/s
Slotted Blade	0.200	0.351	0.751
Straight Blade	0.184	0.330	0.671
Winglet Blade	0.178	0.319	0.703
Tubercle Blade	0.108	0.222	0.487

Table 24 summarizes the findings for CFD of the power for all four blade designs.

Table 24: Power CFD findings for the blades under investigation

	Power Generated (Watt)		
	5.3 m/s -80 Rad/s	6.2 m/s - 105 Rad/s	7.7 m/s - 150 Rad/s
Slotted Blade	48.11	110.68	338.05
Straight Blade	44.35	104.09	302.12
Winglet Blade	37.95	97.64	316.57
Tubercle Blade	25.97	70.01	219.40

The slotted blade was found to be producing 8.9% more power numerically. Additionally, the tubercle blade was found to be less effective than the straight, slotted as well as the winglet blade with an average decrease $\approx 33\%$. Furthermore, the winglet blade was found to be behaving very similarly to the straight blade, with a disadvantage at low velocities, becoming an advantage moving to higher wind velocities. this is an implication of the fact that there are differences in the mass distribution along the blade body, compared to the straight.

CFD Validation with Experiment and Error Discussion

The experimental work was designed to produce low power since the objective of this study is to have a baseline comparison among the designs rather than improving the efficiency of the power extraction. This low power generation was made by design, since dealing with the high amount of energy comes with high risks, and is not the intentions of the author. This low power comes with a penalty of the experiment being of lower resolution, yet accurate in findings, since the experiments took place in three trials with a high agreement in results.

The results shown in figure 71 depicts the experimental work, infused with the CFD for the slotted and the tubercle blade, comparing them to the baseline straight blade.

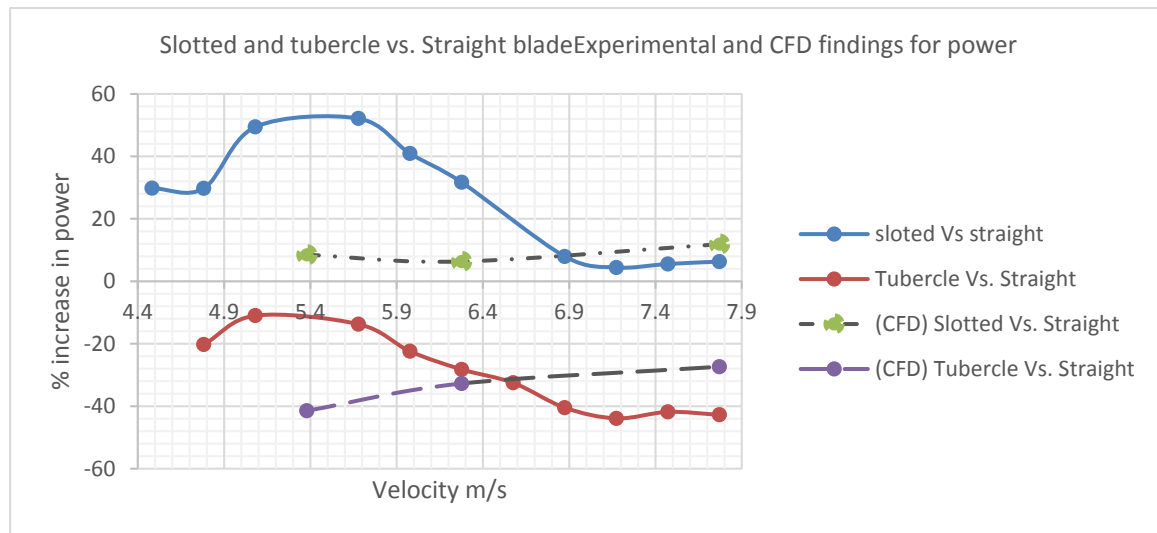


Figure 68: CFD and experimental power findings for slotted and tubercle blade compared to the straight blade

It can be inferred from figure 71 that the experimental findings show much higher increase in power production, which has been anticipated. The experiment had low efficiency compared to the numerical work that was based on highly constructed and well-made conditions. One major condition might be that the torque calculated by the CFD is

correspondent to the highest torque that a wind turbine could achieve, and to match that condition experimentally a resistance approaching zero as a limit would produce such power. The experimental losses can be from many sources, such as the blade surface roughness, tip losses, wake effect losses, generator losses, electric losses at connections, wires and motor magnetic friction losses. The above mentioned losses would impact the power system to decrease significantly the total power generated by the wind turbine. But using the same hub, motor, tower and electric connections makes these losses dependent on the system rather than being design dependent. These losses are carried out for all the different designs. When comparing the CFD results to the experimental, we find a relation there, symbolizing the efficiency of the experiment relative to the ideal cases of CFD. Table 25 shows the relative efficiency of the experiment to the numerical findings. This was done in means of power generated, where we can see that for each velocity, corresponding to a distinct Reynolds number there is a discrete factor governing the power production.

Table 25: Efficiency of experiment compared to the CFD findings

Relative efficiency of experiment system compared to numerical findings			
Velocity	5.3 m/s	6.2 m/s	7.7 m/s
Slotted blade	20.56%	16.07%	10.03%
Straight blade	19.32%	12.97%	10.56%
Tubercle blade	22.86%	13.84%	10.30%
Average	20.92%	14.30%	10.30%
CFD Case #	Case#1	Case#2	Case#3

The factors depicted in table 25 shows that the efficiency of the experiment was changing as the Reynolds number changes for the CFD, but still bounded for the three cases by the same range. If we take 5.3 m/s as an example, it can be seen that for the slotted, the relative efficiency of the experiment is $\approx 21\%$, which was very close in the case of straight, yielding $\approx 19\%$, and $\approx 23\%$ in the case of tubercle, which is in 5% confidence level of the study.

Conclusions

Through observations, the slotted blade generated the highest power among the other blades, and had great characteristics. One of such, is the very low cut in speed, as well as constant power generation, observed by monitoring the frequency of the generated voltage, which had a great consistency throughout the testing stage. Furthermore, it was proven both experimentally and computationally that the addition of slots will improve the power generation. The straight blade was found very similar in characteristics with the winglet blade, with an advantage at lower wind velocities, because the straight blade requires less inertial forces to begin producing power. Another proven fact was that the winglet blade becomes more efficient with increasing wind velocity. The reason behind this is that the generated wing tip vortices is of smaller magnitude than the ones on the straight blade, and the blade witnesses less drag from such region. This increase in power would be the result from the decrease in energy dissipation on the wing tip. The tubercle blade was found to be less effective in capturing energy from the wind, due to the reasons mentioned in previous chapters. The tubercle blade was found to be superior in suppressing vortices created due to the separation, minimizing their magnitude compared to the ones produced by the straight blade. This would translate to a desired acoustic behavior, and might be a solution to one of the problems researchers has been trying to resolve for quite some time, which is the wind turbine noise. The minimal resultant turbulence might make this kind of blade ideal for wind farm applications, since the wake of this type of blade has slight turbulence intensity, which is an appealing characteristics for such field.

References

- [1] Gupta, A., Alsultan, A., Amano, R. S., Kumar, S. And Welsh, A. D. (2013). Design and analysis of wind turbine blades - winglet, tubercle and slotted. *Proceedings of the ASME Turbo Expo 2013*. San Antonio, USA.
- [2] "Environmental Impacts of Wind Power." *Union of Concerned Scientists*. USCUSA, 05 May 2013. Web. 17 Oct 2013. <http://www.ucsusa.org/clean_energy/our-energy-choices/renewable-energy/environmental-impacts-wind-power.html>.
- [3] "Frequently Asked Questions." *Noble Environmental Power*. NoblePower. Web. 17 Oct 2013. <<http://www.noblepower.com/faqs/wind-energy-economy.html>>
- [4] Lynn White Jr., *Medieval technology and social change*(Oxford, 1962) p. 87
- [5] "Aerodynamics of Winglets." *Boeing Aero 17*.N.p..Web. 17 Oct 2013. <http://www.boeing.com/commercial/aeromagazine/aero_17/winglet_story.html>.
- [6] Minnella, Gianluca. *Aerodynamic Shape Design Optimization of Winglets* .Diss. Florida International University, 2010. Web.<<http://www.eng.fiu.edu/mme/robotics/EML4905SeniorDesignProject/SampleSeniorDesignProjects/2010Fall/AerodynamicShapeDesign-FinalReport-Fall2010.pdf>>.
- [7] Fish, Frank. *The Tubercles on Humpback Whales' Flippers: Application of Bio-Inspired Technology*. Diss. West Chester University, 2011. Web.<http://darwin.wcupa.edu/~biology/fish/pubs/pdf/2011ICB_humpback.pdf>.
- [8] Summers, Adam. "As The Whale Turns." *Natural History*. Natural History Magazine, n.d. Web. 17 Oct 2013. <<http://www.naturalhistorymag.com/biomechanics/082067/as-the-whale-turns>>.
- [9] LEAP Support Team "Turbulence Part 4 – Reviewing how well you have resolved the Boundary Layer." Leap Australia, 6 May 2013. Web. 14 Dec. 2013. <<http://www.computationalfluidynamics.com.au/tips-tricks-turbulence-part-4-reviewing-how-well-you-have-resolved-the-boundary-layer/>>.
- [10] Carnegie, Claudius. "Wing Design Level 3, Wing Boundary Layer." *ALLSTAR Network*. Florida International University, 02 May 2008. Web. 14 Dec 2013. <<http://www.allstar.fiu.edu/aero/wing34.htm>>.<http://www.cham.co.uk/phoenics/d_polis/d_enc/turmod/enc_tu91.htm>.
- [11] Jureczko, M., Pawlak, M., and Mezyk, A. (2005). Optimization of wind turbine blades. *Journal of Materials Processing Technology*, 167 (2-3), 463-471.

- [12] "Lift(force)." *Wikipedia The Free Encyclopedia*. Wikipedia, 03 DEC 2013. Web. 15 Dec 2013. <[http://en.wikipedia.org/wiki/Lift_\(force\)](http://en.wikipedia.org/wiki/Lift_(force))>.
- [13] Gupta, A., and Amano, R. S. (August, 2012). CFD Analysis of Wind Turbine Blade with Winglets. *Proceedings of the ASME 2012 International Design Engineering Technical Conferences & Computers and Information in Engineering Conference*. Chicago, USA. DETC2012-70679.
- [14] Sourabh Kumar and R. S. Amano (2012). Wind turbine blade design and analysis with tubercle technology. *Proceedings of the ASME 2012 International Design Engineering Technical Conferences & Computers and Information in Engineering Conference*
- [15] J. Calauti, H. Chaudhry, B. Hughes, L. FangSim, *A validated design methodology for a closed-loop subsonic wind tunnel*, pp. 180–194, *Wind Engineering and Industrial Aerodynamics* 125, 2014
- [16] I. Ross , A. Altman, *Wind tunnel blockage corrections: Review and application to Savonius vertical-axis wind turbines*, pp. 523–538, *Wind Engineering and Industrial Aerodynamics* 99, 2011
- [17] C. Bottasso, F. Campagnolo , V. Petrović, *Wind tunnel testing of scaled wind turbine models: Beyond aerodynamics*, pp. 11–28, *Wind Engineering and Industrial Aerodynamics* 127, 2014.
- [18] J. Monteiro, M. Silvestre, H. Piggott, J. André, *Wind tunnel testing of a horizontal axis wind turbine rotor and comparison with simulations from two Blade Element Momentum codes*, pp. 99–106, *J. Wind Engineering and Industrial Aerodynamics* 123, 2013.
- [19] Y. Li, K. Tagawa, F. Feng, Q. Li, Q. He, *A wind tunnel experimental study of icing on wind turbine blade Airfoil*, pp. 591–595, *Energy Conversion and Management* 85, 2014.
- [20] J. Ryi, J. Choi, S. Lee, S. Lee, *A full-scale prediction method for wind turbine rotor noise by using wind tunnel test data*, pp. 257-264, *Renewable Energy* 65, 2014.
- [21] M. Gaunaa, J. Johansen, *Determination of the Maximum Aerodynamic Efficiency of Wind Turbine Rotors with Winglets*, *Journal of Physics: Conference Series* 75, 2007, 012006
- [22] J. Johansen, N. Sørensen, *Aerodynamic investigation of Winglets on Wind Turbine Blades using CFD*, ISSN 0106-2840, ISBN 87-550-3497-7

- [23] A. Elham, M. vanTooren, *Winglet multi-objective shape optimization*, pp. 93–109, *Aerospace Science and Technology* 37, 2014.
- [24] A. Alsultan, A. Block, T. Burg, J. Vriesman, R. Amano, *Design of Experimental Procedure and Analysis methods of Small Scale Wind Turbine Blades with Different Geometries*, Proceedings of ASME 2014 International Design & Engineering Technical Conferences and Computers & Information in Engineering Conference Wind Energy, August 17-20, 2014 Buffalo, New York, USA, DETC2014-35663
- [25] Johansen, J. S. (2006). *Aerodynamic investigation of winglets on wind turbine blades using CFD*. Technical Report Riso-R-1543 (EN), Riso National Laboratory, Denmark.
- [26] Howle, L. E. (2009). WhalePowerWenvor blade. A report in the efficiency of a WhalePower Corp. 5 meter prototype wind turbine blade. BelleQuant Engineering, PLLC.
- [27] Pape, A. L., & Lecanu, J. (2004). 3D Navier-Stokes Computations of a Stall-Regulated Wind Turbine. *Wind Energy*, 7, 309-324.
- [28] Tachos, N. S., Filios, A. E., & Margaris, D. P. (September, 2010). A Comparative Numerical Study of Four Turbulence Models for the Prediction of Horizontal Axis Wind Turbine Flow. *Journal of Mechanical Engineering Science*, 224 (9), 1973-1979.
- [29] Benjanirat, S., Sankar, L. N., & Xu, G. (January, 2003). Evaluation of Turbulence Models for the Prediction of Wind Turbine Aerodynamics. *Proceedings of the 44th AIAA Aerospace Sciences Meeting and Exhibit*, (pp. 73-83). Reno, Nevada (USA)
- [30] Betz, A.: *Windenergie and ihre Ausnutzung durch Windmuhlen*, Vandenhoeck and Rupprecht 1926; Vieweg Gottingen, 1946
- [31] Jason R. Gregg, *Design and Experimental Testing of Small-Scale Wind Turbines*, Dissertation Baylor University
- [32] *Three-phase AC power circuits* (First ed.). (2010). Québec: Lab-Volt.
- [33] Magdi Ragheb and Adam M. Ragheb (2011). *Wind Turbines Theory - The Betz Equation and Optimal Rotor Tip Speed Ratio*, Fundamental and Advanced Topics in Wind Power, Dr. Rupp Carriveau (Ed.), ISBN: 978-953-307-508-2, InTech, Available from: <http://www.intechopen.com/books/fundamental-and-advanced-topics-in-wind-power/wind-turbines-theory-the-betz-equation-and-optimal-rotor-tip-speed-ratio>
- [34] Muyeen, S., & Tamura, J. (2009). *Stability augmentation of a grid-connected wind farm*. London: Springer.

- [35] Schubel, P., & Crossley, R. (n.d.). Wind Turbine Blade Design Review. *Wind Engineering*, 365-388
- [36] Bianchi, F., & Battista, H. (2007). *Wind turbine control systems principles, modelling and gain scheduling design*. London: Springer.
- [37] B. Sanders, Energy research center at the Netherlands. Aerodynamics of wind turbine wakes, literature review (ECN-E—09-16)
- [38] Ferrer, E., & Munduate, X. (2007). Wind turbine blade tip comparison using CFD. *Journal of Physics: Conference Series*, 012005-012005.
- [39] Burton, T. (2011). *Wind energy handbook* (2nd ed.). Chichester, West Sussex: Wiley.
- [40] "Winglets." *Advanced Blended Technology*. The 737 Technical Site, n. d. Web. 17 Oct. 2013. <<http://www.b737.org.uk/winglets.htm>>.

Author's Research Publications on Thesis Topic

- * Design and Analysis of Wind Turbine Blades: Winglet, Tubercle, and Slotted (ASME Turbo Expo 2013, San Antonio, Texas, USA)
- *Numerical and Experimental Performance Analysis of Wind Turbine Blades (49th AIAA/ASME/SAE/ASEE Joint Propulsion Conference (JPC), San Jose', CA, USA)
- *Performance of Wind Turbine Blades with Several Designs (AIAA - 52nd Aerospace Sciences Meeting. USA)
- *Design of experimental procedure and analysis methods of small scale wind turbine blades with different geometries (ASME-IDETC 2014, Buffalo, New york, USA)
- *Novel Wind Turbine Blade designs (ICNGWE, Madrid, Spain)
- *Advances in Horizontal Axis Wind Turbine Blade designs: Introduction of slots and Tubercle. (Journal of Energy resources Technology ASME)(Accepted)

Appendix

A. Experimental findings

In this section we depict the experimental findings for the straight, slotted and tubercle blade.

A.1-Straight blade findings

In this section, we summaries the experimental findings for the straight blade.

Table 26: Summary of experimental power collected from straight blade

Velocity		Straight Power				
		0.2	0.3	0.5	1	2
4.1846	14				0.969624	0.711507
4.4835	15			4.185068	1.258584	0.897627
4.7824	16		4.92075	5.304608	1.569794	1.125469
5.0813	17	5.65068	3.30672	5.65068	1.939154	1.368901
5.3802	18	2.479688	5.874188	8.127608	2.426976	1.6875
5.6791	19	7.575187	7.575187	8.33187	2.969474	2.164951
5.978	20	10.94448	6.169868	10.94448	3.816038	2.716057
6.2769	21	4.68075	7.89507	13.50723	4.800782	3.492723
6.5758	22	5.86092	10.092	16.40581	6.205734	4.291248
6.8747	23	7.26192	11.256	21.52227	7.379286	4.922883
7.1736	24	10.05723	16.98769	25.30927	8.503742	5.614272
7.4725	25	11.64387	19.22401	28.31437	9.571014	6.324912
7.7714	26	18.11187	21.90511	31.91977	10.47025	6.881131

Table 27: Summary of experimental Torque collected from straight blade

Velocity		Straight Torque				
		0.2	0.3	0.5	1	2
4.1846	14				0.016674	0.011261
4.4835	15			0.027147	0.019023	0.012706
4.7824	16		0.053091	0.030533	0.021445	0.014349
5.0813	17	0.084649	0.030956	0.029046	0.023432	0.015605
5.3802	18	0.033161	0.04926	0.037303	0.02661	0.017376
5.6791	19	0.091037	0.057015	0.034963	0.029059	0.019788
5.978	20	0.118702	0.042299	0.041318	0.032875	0.022118
6.2769	21	0.04548	0.047976	0.04441	0.037175	0.024987
6.5758	22	0.05019	0.054499	0.049105	0.041863	0.027631
6.8747	23	0.056193	0.062245	0.056261	0.045698	0.029335
7.1736	24	0.066457	0.071327	0.060821	0.049043	0.031468
7.4725	25	0.071261	0.075579	0.063951	0.052217	0.03346
7.7714	26	0.1028	0.080789	0.067912	0.05423	0.0348

Table 28: Summary of experimental Angular velocity collected from straight blade

		Straight Angular velocity				
Velocity		0.2	0.3	0.5	1	2
4.1846	14				58.15145	63.1857
4.4835	15			61.66543	66.16139	70.64482
4.7824	16		61.79048	69.49364	73.1993	78.43415
5.0813	17	66.75447	71.21257	77.81758	82.75743	87.71934
5.3802	18	74.77677	79.49924	87.15285	91.20569	97.11499
5.6791	19	83.20986	88.5752	95.32099	102.1873	109.4085
5.978	20	92.20169	97.2424	105.9548	116.0781	122.7993
6.2769	21	102.9185	109.7087	121.6589	129.1391	139.78
6.5758	22	116.775	123.4516	133.6381	148.2402	155.3062
6.8747	23	129.2312	137.3545	153.0163	161.4789	167.8157
7.1736	24	151.3338	158.7779	166.4501	173.393	178.4118
7.4725	25	163.3971	169.5711	177.1012	183.2928	189.0277
7.7714	26	176.1861	180.7595	188.0064	193.0724	197.7335

Table 29: Summary of experimental Tip speed ratio collected from straight blade

		Straight Tip speed ratio (TSR= $\omega r/U$)				
Velocity		0.2	0.3	0.5	1	2
4.1846	14				3.891031	4.227882
4.4835	15			3.851081	4.131859	4.411855
4.7824	16		3.61771	4.068714	4.285674	4.592163
5.0813	17	3.678439	3.924098	4.288061	4.560266	4.833687
5.3802	18	3.891583	4.137353	4.535668	4.746588	5.054124
5.6791	19	4.102545	4.367075	4.699667	5.038201	5.394231
5.978	20	4.31858	4.554679	4.962754	5.436913	5.751726
6.2769	21	4.590989	4.893886	5.426963	5.760639	6.235307
6.5758	22	4.972323	5.256614	5.690362	6.312123	6.612995
6.8747	23	5.263464	5.7523	6.232209	6.576882	6.834973
7.1736	24	5.906862	6.19742	6.49688	6.767875	6.963769
7.4725	25	6.122607	6.35395	6.636109	6.868116	7.083004
7.7714	26	6.347907	6.512682	6.773785	6.95631	7.124249

A.2-Slotted Blade findings

In this section, we summaries the experimental findings for the slotted blade.

Table 30: Summary of experimental power collected from slotted blade

Slotted blade experimental Power(Watt)						
Resistance (Ω)		0.2	0.3	0.5	1	2
m/s	Frequency					
4.1846	14		3.478208	4.297868	1.333874	0.947532
4.4835	15	2.07507	3.20787	5.431508	1.694954	1.173751
4.7824	16	2.73612	4.04067	6.88323	2.077994	1.344691
5.0813	17	3.396968	5.006168	8.442908	2.585954	1.689751
5.3802	18	3.888	5.927408	10.37232	3.1104	2.0667
5.6791	19	8.764208	8.764208	12.675	3.664454	2.465227
5.978	20	10.26675	11.83152	15.42267	4.48935	2.931397
6.2769	21	13.44691	13.44691	17.787	5.045334	3.351747
6.5758	22	14.84737	11.88811	20.91675	5.892486	3.868081
6.8747	23	9.27408	13.74987	23.232	6.596114	4.309207
7.1736	24	19.92675	19.92675	26.42347	7.486134	4.873051
7.4725	25	21.80269	21.80269	29.88012	8.539494	5.524347
7.7714	26	24.19212	20.19661	33.93097	9.487838	6.207847

Table 31: Summary of experimental Angular velocity collected from slotted blade

Slotted Angular velocity						
Velocity		0.2	0.3	0.5	1	2
4.1846	14		61.60845	63.96166	68.78988	73.29371
4.4835	15	66.04645	70.40693	72.41782	77.32058	80.99647
4.7824	16	76.32297	79.98434	80.86463	85.69115	87.05571
5.0813	17	84.49158	88.06655	88.83131	95.70091	98.05539
5.3802	18	91.88572	96.15237	99.66345	104.1949	108.7259
5.6791	19	92.00274	106.0964	110.7177	114.0857	118.0461
5.978	20	110.1771	115.2406	121.2031	124.6584	128.9503
6.2769	21	119.5108	125.5566	131.3807	134.5271	138.421
6.5758	22	129.8891	135.5959	140.6019	144.7652	148.5638
6.8747	23	140.1619	144.5959	149.2959	153.2483	157.9412
7.1736	24	149.0182	153.4543	158.3859	163.8506	167.4429
7.4725	25	159.3072	163.55	168.2528	174.4179	178.0613
7.7714	26	169.9565	173.6587	179.0457	184.1908	187.8276

Table 32: Summary of experimental torque collected from slotted blade

Slotted Torque						
Velocity		0.2	0.3	0.5	1	2
4.1846	14		0.037638	0.026878	0.019391	0.012928
4.4835	15	0.031418	0.030375	0.030001	0.021921	0.014491
4.7824	16	0.035849	0.033679	0.034048	0.02425	0.015446
5.0813	17	0.040205	0.037897	0.038018	0.027021	0.017233
5.3802	18	0.042313	0.041097	0.041629	0.029852	0.019008
5.6791	19	0.09526	0.055071	0.045792	0.03212	0.020884
5.978	20	0.093184	0.068445	0.050899	0.036013	0.022733
6.2769	21	0.112516	0.071399	0.054154	0.037504	0.024214
6.5758	22	0.114308	0.058449	0.059506	0.040704	0.026036
6.8747	23	0.066167	0.063394	0.062244	0.043042	0.027284
7.1736	24	0.13372	0.08657	0.066732	0.045689	0.029103
7.4725	25	0.136859	0.088873	0.071036	0.04896	0.031025
7.7714	26	0.142343	0.077534	0.075804	0.051511	0.033051

Table 33: Summary of experimental tip speed ratio collected from slotted blade

Slotted Tip speed ratio (TSR= $\Omega r/U$)						
Velocity		0.2	0.3	0.5	1	2
4.1846	14		4.122345	4.279803	4.602869	4.90423
4.4835	15	4.124681	4.396998	4.522581	4.828764	5.058327
4.7824	16	4.468558	4.682924	4.734463	5.017046	5.096938
5.0813	17	4.655825	4.85282	4.894961	5.273504	5.403245
5.3802	18	4.781979	5.004026	5.186753	5.422583	5.658387
5.6791	19	4.536065	5.230931	5.458779	5.624834	5.820098
5.978	20	5.16052	5.397688	5.676958	5.838801	6.039825
6.2769	21	5.33114	5.600831	5.860629	6.000985	6.174686
6.5758	22	5.530728	5.773725	5.986879	6.164155	6.325901
6.8747	23	5.708661	5.889254	6.080679	6.241658	6.432797
7.1736	24	5.81648	5.989629	6.18212	6.395417	6.535633
7.4725	25	5.969355	6.128338	6.304555	6.535567	6.672087
7.7714	26	6.123455	6.256845	6.450934	6.636311	6.767343

A.3-Tubercle Blade findings

In this section, we summaries the experimental findings for the tubercle blade.

Table 34: Summary of experimental power collected from tubercle blade

Velocity		Tubercle Power				
		0.2	0.3	0.5	1	2
4.1846	14					
4.4835	15					0.699867
4.7824	16			4.230008	1.204224	0.852267
5.0813	17		2.496968	5.030708	1.464216	1.017919
5.3802	18	1.78608	3.062408	6.197108	1.710936	1.185037
5.6791	19	2.15472	3.622688	7.188308	2.028854	1.401517
5.978	20	2.57547	4.320608	8.49072	2.373846	1.614067
6.2769	21	2.97675	5.030708	9.695768	2.701446	1.884169
6.5758	22	3.539768	5.91408	11.07169	3.158102	2.076672
6.8747	23	4.17387	6.82587	12.81187	3.534338	2.304757
7.1736	24	4.788008	7.757168	14.20032	4.009838	2.673408
7.4725	25	5.292	8.570708	16.47243	4.453094	2.991007
7.7714	26	5.96748	9.867068	18.27541	5.045334	3.291769
8.0703	27	6.811568	11.05347	20.46828	5.512334	3.649827
8.3692	28	7.56012	12.288	22.60272	6.163094	4.096177

Table 35: Summary of experimental torque collected from tubercle blade

Velocity		Tubercle Torque				
		0.2	0.3	0.5	1	2
4.1846	14					
4.4835	15					0.011172
4.7824	16			0.027641	0.018495	0.012291
5.0813	17		0.027145	0.030029	0.020477	0.013484
5.3802	18	0.027799	0.030284	0.033422	0.022107	0.014458
5.6791	19	0.030435	0.032676	0.035939	0.023949	0.015803
5.978	20	0.033344	0.035593	0.039167	0.026257	0.016939
6.2769	21	0.035712	0.03858	0.041731	0.027685	0.018435
6.5758	22	0.03938	0.042301	0.044687	0.030241	0.019105
6.8747	23	0.043161	0.045248	0.04804	0.03176	0.01991
7.1736	24	0.046426	0.048314	0.04995	0.033891	0.021755
7.4725	25	0.048403	0.05012	0.054553	0.035502	0.022995
7.7714	26	0.05101	0.05455	0.057063	0.038001	0.02393
8.0703	27	0.054894	0.057645	0.060664	0.039426	0.025236
8.3692	28	0.057574	0.060356	0.063245	0.041814	0.026783

Table 36: Summary of experimental angular velocity collected from tubercle blade

		Tubercle Angular velocity				
Velocity		0.2	0.3	0.5	1	2
4.1846	14					
4.4835	15					62.6451
4.7824	16			61.21394	65.10981	69.33984
5.0813	17		61.32514	67.01053	71.50616	75.48837
5.3802	18	64.25086	67.41454	74.16882	77.39285	81.96524
5.6791	19	70.79839	73.91124	80.00483	84.7159	88.68832
5.978	20	77.23832	80.92679	86.71374	90.40883	95.28566
6.2769	21	83.35479	86.93104	92.9352	97.57907	102.2061
6.5758	22	89.8863	93.20638	99.10351	104.4295	108.6978
6.8747	23	96.7055	100.5693	106.6772	111.284	115.7581
7.1736	24	103.1313	107.0387	113.7165	118.3152	122.8892
7.4725	25	109.331	114.0023	120.7818	125.4308	130.0749
7.7714	26	116.9862	120.5883	128.1077	132.7693	137.5585
8.0703	27	124.0864	127.8339	134.9626	139.8147	144.6264
8.3692	28	131.3103	135.7274	142.9535	147.3923	152.9396

Table 37: Summary of experimental tip speed ratio collected from tubercle blade

		Tubercle Tip speed ratio (TSR= $\Omega r/U$)				
Velocity		0.2	0.3	0.5	1	2
4.1846	14					
4.4835	15					3.912263
4.7824	16			3.583954	3.81205	4.05971
5.0813	17		3.379261	3.692549	3.940276	4.159712
5.3802	18	3.343786	3.508433	3.859944	4.027731	4.26569
5.6791	19	3.490615	3.644089	3.944525	4.176797	4.372652
5.978	20	3.61772	3.790482	4.061533	4.234605	4.463028
6.2769	21	3.718291	3.877821	4.145654	4.352808	4.559212
6.5758	22	3.827392	3.968762	4.219864	4.446648	4.628391
6.8747	23	3.938723	4.096092	4.344861	4.532491	4.714716
7.1736	24	4.02542	4.177935	4.438581	4.618079	4.79661
7.4725	25	4.096711	4.27175	4.525781	4.699982	4.873999
7.7714	26	4.214959	4.34474	4.615664	4.783618	4.956169
8.0703	27	4.305193	4.435213	4.682543	4.850887	5.017829
8.3692	28	4.393118	4.540897	4.782653	4.931157	5.116748

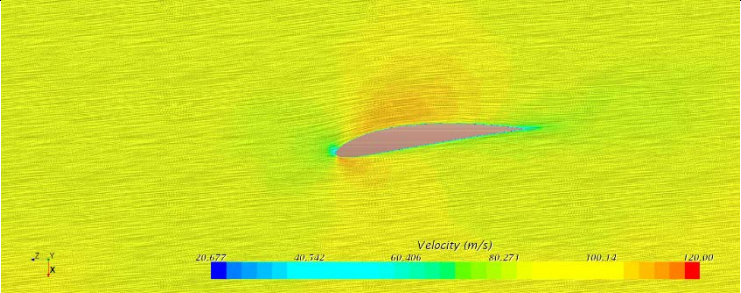
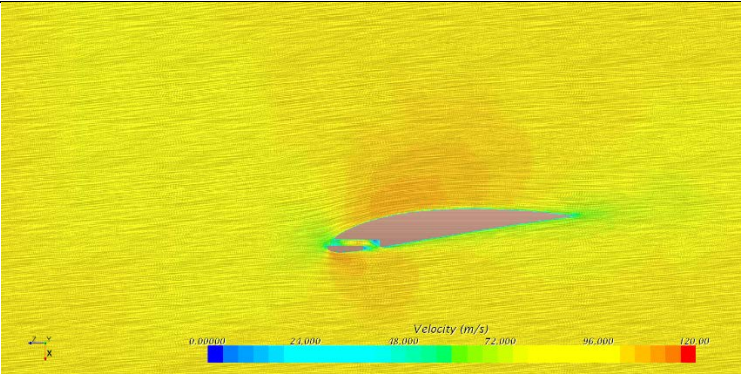
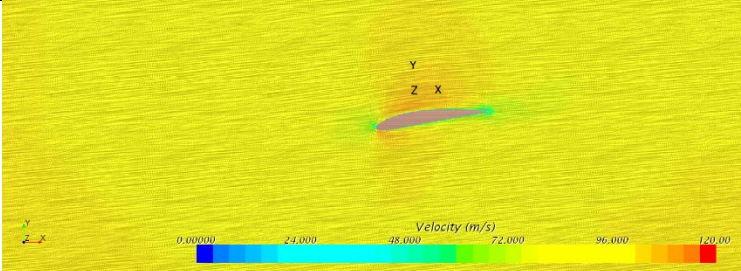
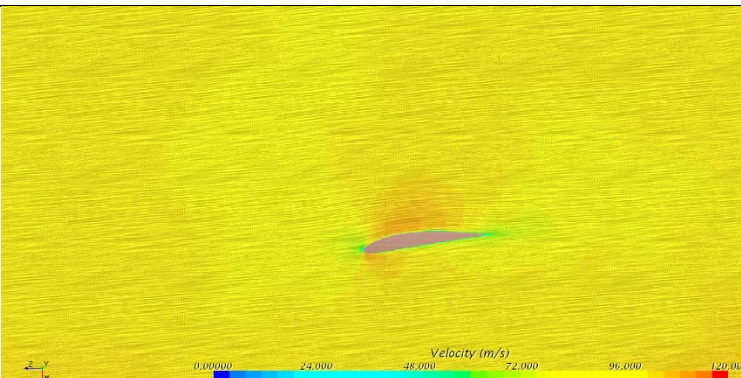
B. CFD Findings (Pressure and Velocity)

In this section, we summaries both velocity vectors and pressure contours for all blade designs.

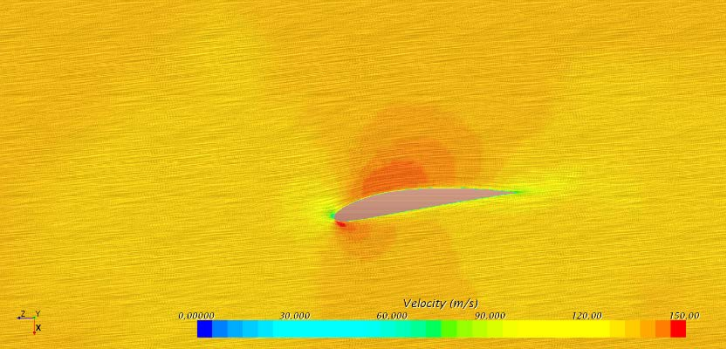
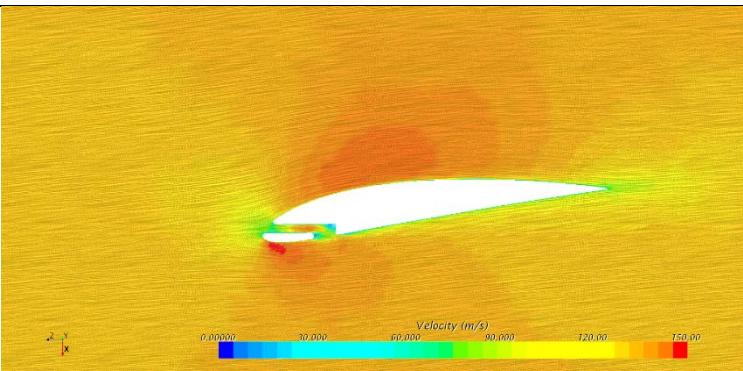
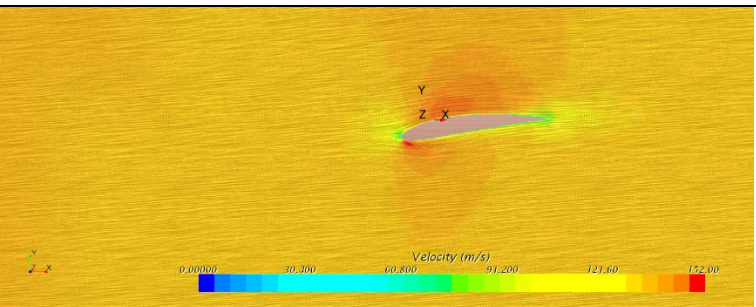
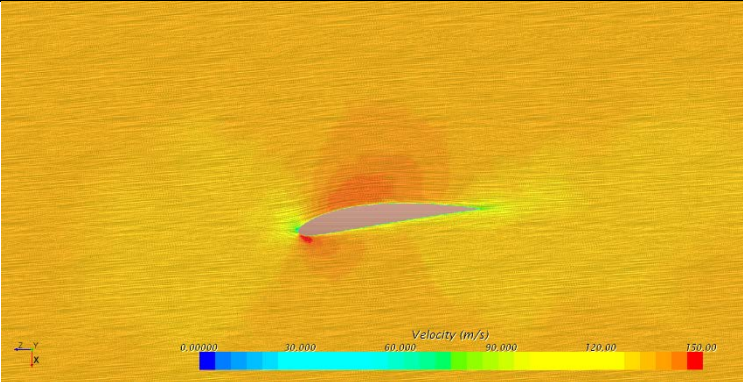
B.1-Velocity Vectors @ 5.3 m/s And 80 Rad/s

Velocity Vectors Taken at 19cm from root @ 5.3 m/s And 80 Rad/s	
Straight Blade	
Slotted Blade	
Tubercle Blade	
Winglet Blade	

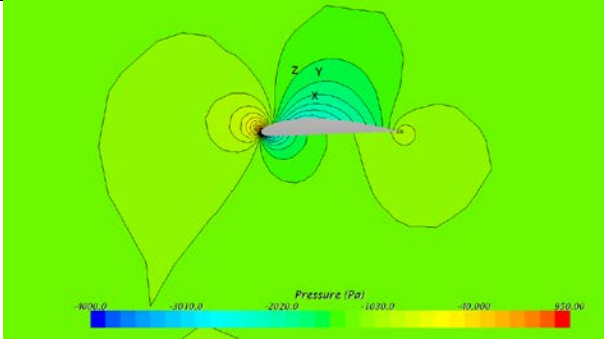
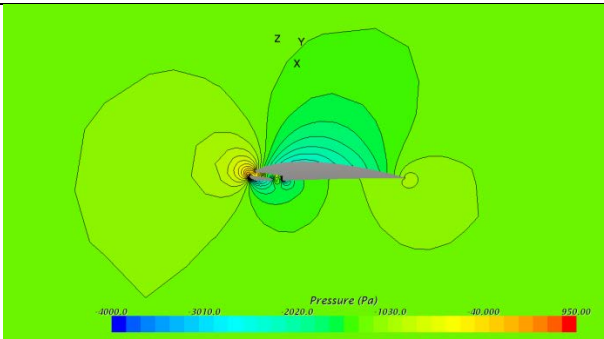
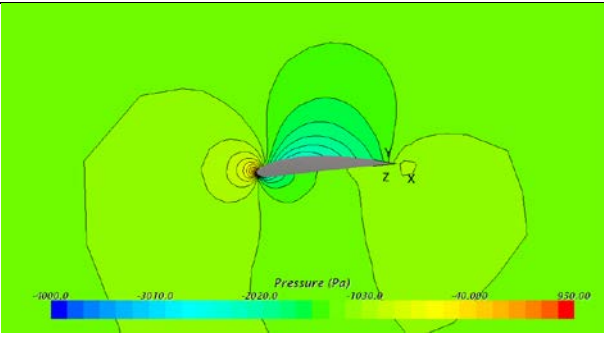
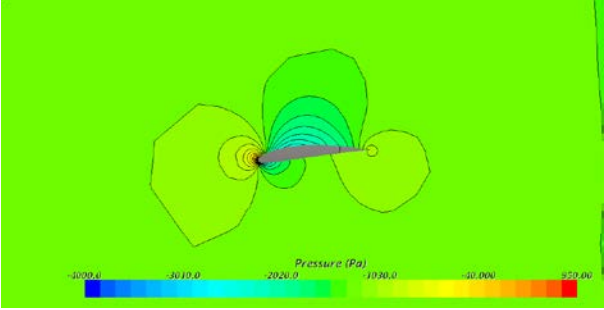
B.2-Velocity Vectors @ 6.2 m/s And 105 Rad/s

Velocity Vectors Taken at 19cm from root @ 6.2 m/s And 105 Rad/s	
<p>Straight Blade</p>	
<p>Slotted Blade</p>	
<p>Tubercle Blade</p>	
<p>Winglet Blade</p>	

B.3-Velocity Vectors @ 7.7 m/s And 150 Rad/s

Velocity Vectors Taken at 19cm from root @ 7.7 m/s And 150 Rad/s	
Straight Blade	
Slotted Blade	
Tubercle Blade	
Winglet Blade	

B.4- Pressure Contours @ 5.3 m/s And 80 Rad/s

Pressure Contours Taken at 19cm from root @ 5.3 m/s And 80 Rad/s	
Straight Blade	
Slotted Blade	
Tubercle Blade	
Winglet Blade	

B.5- Pressure Contours @ 6.2 m/s And 105 Rad/s

Pressure Contours Taken at 19cm from root @ 6.2 m/s And 105 Rad/s	
Straight Blade	
Slotted Blade	
Tubercle Blade	
Winglet Blade	

B.6- Pressure Contours @ 7.7 m/s And 150 Rad/s

Pressure Contours Taken at 19cm from root @ 7.7 m/s And 150 Rad/s	
Straight Blade	
Slotted Blade	
Tubercle Blade	
Winglet Blade	